Università degli Studi di Padova

Sede amministrativa: Università Degli Studi di Padova
Dipartimento di: Ingegneria Industriale
Centro di Ateneo di Studi ed Attività Spaziali CISAS "G. Colombo"

SCUOLA DI DOTTORATO DI RICERCA IN: Scienze Tecnologie e Misure Spaziali
INDIRIZZO: Scienze e Tecnologie per Applicazioni Spaziali ed Aeronautiche
CICLO: XXVII

Optimization and Automatic Control of Radio-Frequency Plasma Thrusters for Space Applications

Ottimizzazione e controllo automatico di propulsori al plasma in radiofrequenza per applicazioni spaziali

Direttore della Scuola: Ch.mo Prof. Giampiero Naletto
Coordinatore d'indirizzo: Ch.mo Prof. Giampiero Naletto
Supervisore: Ch.mo Prof. Daniele Pavarin
Co-supervisore: Dr. Marco Manente

Autore:
Fabio Trezzolani

Abstract

Helicon Plasma Thrusters represent a recent and innovative type of space thrusters, currently receiving the attention of the research community thanks to (i) a very simple structure, based on a dielectric tube(discharge chamber) in which plasma is generated, an RF antenna for propellant ionization and a magneto-static field which confines and conveys the plasma, (ii) the lack of neutralization cathodes and other electrodes immersed in the plasma, resulting in a potentially long lifetime and (iii) the potential capability of operating with different propellants, both mono-atomic and molecular. This PhD thesis reports the development of an innovative experimental set-up for the characterization and optimization of Helicon Plasma Thrusters (HPT) at the electric propulsion facility of CISAS, composed of a test-bed, including a reconfigurable plasma source and an array of plasma diagnostics, and an innovative, high efficiency RF power generation system, intended to test kW-class thrusters. The activity was carried out both autonomously by the electric propulsion group and within the italian research program SAPERE - STRONG (Space Advance Project Excellence in Research and Enterprise - System, Technologies and Research for Global National Operativity)[1], aiming at the development of a kW-class HPT prototype working on Argon or CO_2.

The activity was carried out as a development of the technology and know-how deriving from program HPH.Com, carried out at CISAS from 2008 to 2012 with the objective of developing a 50 W HPT employing Argon [2], during which an innovative, high performance RF plasma source was developed. The new set-up constitutes in fact an upgrade of the existing one, which features (i) an high vacuum pumping system, (ii) a re-configurable low power plasma source and (iii) an array of plasma diagnostic systems, including a microwave interferometer for plasma density measurement, optical spectrometers and Faraday probes for plume current measurements. [3] The general configuration of the high power HPT, over which the design of the set-up was based, was determined by means of a plasma source global model, developed within another PhD work at CISAS. The resulting configuration employs roughly 30-80 times the mass flow rate of HPH and roughly 20-30 times the power. During these simulations the size of the thruster was minimized, resulting in a 7-10 times higher power density with respect to HPH.Com.

The development of an high power set-up suitable for testing such thrusters presented a series of issues:

- the technology of the plasma source, in particular with respect to the RF system, was developed and tested for operation with Argon 50-100 W operation, thus requiring further theoretical and experimental analyses in order to (i) characterize

its performance with new propellants (namely CO_2), (ii) optimize its design, (iii) investigate its power scalability, with particular attention to the increased power density, (iv) develop analysis and design tools for the RF system;

- during the tests the thruster must be re-configured (in terms of geometry and magnetic field) and the input parameters (propellant type and mass flow rate, input power) are varied, resulting in a wide variety of possible operating regimes. The electrical impedance of the antenna will change accordingly, resulting in a widely variable electrical load for the power supply;
- the existing plasma diagnostics, developed for HPH.Com, could not be suitable for operation at the desired power level with the chosen propellants;

These issues were faced by means of a working program articulated in several phases. As a first step a theoretical and experimental survey was carried out on the RF circuit of the thruster, aiming at its frequency-domain and time-domain characterization both with and without plasma. The collected data were employed as a benchmarck from which to develop dedicated numerical codes, namely (i) a Simulink lumped-parameters model,employed for theoretical study and performance analysis of existing antennae, and (ii) an antenna preliminary design tool, based on a coupled Matlab/FEMM (Finite Elements Method Magnetics) capable of performance prediction from antenna geometry and materials. Along with this theoretical-experimental studys a refinement of the electrical design of the thruster was performed by means of an experimental/numerical approach, resulting in the maximization of the electric field generated by the antenna at a given input voltage. This process was followed by a low power HPT optimization with the modified antenna. Operation with CO_2 was explored with the existing low power set-up, in order to identify eventual issues related to the employment of this propellant. The results have shown that CO_2 can be employed in the HPT without significant issues, but requires, for optimal performance, a different plasma source configuration with respect to Argon. In this occasion the employability of the existing plasma diagnostics with CO_2 was analysed and verified. The capability of the vacuum pumping system and the plasma diagnostics of operation with the high power HPT was analyzed, concluding that the existing diagnostics are suited for high power operation. Issues related to the higher power density were explored by means of an intermediate power testing at 500 W with the HPH.Com set-up. This activity allowed to (i) identify thermal and electrical issues and their related solutions, (ii) investigate the power scaling of the HPT plasma source performance, in terms of emission spectra and plasma density The experience and the data collected during this work enabled the design and development of an highly reconfigurable plasma source, characterized by a variable-geometry discharge chamber and a magnetic field which can be varied in position, intensity and shape. Along with the work on the plasma source itself, a dedicated RF power generation system was developed in cooperationwith RESIA, a CISAS partner. The system is composed of (i) an innovative RF amplifier, capable of high efficiency operation with a widely variable load and (ii) an automated control system, capable of avoiding power reflections from the load in any operating condition. An high power HPT prototype was also subject to preliminary design, in order to study solutions useful for the prosecution of program SAPERE - STRONG.

Chapters 1 and 2 provide a general introduction and an overlook on the existing set-up for HPT testing at CISAS; the theoretical and experimental study on the RF system is illustrated in Chapter 3, while Chapter 4 reports the antenna design refinement and low power thruster optimization activity. Chapter 5 treats all the experimental, theoretical and design activites related to the development of an high power test-bed capable of multi-propellant operation, while the design and deveolpment of the RF power generation system is illustrated in Chapter 6. As an accessory activity, the algorithms for Faraday probe data analysis were upgraded, as reported in Chapter 2 and Appendix A.

I propulsori al plasma di tipo Helicon rappresentano una famiglia recente ed innovativa di propulsori spaziali, che sta attualmente ricevendo l'attenzione delle comunità di ricerca grazie ad (i) una struttura molto semplice, basata su un tubo in materiale dielettrico (la camera di scarica) in cui viene generato il plasma, un'antenna RF per propellente ionizzazione e un magnetostatico settore che limita e trasmette il plasma, (ii) la mancanza di catodi di neutralizzazione e di altri elettrodi immersi nel plasma, il che ne estende potenzialmente la vita operativa e (iii) la potenziale capacità di operare con diversi propellenti, sia mono-atomici che molecolari. Questa tesi di dottorato riporta lo sviluppo di un innovativo set-up sperimentale per la caratterizzazione e l'ottimizzazione di Helicon Plasma Thruster (HPT) presso la facility di propulsione elettrica del CISAS, comprendente un test-bed, composto da una sorgente di plasma riconfigurabile e un complesso di apparati di diagnostica di plasma, e un innovativo sistema di generazione di potenza RF ad alta efficienza, destinato a testare propulsori aventi potenze in ingresso dell'ordine del kW. L'attività è stata svolta sia autonomamente dal gruppo di propulsione elettrica e nell'ambito del programma di ricerca italiano SAPERE - STRONG (Space Advance Project Excellence in Research and Enterprise - System, Technologies and Research for Global National Operativity) [1], mirante allo sviluppo di un prototipo di HPT da 1-1.5 kW funzionante con Argon o CO_2.

L'attività costituisce uno sviluppo della tecnologia e del know-how derivante dal programma HPH.Com, portato avanti presso il CISAS dal 2008 al 2012 con l'obiettivo di sviluppare un HPT da 50 W impiegante Argon [2], durante il quale è stata sviluppata una innovativa sorgente dil plasma in RF ad alte prestazioni (Figura[1]). Il nuovo set-up costituisce infatti un aggiornamento di quello esistente, che presenta (i) un sistema di pompaggio ad alto vuoto, (ii) una sorgente di plasma riconfigurabile, progettata per bassa potenza (fino a 100 W) e (iii) una serie di dispositivi diagnostici per il plasma, compreso un interferometro a microonde per la misura della densità del plasma, spettrometri ottici e sonde di Faraday per le misure di corrente nel plume emesso dal motore. [3]

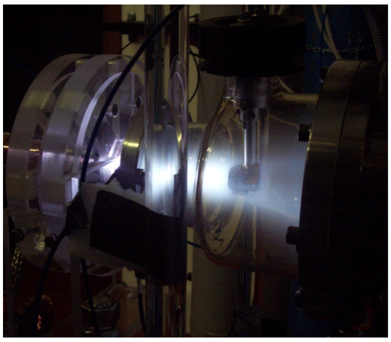

Figure 1: La sorgente di plasma sviluppata al CISAS durante il programma HPH.Com in funzione.

La configurazione generale dello HPT ad alta potenza, sulla base della quale quale è stata basata la progettazione del nuovo set-up, è stata determinata mediante simulazioni condotte con un modello globale della sorgente di plasma, sviluppato nell'ambito di un altro lavoro di dottorato presso il CISAS. La configurazione risultante impiega circa 30-80 volte la portata massica di HPH e circa 20-30 volte la potenza. Nelle simulazioni è stata imposta la minimizzazione delle dimensioni del thruster, in modo da competere più efficientemente con altre tecnologie propulsive caratterizzate da prestazioni similari (propulsori ad effetto Hall, propulsori a ioni), con il risultato di arrivare ad una densità di potenza per unità di superficie maggiore di 7-10 volte rispetto ad HPH.Com.

Lo sviluppo del set-up ad alta potenza destinato a testare simili propulsori ha dovuto fronteggiare una serie di problematiche, che possono essere così riassunte:

- *la tecnologia alla base della sorgente di plasma, in particoalr modo per quanto riguarda il circuito in RF, è stata sviluppata e testata per impiego con Argon a livelli di potenza compresi fra 50-100 W. Ciò porta alla necessità di una ulteriore analisi teorica e sperimentale per (i) caratterizzarne le prestazioni con nuovi propellenti (CO_2 nello specifico), (ii) ottimizarne il design, (iii) indagarne la scalabilità, in particolare tenendo conto della maggiore densità di potenza, (iv) sviluppare strumenti di analisi e design del circuito in RF;*
- *durante le prove il propulsore deve essere ri-configurato (in termini di geometria e campo magnetico) ed i parametri di input (tipo di propellente, portata di massa, potenza di ingresso) vengono variatii, portando ad una grande varietà di possibili regimi di funzionamento. L'impedenza elettrica dell'antenna cambierà di conseguenza, venendo vista come un carico elettrico ampiamente variabile dal sistema di generazione di potenza elettrica;*
- *gli apparati diagnostici per il plasma esistenti sono stati sviluppati durante HPH.Com per essere usati su plasmi di Argon a bassa potenza. Ciò implica che i loro range di funzionamento potevano non essere adatti per il funzionamento ad alta potenza e/o per l'impiego con altri propellenti ;*
- *l'accresciuta densità di potenza rispetto ad HPH comporta maggiori carichi termici e più alte tensioni e correnti, con rischi di danneggiamento potenzialmente accresciuti.*

Questi problemi sono stati affrontati tramite un programma di lavoro articolato in varie fasi. Come primo passo è stata condotta un'indagine teorica e sperimentale a bassa potenza sul circuito RF del propulsore, volta a caratterizzarne l'impedenza complessa nel dominio della frequenza e nel dominio del tempo, con e senza il plasma. Sulla base *dei dati raccolti è stato possible sviluppare (i) un affidabile modello a parametri concentrati, implementato in Matlab e Simulink, impiegato per studi teorici e per l'analisi prestazionale delle antenne esistenti e (ii) uno strumento numerico di progettazione preliminare per le antenne, sulla base di un algoritmo accoppiato Matlab / FEMM (Finite Elements Method Magnetics) capace di prevedere le prestazioni elettriche di un'antenna sulla base della sua struttura e dei materiali. Assieme a questo studio teorico/sperimentale è stato portato avanti anche un processo di raffinazione del design del circuito RF del propulsore, condotto anche in questo caso per mezzo di test sperimentali e analisi numeriche, miranti alla massimizzazione del campo elettrico generato dall'antenna per un dato voltaggio applicato ai suoi morsetti di ingresso. Questo processo è stato seguito da una ottimizzazione bassa potenza dell'HPT con l'antenna modificata, allo scopo di caratterizzarne le prestazioni in configurazione aggiornata.*

L'incognita circa i funzionamento con CO_2 *è stata affrontata mediante test a bassa potenza con tale gas (Figura[2]), condotti impiegando il set-up di HPH.Com, al fine di individuare eventuali problematiche legate all'impiego di questo propellente. I risultati hanno dimostrato che la* CO_2 *può essere impiegata come propellente senza problemi significativi, ma richiede, per ottenere prestazioni ottimali, una configurazione sorgente di plasma differente rispetto all' Argon. In questa occasione l'impiegabilità delle diagnostiche di plasma esistenti con* CO_2 *è stato analizzata e verificata. La capacità del delle diagnostiche di operare ai regimi di potenza e portata massica richiesti dal nuovo propulsore è stata analizzata, concludendo che gli apparati attualmente disponibili sono adatti per il funzionamento ad alta potenza. Gli effetti della superiore densità di potenza sono stati esplorati tramite test alla potenza intermedia di 500 W con il set-up di HPH.Com, sottoponendolo dunque ad una densità di potenza 10 volte superiore a quella già testata. Questa attività ha permesso di (i) individuare i problemi termici/elettrici legati alla maggiore densità di potenza ed elaborare relative soluzioni, (ii) studiare il modo in cui le prestazioni della sorgente di plasma sviluppata per gli HPT scalano con la potenza, in termini di spettri di emissione e densità del plasma, (iv) verificare che non insorgano fenomeni di instabilità di plasma. L'esperienza ed i dati raccolti durante questo lavoro hanno reso possiblie la progettazione e lo sviluppo di una sorgente di plasma riconfigurabile, caratterizzata da una camera di scarica a geometria variabile e di un campo magnetico che può essere variato in posizione, intensità e forma. Parallelamente allo sviluppo della sorgente di plasma è stato inoltre portato avanti lo sviluppo di un sistema di generazione di potenza in RF. Tale attività è stata condotta in cooperazione con RESIA, un partner del CISAS durante HPH.Com, specializzato in realizzazioni elettroniche non convenzionali. Il sistema è composto da (i) un innovativo amplificatore RF, in grado di funzionare ad alta efficienza con un carico ampiamente variabile e (ii) un sistema di controllo automatizzato, in grado di evitare le riflessioni di potenza dal carico in ogni condizione operativa. In aggiunta a questa attività si è inoltre proceduto alla* *progettazione preliminare di un HPT ad alta potenza impiegante anidride carbonica come propellente, allo scopo di identificare soluzioni progettuali utili per la futura prosecuzione del programma SAPERE - STRONG.*

I capitoli 1 e 2 forniscono un'introduzione generale ed un preliminare sguardo d'insieme sul set-up per il testing e lo sviluppo di propulsori Helicon al CISAS; lo studio teorico e sperimentale sul sistema RF è illustrato nel capitolo 3, mentre il capitolo 4 riporta il processo di raffinazione del design dell'antenna e la successiva ottimizzazione a bassa potenza del propulsore. Il capitolo 5 tratta tutte le attività sperimentali, teoriche e progettuali legate allo sviluppo di un banco di prova ad alta potenza in grado di funzionare con diversi propellenti, mentre il design e deveolpment del sistema di generazione di potenza RF è illustrato nel capitolo 6.
Come attività accessoria sono stati aggiornati gli algoritmi per l'analisi dei dati della sonda di Faraday, come riportato nel capitolo 2 e nell'appendice A.

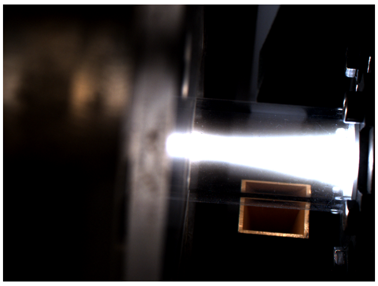

FIGURE 2: Test a bassa potenza con CO_2. Sotto la scarica di plasma è parzialmente visibile una delle guide d'onda dell'interferometro a microonde.

Acknowledgements

I have many persons to thank for this work:

my family, in particular my wife Donata, whose inexhaustible patience and encouragement helped me to complete my work;

my supervisor, prof. Daniele Pavarin, for the opportunity of working in the stimulating field of space thrusters, for his volcanic creativity and for his confident attitude towards new challenges, which tought me that ”*if you can imagine it, you can achieve it*”;

my co-supervisor dr. Marco Manente, from whose patient help, competence and rational rigor I learned the importance of precision, organization and generosity at work;

dr. Antonio Selmo, in fact my mentor, for his vast expertise, bright ingenuity and generosity, which taught me that paperwork and real engineering are not the same thing, that mastering a lathe is as important as mastering a computer and most important of all that creativity and fantasy are by far an engineer's most valuable tools;

my fellow colleagues of the Advanced Space Propulsion Group at CISAS, for the positive working environment which I had and have the luck of operating in.

Contents

List of Figures

List of Tables

Abbreviations

PPU	**P**ower **P**rocessing **U**nit
HPT	**H**elicon **P**lasma **T**hruster
RF	**R**adio **F**requency
RPA	**R**etarding **P**otential **A**nalyzer
FWHM	**F**ull **W**idth **H**alf **M**aximum
EDF	**E**nergy **D**istribution **F**unction

Physical Constants

Speed of Light $c = 2.997\ 924\ 58 \times 10^{8}\ \mathrm{ms}^{-1}$ (exact)

Elementary charge $e = 1.602\ 176\ 57 \times 10^{-19}\ \mathrm{C}$

Proton mass $m_p = 1.672\ 621\ 777 \times 10^{-27}\ \mathrm{kg}$

Electron mass $m_e = 9.109\ 382\ 916\ 217 \times 10^{-31}\ \mathrm{kg}$

Standard Earth gravity acceleration $g_0 = 9.806\ 65\ \mathrm{ms}^{-2}$

Symbols

V	voltage	V
I	current	A
Z	impedance	Ω
P	power	W (Js^{-1})
$\dot{m}$	mass flow rate	kgs^{-1}
I_{sp}	specific impulse	s
f	frequency	Hz
ω	angular frequency	rads^{-1}

Dedicated to my wife, Donata, and my Son, Giacomo.

Chapter 1

Introduction

1.1 Electric propulsion overview

In the vast field of space propulsion electrical thrusters are one of the most important and promising technologies, due to their unique performance features. As all other existing types of thrusters these devices necessarily work according to Newton's third law, thus requiring a propellant of some sort to be accelerated towards the back of the thruster in order to generate a net thrust in the other direction; the difference between electric thrusters and traditional chemical thrusters, however, lies in the acceleration mechanisms of the propellant: indeed all electric thrusters rely on purely electric phenomena, where no thermo-dynamical processes are involved, thus being virtually free from the efficiency limitations proper of thermodinamic systems. In almost all cases the propellant is a gas which is electrically ionized by means of DC or AC antennas and/or electrodes and then accelerated by means of electric and magnetic fields. These features allow these thrusters to achieve unique performance levels, which can be better explained with the preliminary introduction of some parameters quantifying the propulsive performance of a thruster:

$$I_{sp} = c_{exh}/g_0 \quad [s] \tag{1.1}$$

$$T = I_{sp} \cdot \dot{m} \cdot g_0 \quad [N] \tag{1.2}$$

$$\tag{1.3}$$

The first parameter, I_{sp}, is called *specific impulse* and gives a measure of the exhaust velocity c_{exh} of the ejected propellant as a function of the time it would require to the standard earth gravity acceleration g_0 to accelerate the propellant to c_{exh}; the second parameter is thrust and can be expressed as a function of Isp, the propellant mass flow rate $\dot{m}$: as it can be seen, for a given mass flow rate, the higher the specific impulse, the higher the thrust. Specific impulse also influences the size of the amount of propellant required by a spacecraft in order to perform an orbital maneuver, as can be appreciated from the well known Tsiolkovsky's equation:

$$\Delta v = v_{exh} \ln \frac{m_0}{m_1} = I_{sp} \cdot g_0 \cdot \ln \frac{m_0}{m_1} \tag{1.4}$$

where m_0 and m_1 are the initial and final mass of the spacecraft respectively, while Δv is the magnitude velocity change required by the maneuver. Clearly the mass of propellant consumed by the spacecraft will be $m_p = m_0 - m_1$, thus, for a given maneuver implying a given Δv, an high I_{sp} means a lower m_0/m_1 ratio and thus a lower propellant consumption. Thanks to their peculiar acceleration mechanisms the electric thrusters can impress a very high exhaust speed to their propellants, reaching extremely high I_{sp} values, as shown in Figure[1.1]: the I_{sp} of thermodynamics-based rockets typically ranges from in the 300-500 s of chemical thrusters up to 800-1000 s of more exotic systems, such as nuclear rockets; existing electric thrusters, instead, can easily achieve I_{sp}s ranging from 1000 to more than 3000 s [4], with innovative systems, such as the FEEP thruster [5], reaching up to 10000-19000 s . Such specific impulse values allow electric thrusters to produce very large Δvs with a given amount of fuel, or on the other hand to greatly reduce fuel consumption for a given maneuver with respect to chemical rockets.

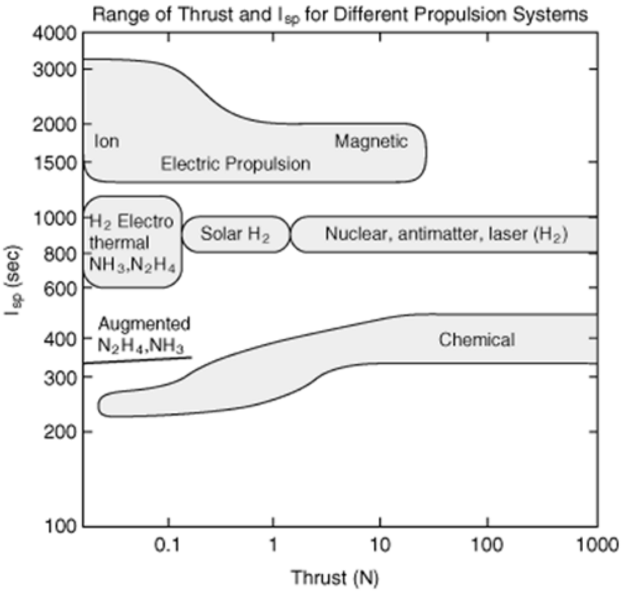

FIGURE 1.1: Typical I_{sp} ranges of space thrusters. Electric thrusters are by far superior to other technologies under this point of view.

Such high I_{sp}s, however, present a serious drawback: if we quantify the power of the propellant ject ejected by the thruster we find:

$$P_j = \frac{1}{2} \cdot \dot{m} \left(I_{sp} \dot{g}_0 \right)^2 = \frac{1}{2} \cdot \frac{T^2}{\dot{m}} \quad [W] \tag{1.5}$$

Recalling eq. 1.2 we can see that, for a given thrust level, an increase in the specific impulse produces a linearly proportional decrease in the required mass flow rate, but, at the same time, implies an *increase* in the jet power, which is proportional to I_{sp}^2. This means that increasing the specific impulse will on one hand reduce the required amount of propellant but, on the other hand, will require more power to generate the same thrust level. Given the current technological level in the field of power generation systems for space vehichles, no more than a few kWs can be available to the thruster at most, unless more performing power sources are developed, meaning that the thrust range practivally accessible at present by electric propulsion systems lies below some tenths of N. Experimental systems, such as the VASIMR [6] or the DS4G thruster [7], should be able to produce 2.5-5 N of thrust, but at the cost of a 200-250 kW input power.

High specific impulse and low thrust are thus the hallmark features of electric thrusters, precluding them the application on earth-to-orbit launch systems but making them the ideal candidates for a wide array of other apcplications, such as long term attitude control, atmospheric drag compensation in low orbit, orbital servicing and interplanetary exploration.

1.2 Helicon Plasma Thrusters

Within the large family of electric thrusters several technologies have been developed or are currently being studied; the first and currently most mature ones are surely ion thrusters, mainly studied in the United States, and Hall effect thrusters, which knew their highest development in the former Soviet Union. Both technologies, whose origin dates back to early 1960, are electrostatic thrusters, in which a gas (typically Xenon) is ionized and then subject to a DC electric field by means of a physical polarized grid (ion thrusters) or a virtual grid composed of magnetically trapped electrons (Hall effect thruster). In both cases the ions within the plasma are accelerated at great speed outside the thruster, thus achieving very high specific impulses, but the ion beam must be neutralized by means of dedicated cathodes immediately after the acceleration, in order to avoid a negative charge build-up inside the thruster which would ultimately block its operation. These thrusters are at the top among electric thrusters under the point of view of specific impulse and thrust, but the presence of grids and/or electrodes at contat with the plasma severely limits their operating lifetime. Along with these two types of thruster, which know a constant refinement, other, more innovative technologies are currently being studied and developed worldwide; among these the Helicon Plasma Thruster has emerged in the last few years as a very promising solution, offering the performance of an electric thruster with the additional advantages of higher flexibility, lower complexity, extended lifetime and reduced costs if compared to other technologies. In this thruster plasma is ionized and heated by means of an RF antenna, which, thanks to the presence of a proper DC magnetic field, allows the establishment of helicon waves [8] efficiently transferring energy to the plasma. HPTs are characterized by the following features:

- the structure is very simple (Figure[1.2]), being just composed by i) a dielectric chamber, in which the propellant is ionized, ii) an RF antenna, wrapped around the chamber and responsible for gas ionization, iii) a magneto-static field, devoted to plasma confinement and expansion (magnetic nozzle), iv) a propellant injection system;
- there are no electrodes immersed in the plasma;
- no neutralizer cathodes are required, since the ejected plasma is quasi-neutral due to ambipolar diffusion [8];
- the configuration of the thruster can easily be optimized for operation with different propellants.

The absence of immersed electrodes and of neutralizer cathodes greatly reduces erosion issues with respect to more traditional electrostatic devices, thus leading to a potentially longer operating lifetime, while the simple and flexible configuration means lower costs and increased reliability.

1.3 Frame of the work: Helicon thrusters at CISAS

HPTs are currently a subject of research in the United States, the EU and Japan [9–12]; in the EU, in particular, work on HPTs was started with the FP7 program HPH.COM (ref. 218862) [2], conducted by a consortium of 15 between research institutes and private companies belonging to several EU and eastern europe states and led by CISAS

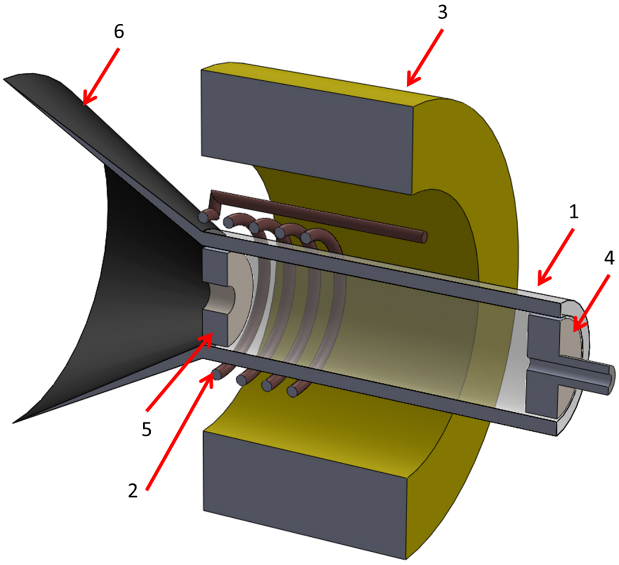

Figure 1.2: Structure of an HPT. 1: discharge chamber. 2: RF antenna. 3: magnetic system. 4: Injector. 5: outlet section. 6: baffle.

(Figure[1.3]). The program, which ended successfully in may 2012, aimed at the development of a low power HPT in the 50 W - 1 mN range for mini and micro-satellite applications. During the program CISAS developed: (i) dedicated numerical tools for plasma and antenna simulations, (ii) an innovative experimental set-up for HPT characterization and (iii) a novel, high efficiency RF plasma source for the HPT. The final result of the project was an HPT Qualification Model (Figure[1.4]), manufactured ad the Kharkov Aviation Institute (KhAI) of Kharkov, Ukraine, and jointly tested by KhAI and CISAS both in Ukraine and Italy [13].

Since the end of HPH.COM the work on HPT at CISAS is ongoing both autonomously and in the frame of EU and italian research projects, the most important currently being SAPERE - STRONG (Space Advance Project Excellence in Research and Enterprise - System, Technologies and Research for Global National Operativity)[1], which aims at the development of (i)space exploration and access and (ii) technologies for electric propulsion modules, with a particular focus on applications involving orbital servicing and space tug vehicles, requiring power levels on the order of some kW.

Within this frame the activity at CISAS focuses on (i) deepening the theoretical knowledge on the physics of HPT plasma sources, (ii) exploring the employment of various propellant gases, (iii) scaling up the power level, in order to meet the thrust requirements of the wide array of applications envisioned by the ongoing projects. These objectives are pursued through the following activities:

- development of dedicated simulation tools for the analysis and design process of the HPT;
- low power optimization of the existing low-power HPT laboratory model;
- development of the existing experimental set-up in order to allow high power operation (up to 1 - 1.5 kW) with different propellant gases;
- analysis and eventual improvement of the existing diagnostic systems in order to ensure their applicability to the operating regimes of interest;
- design and development of a dedicated RF Power Processing Unit, capable of operation in the required power regime and coupled to a control system capable of ensuring an optimal power transfer to the antenna in every condition.

FIGURE 1.3: HPH.COM logo with the list of involved partners.

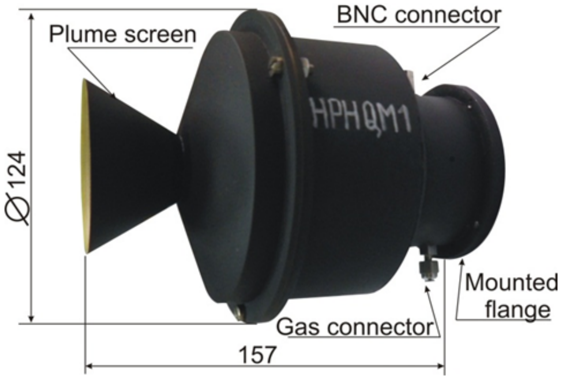

FIGURE 1.4: HPH.COM Qualification Model, manufactured at KhAI.

1.4 PhD activity

The author has actively taken part to all the activities illustrated in this work, with innovative contributions in several areas.

He dedicated a great part of his PhD work to carry out the extensive numerical and experimental study on the RF network of the thruster reported in Chapter 3, whose high efficiency constitute the key element of the HPT developed at CISAS. With respect to this subject, the author:

- took part in the manufacturing of several RF antennae, in cooperation with RESIA;
- experimentally characterized several antennae and other elements of the RF circuit, both alone and in cooperation with RESIA (3.1);
- autonomously developed a lumped-parameters model of the RF network, useful for both theoretical studies and performance analysis (3.1, 3.2);
- autonomously developed an antenna preliminary design tool, based on a finite elements model of the antenna coupled with a Matlab algorithm (3.3).

The author provided another original contribution by refining the basic design of the RF network, upgrading it in order to maximize the electrical field produced by the antenna for a given input voltage, by means of the numerical - experimental approach described in 4.4. The same chapter also reports the activity of optimization of the low power HPT in-vacuum model with the upgraded antenna, carried out by the author as a completion of the antenna upgrade process (4.5).
These contributions paved the way for the power scaling of the RF network, belonging to the more general group of activities related to the development of an high power multi-propellant set-up, which are reported in Chapter 5. The author contributed to this effort by:

- autonomously carrying out the characterization tests on the HPH.Com set-up at progressively higher power, with the target of reaching 500 W, which is representative of the power density required by the high power application (see 5). This activity allowed the author to identify the main issues related to the operation of the RF system in such conditions and to develop solutions to be implemented in order to overcome them, in cooperation with RESIA (5.4.1);
- autonomously performing tests with the upgraded RF network at the power of $\approx$ 500 W (5.4.3).

In the frame of the activities illustrated in Chapter 5 the author also:

- autonomously carried out low power characterization tests on the HPH.Com set-up at low power with CO_2 propellant, which potentially constitutes an innovative, low cost alternative to noble gases. This provided a first insight on the performance of the HPT with such gas (5.3);

- autonomously carried out a survey of the existing plasma diagnostics and experimental facility, in order to verify their employability for high power multi-propellant tests (5.5);
- identified the thermal and electrical issues related to high power density and developed solutions to overcome them (5.4.2);
- autonomously designed an high power plasma source, based on the input provided by numerical simulations performed by another CISAS PhD student in the frame of his work (5.6).

The author has also performed the preliminary design of an high power HPT working on CO_2 propellant, identifying design solutions to be employed in the future prototype development phase, required by the ongoing research projects.

Along with the activities on antennae and plasma source the author took also part in the development of the high efficiency RF power generation system illustrated in Chapter 6, in particular:

- he took part, in cooperation with RESIA, to the conceptual design of the new RF amplifier (6.1.2);
- he took part, in cooperation with RESIA, to the manufacturing and testing of a prototype amplifier calibrated for the intermediate power of 480 W and representative of the kW-class final device (6.1.3);
- he took part, in cooperation with RESIA, to the conceptual design of the control electronics (6.2.1);
- he autonomously developed a Simulink model for time-domain simulation of the control electronics operation (6.2.2).

As a side activity the author also developed new algorithms for the data analysis of Faraday probes, as illustrated in A and 2.3.3

L'autore ha attivamente preso parte a tutte le attività illustrate in questa tesi, con contributi innovativi in diversi settori.
Gran parte del suo lavoro di dottorato è stato destinato all' ampio studio numerico e sperimentale sul network in RF del propulsore, riportato nel capitolo 3, la cui alta efficienza costituisce l'elemento chiave dell'HPT sviluppato dal CISAS. Per quanto riguarda questo argomento, l'autore:

- *ha partecipato alla realizzazione di diverse antenne in RF, in collaborazione con RESIA;*
- *ha caratterizzato sperimentalmente diverse antenne ed altri componenti del nework in radio-frequenza, sia autonomamente che in collaborazione con RESIA (3.1);*
- *ha autonomamente sviluppato un modello Simulink a parametri concentrati del network in RF, utile per entrambi gli studi teorici e analisi delle prestazioni (3.1, 3.2);*
- *ha autonomamente sviluppato uno strumento di progettazione preliminare dell'antenna, basato su un modello agli elementi elementi finiti dell'antenna accoppiato con un algoritmo Matlab (3.3).*

L'autore ha fornito un altro contributo originale raffinandone il design di base del network in RF, modificandolo in modo da massimizzare il campo elettrico prodotto dalla antenna per una data tensione di alimentazione, mediante l'analisi numerica- sperimentale descritta in 4.4. Lo stesso capitolo riporta anche l'attività di ottimizzazione a bassa potenza del modello da vuoto dell'HPT impiegante l'antenna aggiornata, effettuata dall'autore come completamento del processo di aggiornamento della parte circuitale (4.5).
Questi contributi hanno aperto la strada per lo scaling in potenza del sistema RF, appartenente all'insieme più generale delle attività legate allo sviluppo di un set-up multipropellente ad alta potenza, riportate nel capitolo 5. L'autore, in merito a questo punto, ha:

- *portato autonomamente avanti l'esecuzione delle prove di caratterizzazione sul set-up di HPH.Com a potenza progressivamente più elevata, con l'obiettivo di raggiungere il valore di 500 W, in corrispondenza del quale si ha la stessa densità di potenza richiesta dall'applicazione alta potenza (vedi 5) . Questa attività ha permesso all'autore di individuare le principali problematiche relative al funzionamento in tali condizioni e di studiare, congiuntamente con RESIA, soluzioni da attuare al fine di superarle.; (5.4.1);*
- *eseguito autonomamente i test con il network in RF aggiornato fino ad una potenza di $\approx$ 500 W (5.4.3).*

Nel quadro delle attività illustrate nel capitolo 5 l'autore ha anche:

- *autonomamente effettuato prove di caratterizzazione a bassa potenza sul set-up di HPH.Com a bassa potenza, impiegando come propellente CO_2, che costituisce potenzialmente un innovativa alternativa a basso costo ai gas nobili attualmente usati in propulsione elettrica. Questo ha fornito una prima panoramica sulle prestazioni del HPT con tale gas (5.3);*
- *autonomamente effettuato un'analisi delle diagnostiche di plasma già disponibili e dell'impianto ad alto vuoto destinato ad ospitare i test, al fine di verificare la loro impiegabilità per le prove ad alta potenza con diversi propellenti (5.5);*
- *individuato le problematiche termiche ed elettriche relative alla elevata densità di potenza, studiando relative soluzioni (5.4.2);*
- *autonomamente progettato una sorgente di plasma ad alta potenza, in base all'input fornito da simulazioni numeriche effettuate da un altro dottorando CISAS nell'ambito del suo lavoro (5.6).*

L'autore ha inoltre eseguito la progettazione preliminare di un HPT ad alta potenza impiegante CO_2, individuando soluzioni progettuali utili per la futura fase di realizzazione di tale dispositivo, prevista dai programmi di ricerca in corso.

L'autore ha anche partecipato allo sviluppo del sistema di generazione di potenza RF ad alta efficienza illustrato nel capitolo 6, in particolare:

- *ha partecipato, in collaborazione con RESIA, alla progettazione concettuale del nuovo amplificatore RF (6.1.2);*
- *ha partecipato, in collaborazione con RESIA, alla produzione e la sperimentazione di un prototipo di amplificatore calibrato alla potenza intermedia di 480 W e rappresentativo del dispositivo da 1-1.5 kW (6.1.3);*
- *ha partecipato, in collaborazione con RESIA, alla progettazione concettuale dell'elettronica di controllo (6.2.1);*
- *ha autonomamente sviluppato un modello Simulink per la simulazione nel dominio del tempo del funzionamento dell'elettronica di controllo (6.2.2).*

Come attività accessoria, l'autore ha inoltre sviluppato nuovi algoritmi per l'analisi dati delle sonde di Faraday impiegate al CISAS, come illustrato in A e 2.3.3.

Chapter 2

The Electric Propulsion Experiment at CISAS

The this work was performed ont he basis of the Helicon Plasma Thruster experiment started at CISAS during project HPH.COM [3, 14], whose key features are outlined in this chapter. Some preliminary work aimed at the improvement of the data analysis process for Faraday probes was performed in the early stages of the activity; these interventions are not strictly related to the PhD thesis subject, but will be illustrated in order to give a comprehensive look at how these diagnostics are employed.

2.1 The experimental facility

2.1.1 High Vacuum System

The high vacuum facility available at CISAS propulsion laboratory allows to reproduce an environment which represents the operating conditions of the thrusters. The facility is based on a cylindrical vacuum chamber, 2 m long and with an inner diameter of 0.6 m, featuring several flanges equipped with electrical, gas and optical feed-throughs, along with a DN160 gate valve through which other vacuum systems can be connected to the chamber itself. The vacuum is provided by a pumping system composed of a turbomolecular pump and a diffusion pump, whose combined pumping capacity reaches the nominal value of 12600 l/s. The two main pumps are connected in series to a pair of backing pumps (a roots and a rotary one), which produce the pressure level required at the exhaust of the main pumps. The pressure level inside the chamber typically ranges between $8 \cdot 10^{-6}$ mbar (clean chamber, without mass flow rate) to $1 \cdot 10^{-4}$ mbar (during thruster operation at the maximum mass flow rate). A quadrupole mass spectrometer is available to monitor the presence of contaminants within the chamber, but cannot be employed during tests since its maximum operating pressure is 10^{-5} mbar. The pressure levels in the chamber and in other critical points of the vacuum system are monitored by means several Edwards APG100-XLC Pirani gauges, which can measure pressures ranging from 1 bar to 10^{-4} mbar (accuracy ±15% below 10 mbar), while an Edwards AIM-S-NW25 active inverted magnetron gauge is employed in the chamber alone during high vacuum operation (from 10^{-4} mbar to 10^{-9} mbar, accuracy ±30%). An overall scheme of the vacuum system is shown in Figure[2.1].

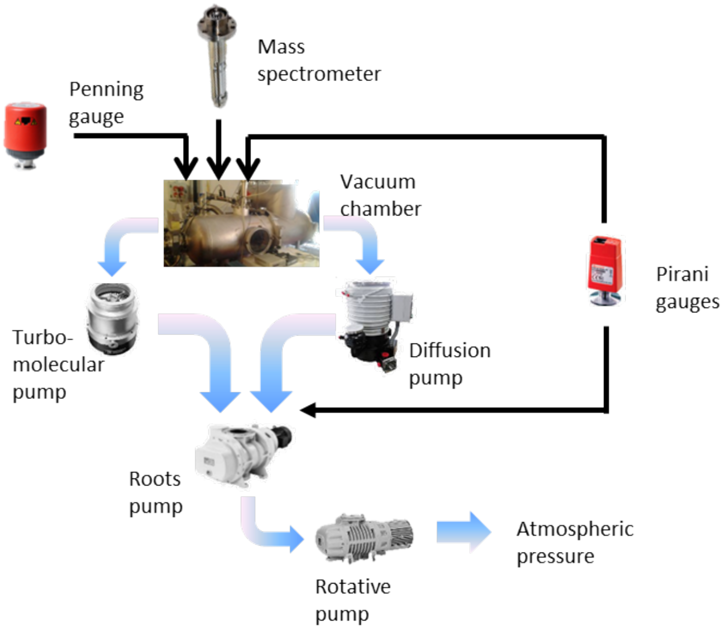

FIGURE 2.1: Overall scheme of the vacuum system.

2.1.2 RF system

The RF system is devoted to the generation of RF power by means of an amplifier, and of the subsequent transfer of this power to the antenna. The most critical aspect of this system is represented by the so defined *impedance matching*: the power is generated by an amplifier, which can be modeled making use of the real voltage generator scheme, illustrated in Figure[2.2]. Here $Z_A = R_A + jX_A$ is the amplifier's input impedance, while $Z_L = R_L + jX_L$ is the impedance of the load; in these conditions, for systems operating in RF, two important impedance matching conditions can be identified [15]:

- reflection-less matching, $Z_A = Z_L$;
- complex-conjugate matching, $Z_A = Z_L^*$.

In the reflection-less case the impedances of the amplifier and the load are equal, which minimizes deleterious power reflections along the circuit, while in the other case the matching is set in order to have the amplifier impedance equal to the complex conjugate of the load impedance Z_L^*, which maximizes the power transfer between the two at a given operating voltage. If both Z_L and Z_A are real the two conditions coincide.

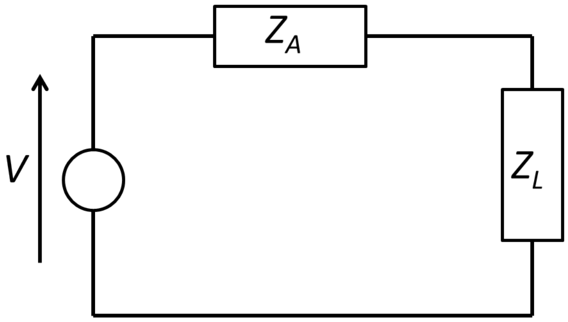

FIGURE 2.2: Scheme of the real voltage supply connected to a load.

The employed amplifiers are often derived from industrial applications usually present a fixed 50 Ω or 70 Ω purely resistive output impedance, thus requiring a way to adapt the impedance of the load, which will typically present both resistive and reactive components and will have a different modulus; this, in Helicon plasma sources, is usually [10, 11, 16] accomplished by variable reactive elements (capacitors or inductors) inserted in the circuit between the antenna and the amplifier, thus realizing a matching network capable of presenting a purely resistive 50 or 75 Ω impedance to the amplifier at the desired operating frequency (usually 13.56 MHz).

The RF system developed at CISAS was designed with flexibility as the main goal, thanks to the following elements, which can be observed in Figure[2.3]:

- an HP 8648A signal generator, capable of operation in the 100 kHz - 1 GHz range;
- an RF amplifier, which can be chosen between two models, covering different frequency ranges:
  - an water-cooled ENI OEM-12B3-02 linear amplifier (8-30 MHz, power up to 1250 W);
  - a Spin HFPA-30 linear amplifier (1.8-30 MHz, power up to 300 W). In this case a low power (4-10 W)pre-amplifier is needed to elevate the signal generated by the generator to the level required to trigger the amplifier. This role can be covered by an IntraAction PA-4 class A amplifier (4 MHz or more) or by a custom built linear amplifier (4 MHz - 100 KHz).

- a custom-built matching box, composed of two variable high vacuum capacitors, connected as illustrated in Figure[2.4], and characterized by a capacitance ranging up to 1250 pF each.

All the cables are coaxial: typically those carrying low power signals are of the RG-58 type, while power is carried by RG-213s and RG-214s, but custom coaxial cable were manufactured and employed as well for special applications. All the connectors are either BNC or N-type ones.

A set of voltage and current probes (VI modules, Figure[2.5]), manufactured by RESIA, a partner of CISAS during HPH.Com, can be placed along the RF network; the modules generate two voltage signals, each one proportional to the voltage and current flowing in the RF network, which are plotted on a Siglent SDS-1102CML digital oscilloscope, thus allowing to estimate both the power coupling and the complex impedance seen at the chosen circuit locations. In the case of sinusoidal V/I waveforms power and impedance can be asily estimated as $P = 1/2 \cdot V \cdot I \cdot \cos\Delta\phi$ and $Z = V/I$, where V and I are the peak values of voltage and current and $\Delta\phi$ is their relative phase angle; if, however, the waveforms present spurious harmonics the oscilloscope plots can be saved as .csv files and post-processed. In this case the samped voltage and current plots, $\mathbf{V}(t)$ and $\mathbf{I}(t)$, are employed to calculate the effective power as $P = 1/n \cdot \sum_{i=0}^{n} \mathbf{V}(i) \ \cdot \mathbf{I}(i)$, where n is the number of sampled points. Impedance is approximately estimated as $Z = \max(\mathbf{V})/\max(\mathbf{I})$. The overall uncertainty associated to the measurement of voltage, current and phase angle is estimated at $\pm$ 5%; from these values the uncertainties of power and impedance measurements were estimated via the Monte-Carlo method: a set of 1500 estimations of Z and P were performed by inserting in the related expressions randomly variable values of I, V and $\Delta\phi$ around set mean values, assuming for each parameter a Gaussian error distribution. The resulting Z and P distributions were then analyzed in order to estimate their mean values, Z_{avg} and P_{avg}, and the respective standard deviations σ_Z and σ_P. The uncertainty associated to Z and P was then calculated assuming a 3σ confidence interval, resulting in both cases $\leq$ 8 %. It was thus decided to assume this value as the uncertainty for both estimations.

2.2 Thruster laboratory models

2.2.1 External experiment

The external experiment was designed in order to be almost completely reconfigurable, under the point of view of geometry, RF antenna, magnetic system and employed gas;

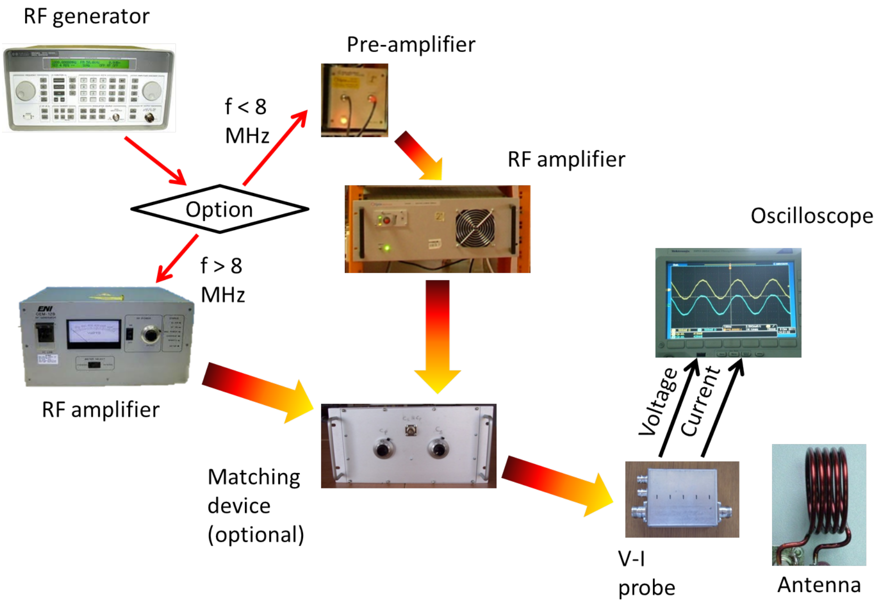

FIGURE 2.3: Complete scheme of the RF system.

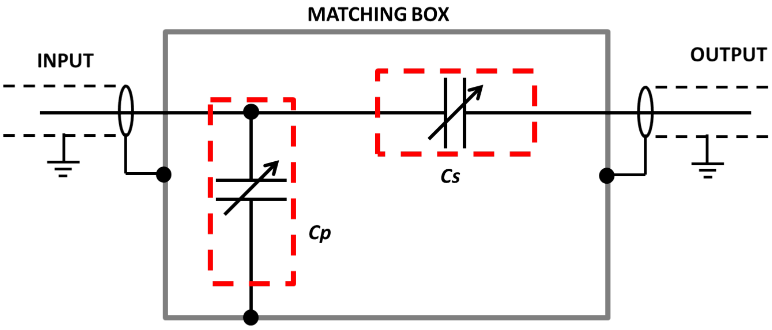

FIGURE 2.4: Equivalent electrical scheme of the matching box. Cp and Cs are respectively the parallel and series capacitors.

in order to enable a quick and easy change of its key features the model is mounted outside the vacuum chamber, to which it is connected through the gate valve. The main elements are:

- a Pyrex tube, acting as the discharge chamber into which the plasma is generated;
- a Pyrex bell, connected to the plasma source at one end ant to the gate valve of the vacuum chamber on the other end. Through the bell the plasma exhaust expands before reaching the vacuum chamber, thus allowing both visual observations and access for plume diagnostics;
- the RF antenna, wrapped around the discharge chamber and axially movable along it;

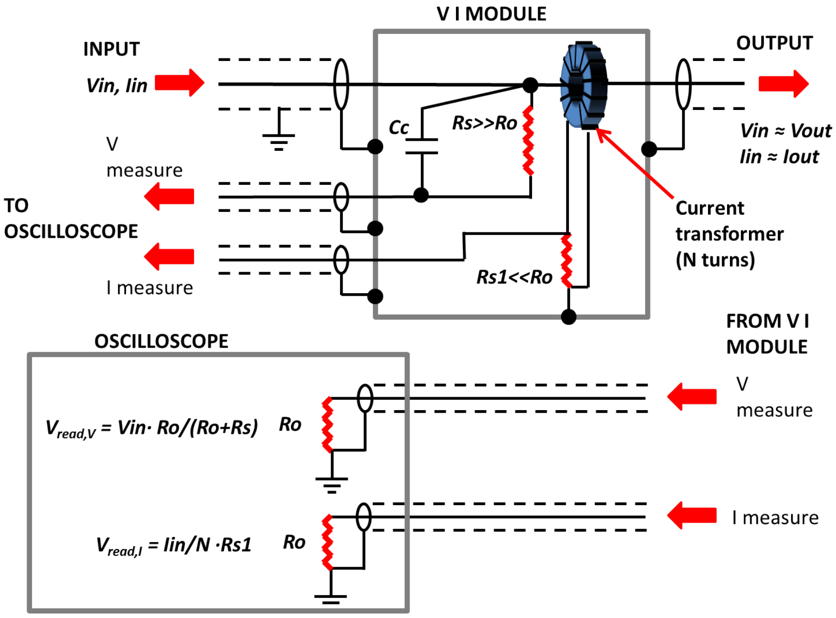

Figure 2.5: Scheme of the VI module. The voltage is sensed by means of a compensated resistive partitor (compensation capacitance Cc), while current is measured by means of a current transformer with an high permeability core.

- a magnetic system, either composed of electromagnets or permanent magnets, mounted on axially mobile carriages sliding on an axial rail;
- an injection system, composed of a stainless steel tube tipped by a ceramic head, which is inserted inside the discharge chamber and mounted on a mobile carriage in order to allow for plasma source length regulation. An MKS 1179A01311CS1BV mass flow controller is employed to regulate the gas flow inside the plasma source (maximum mass flow rate: 11 SCCM, N_2 equivalent). The controller can work with a wide variety of different gases;
- a set of ceramic outlet disks, featuring different opening diameters.

Table[2.1] reports the key geometrical features of the experiment, which is portrayed in Figure[2.6].

Parameter	**Value**
Discharge chamber length	0 - 200 mm
Outlet diaphragm diameter	5-10-15-19 mm
Discharge chamber inner diameter	19 mm
Magnets-outlet flange distance	25-250 mm

Table 2.1: Geometrical parameters of the experiment

The magnetic system, in particular, can be composed of up to four elements, mounted in pairs on axially movable carriages, which can be chosen among the following:

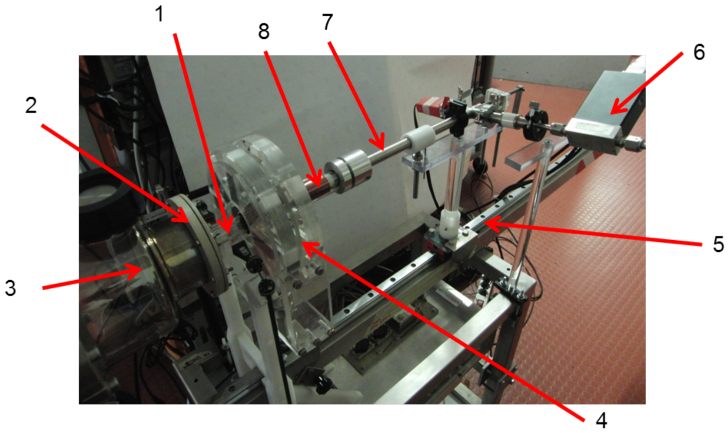

FIGURE 2.6: Overall scheme of the RF system. 1: discharge chamber. 2: outlet flange. 3: Pyrex bell. 4: magnetic system. 5: axial rail. 6: mass flow controller. 7: injector tube. 8: RF antenna.

- up to four electromagnets (Figure[2.9]), each composed of a copper coil counting 624 windings (wire diameter $\phi_w = 2$ mm) contained within a Teflon casing. Each electromagnet can be independently fed by a separate DC power supply and can produce at its center an axial magnetic field of approximately 40 gauss for each ampere of input current.

- up to four SmCo permanent magnets rings, each with up to three layers of magnets. The choice of SmCo was dictated by its very high maximum operating temperature (up to 473-523 K), which mitigates thermal issues, while the double radially-polarized rings configuration (Figure[2.7]) has resulted from the optimization process. Each ring was built employing 8 cubic Sm_2Co_{17} blocks (20x20x20 mm), encased in radially-slotted Plexiglas disks. The mean axial field developed by the magnets in the plasma source region, mapped by means of an Hall effect gauss-meter (Figure[2.8]), resulted to be near 700 G.

2.2.2 Vacuum Model

During the later stages of project HPH.COM the necessity of (i) taking steps towards the development of a real-scale miniaturized thruster and (ii) validating the results of the external experiment in conditions more representative of the intended operating environment of the thruster led to the development of a second laboratory model, specifically designed to operate completely immersed in vacuum. The model is highly reconfigurable and allows to reproduce all the configurations tested on the external experiment with additional geometric flexibility; Figure[2.10] portrays the model mounted inside the vacuum chamber: its structure is composed of a base flange (ϕ=145 mm), connected to

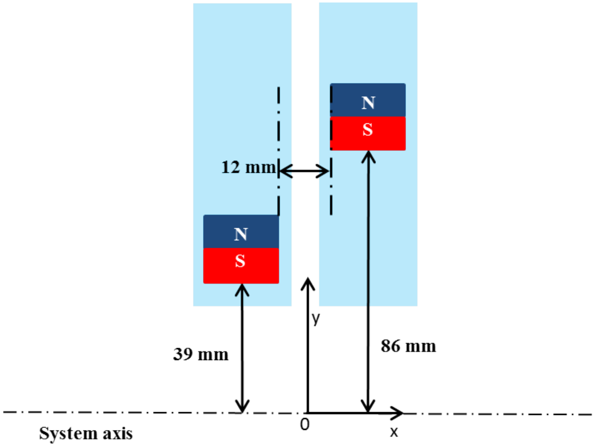

Figure 2.7: Magnetic rings geometry and polarization

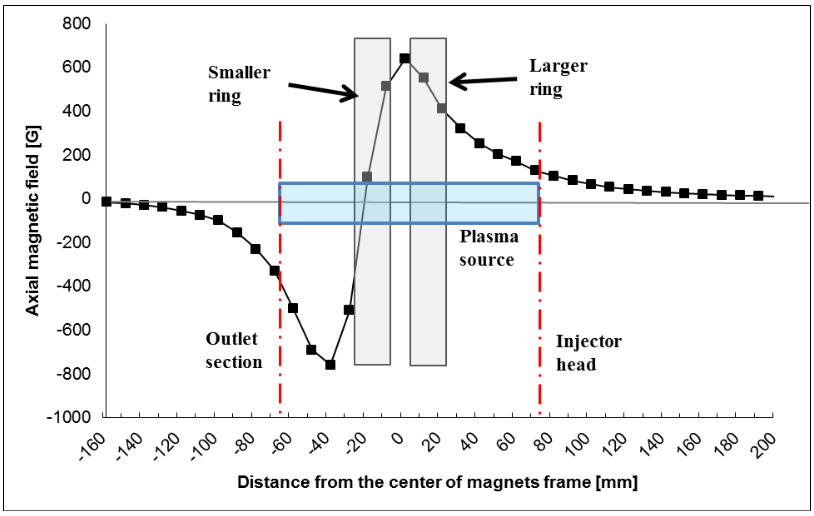

Figure 2.8: Axial component of the magnetic field produced by the permanent magnets

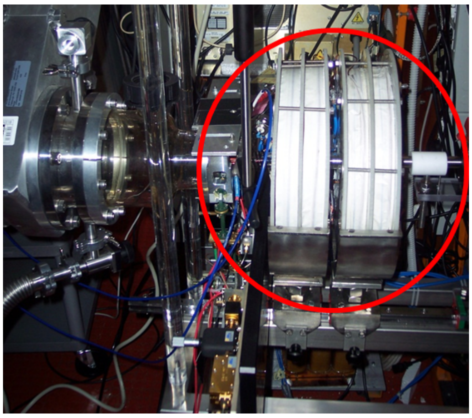

Figure 2.9: The electromagnets (circled) mounted on the experiment.

four lateral bars. The Pyrex discharge chamber,with the antenna wrapped around it, is directly connected to the flange, while the magnets are fastened to the lateral bars. It can be observed that the Pyrex chamber terminates with a conical baffle, which was

inserted in order to screen the rest of the thruster from eventual back-flows of chargedt particles and to provide an optimal neutral gas pressure profile in oder to favor the ionization process. All the structural elements are made in PEEK, an high strength, high temperature polymer chosen for its robustness and high maximum operating temperature, the latter being particularly critical during operation in vacuum.
The magnetic system is based on two radially polarized Sm_2Co_{17} rings, each composed of six wedge-shaped elements encased in PEEK mountings. Again SmCo was favored due to thermal considerations, with PEEK, being a thermally insulating material, providing additional protection from the waste heat produced by the plasma source. The magnets are smaller than their external counterparts (ϕ_{inner}=28 mm, ϕ_{outer}=37.5 mm, length=25 mm) but are capable of producing a similar magnetic field, both in shape and intensity.

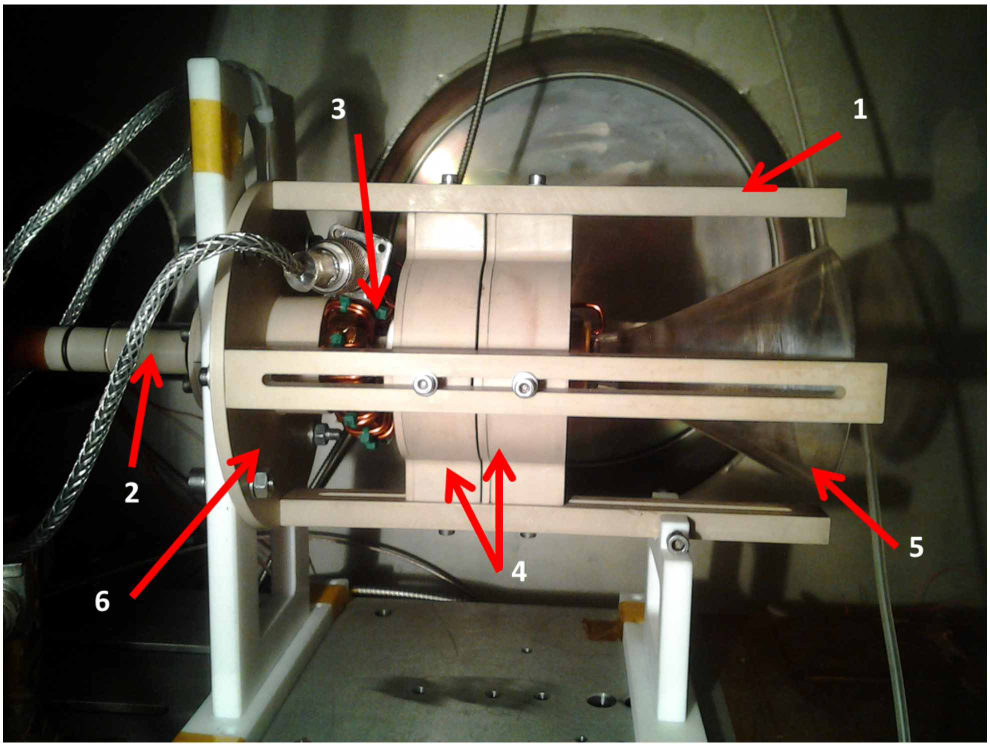

FIGURE 2.10: Thruster vacuum model. 1: PEEK lateral bar. 2: injector. 3: antenna. 4: magnets. 5: discharge chamber with nozzle screen. 6: PEEK base flange.

2.3 Plasma Diagnostics

An array of plasma diagnostic systems is available for the characterization of the HPT, including:

- a microwave interferometer for plasma density (n_e) measurements ;

- a set of optical spectrometers for plasma emission spectrum acquisition, which allows to estimate both the electron temperature (T_e) and the ionization ratio (η_i) of the plasma;
- a Faraday cup, which allows to monitor both ion flow ejected by the thruster ($\dot{m}_i$) and the plume divergence demi-angle (α_p);
- a set of CCD cameras, equipped with bandpass filters centered on the emission lines of Argon ions (488 ± 10 nm) and excited neutrals (752 ± 10 nm), employed for the analysis of the distribution of ions within the plasma discharge and for the estimation of the actual plasma column diameter within the discharge chamber, which is required for interferometric density measurements.

The data provided by these diagnostics are partially overlapping, in order to allow a cross-check of the measurements and, when combined, allow to estimate the performance parameters of the thruster, namely the specific impulse, I_{sp}, and thrust, T, c.
Each diagnostic system will be briefly introduced in the following subsections.

2.3.1 Microwave interferometer

The microwave interferometer available at CISAS (Figure[2.11]) was developed within project HPH.COM ([17]) and was specifically designed to deal with small and tenous plasmas, such as those generated by a low power helicon source. The operating principle of the device is the following: a 75 GHz microwave signal (λ=4 mm) is generated within the interferometer and split in two parts, one of which follows a reference path inside the instrument while the other travels along external waveguides which drive it through the plasma source, which generates a phase shift in the microwave beam whose entity depends on plasma density; the two signals are then compared by a phase detector, which measures the plasma-induced phase shift. The instrument can operate independently from the type of gas employed, thus providing a great operating flexibility. In addition this kind of diagnostic is not invasive, since it is placed outside the plasma source. The detector operates at 100 MHz, thus requiring the microwave signal to be modulated at such frequency. The device is installed externally to the vacuum chamber, on a sliding carriage which allows it to be moved axially along the plasma source. The external waveguides force the microwave signal through the plasma by means of two horns, spaced by 48 mm and with an opening of 10x15 mm. This installation, unfortunately, does not allow this instrument to operate inside the vacuum chamber, thus limiting density measurements to the external experiment alone. The interferometer is capable of detecting plasma densities in a wide range spanning from $10^{16}m^{-3}$ to $10^{19}m^{-3}$, which ensures an high operating flexibility.

If the plasma is modeled as an uniform slab of constant density and thickness placed between the horns the relation between the phase shift and plasma density necomes linear and can be expressed in a simplified form as in eq.[2.1]:

$$\Delta\phi = \frac{e^2}{4\pi c^2 \epsilon_0 m_e}\lambda \int_0^D n dl = 2.82 \cdot 10^{-15} \lambda D N \tag{2.1}$$

Here m_e and e are the electron mass and charge, c is the speed of light, ϵ_0 is the vacuum dielectric constant, λ is the microwave wavelength, n is the plasma density, N is the average plasma density and D is the actual plasma discharge diameter, whose value is experimentally measured as explained in 2.3.4. eq.[2.1] is valid within a 4% error up to a density of $1 \cdot 10^{19} m^{-3}$ and for a value of D ranging from 20 mm down to 8 mm (corresponding to 2λ), below which the relation becomes nonlinear. In this case approximated expressions can be employed, such as those expressed in eq.[2.2] and eq.[2.3], which are valid for D=6mm and D=7mm respectively.

$$\Delta\phi \approx 4 \cdot 10^{-20} N \tag{2.2}$$

$$\Delta\phi \approx 6.5 \cdot 10^{-20} N \tag{2.3}$$

During operation we adopted the following procedure in order to measure the phase shift produced by the plasma:

- while the plasma is turned on the interferometer is activated and set to continuously acquire the value of the phase angle in a 10 s time interval;
- during the acquisition the plasma is suddenly turned off by cutting the power supply to the antenna. This produces a steep ”jump” in the phase angle plot;
- the difference between the value of the phase angle before and after the turn-off gives the phase shift produced by the plasma.

The uncertainty associated to density measurements depends on several factors, namely the uncertainty on the actual size of the waveguide horns, the uncertainty on the actual plasma discharge diameter, the phase noise of the phase detector. As long as the linear relationship between the phase angle and plasma density holds the overall uncertainty on density measurements can be calculated from their estimated standard deviation, whose expression is derived from eq. 2.1 [18]:

$$\sigma_N = \sqrt{\left(\frac{\sigma_{\Delta\phi}}{QD}\right)^2 + \left(\frac{\Delta\phi\sigma_D}{QD^2}\right)^2} \tag{2.4}$$

with Q=$2.82 \cdot 10^{-15}$ λ and σ_D, $\sigma_{\Delta\phi}$ are the standard deviations associated to the plasma diameter and phase angle detection, whose values are 0.08 mm (see 2.3.4) and 0.02 rad respectively. This relation is valid in the hypothesis that the uncertainty associated to the value of Q is negligible with respect to those associated to the actual discharge diameter D and to the phase jump $\Delta\phi$, which is valid since Q depends on known physical constants and on the value of the wavelength λ, whose uncertainty is negligible due to the high stability of the microwave source. The uncertainty on density measurements becomes $3 \cdot \sigma_N$, for a 3σ confidence interval.

In the cases when the density-phase jump relation is no longer linear (small plasma diameters) the rigorous estimation of uncertainty becomes more complex and would require a more detailed geometric analysis [18] . A simplified estimation, however, can be performed as:

$$\sigma_N = \sqrt{\left(\frac{\sigma_{\Delta\phi}}{C}\right)^2 + \left(\frac{\Delta\phi\sigma_C}{C^2}\right)^2} \tag{2.5}$$

where C is coefficient multiplying the density in eq.s 2.2 and 2.3 and σ_C is the related standard deviation, estimated at ±5% in order to match the results of the more accurate uncertainty analysis reported in [18]. Also in this case the measurement uncertainty becomes $3 \cdot \sigma_N$.

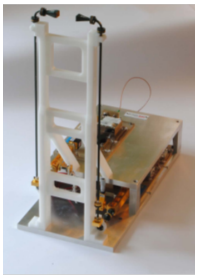

FIGURE 2.11: Microwave interferometer employed at CISAS. The two vertical waveguides terminate in two horns between which the plasma source is placed.

2.3.2 Optical spectrometers

A total of four digital optical spectrometers are currently available at CISAS the propulsion laboratory; all of them belong to the Ocean Optics USB series, characterized by a linear CCD sensor, easy operation through a dedicated computer software and customizable optical elements, namely the diffraction grating and the entrance slit,which determine both the operating range of the instrument and its wavelength resolution. Table[2.2] reports the key features of the devices.

Model	**CCD size** [pixel]	**Slit size** [μn x mm]	**Wavelength range** [nm]	**Optical resolution** [nm]
USB4000	3648	5 x 1	220 - 650	0.53 FWHM
USB2000$^+$	25 x1	2048	200 - 1100	1.84 FWHM
USB2000$^+$	25 x 1	2048	350 - 830	1.33 FWHM
USB2000$^+$	25 x 1	2048	350 - 830	1.33 FWHM

Table 2.2: Characteristics of the optical spectrometers.

The emission spectrum of the plasma is conveyed to the spectrometer through 400 μm core or 600 μm core optical fibers, which can be combined with dedicated joints or vacuum feedthroughs, allowing a great flexibility in the choice of the observed point both on the external experiment and on the vacuum model without requiring the spectrometer to be physically placed near the experiment. Measurements on the plasma inside the plasma source must be performed through the pyrex wall of the discharge chamber, which thus becomes a part of the optical path of the light. Typically the uncertainty on the detected spectral lines intensity can be contained within 5%, considering errors related to the calibration process, signal to noise ratio and spectrometers specifications [18].

Both the fibers and the discharge chamber wall act as filters affecting the passing light as a function of its wavelength, thus requiring the whole optical system to be calibrated before use; this is accomplished by means of an Ocean Optics DH2000 light source, featuring a deuterium lamp and a tungsten halogen lamp providing a known and stable calibration spectrum covering the whole operating range of the spectrometer; the lamp features a special SMA connector for optical fibers, in which a Pyrex slab can be placed in order to reproduce the effect of the discharge chamber wall. The slab can be positioned replicating the actual distance between the head of the optical fiber and the wall of the discharge chamber. Due to the effect of Pyrex, which blocks radiation with wavelength $\lambda \leq 250 - 300$ nm, measurements can be carried out only in the 270-1100 nm range.

The acquired spectra can be analyzed at two levels:

- at a preliminary level a dedicated Matlab script, developed at CISAS, is employed identify the emission lines of the plasma produced with the selected operating gas, classifying them according to the species they are emitted by (excited neutrals or ions). Usually for each gas it is possible to identify a set of lines, belonging to both excited neutrals and atoms, which are particularly evident with respect to others in the typical operating conditions. A series of intensity ratios between ion and excited neutrals lines, whose entity is indicative of the relative strength of ion vs neutral light emission, is calculated and employed as a qualitative estimation of the trend of the ionization efficiency of the plasma source during a series of tests. For example with argon as the operating gas the script calculates four ArII to ArI lines ratios, based on five emission lines: 420, 452.2, 355.9, 434.8, 488 nm; the first couple of values corresponds to an argon excitation level while the last three values identify the ionized argon. The lines were selected due to their relatively high intensity with respect to others in the typical operating conditions. From the intensity of these emission lines the ratios E(355.9)/E(420), E(434.8)/E(420), E(488)/E(420), E(488)/E(452.2) are calculated and employed for a qualitative comparison of ionization level between different tests, which is considered attendible if all the ratios show an equal trend. This analysis is based on the simplifying hypothesis of a plasma in local equilibrium both along the axis and across the section, which cannot be considered fully valid in an HPT [19]. This, however, does not hamper the possibility of using the aforementioned ratios for qualitative comparison on the propulsive performances. Similarly to what was done in 2.1.2, the uncertainty associated with lines intensity ratios was estimated by means of a Monte-Carlo simulation (2000 trials), resulting in an overall value of 8% for a 3σ confidence interval;

- at a deeper level the spectra are elaborated by means of a Collisional-Radiative Model (CRM) of the employed gas [19], in order to estimate plasma temperature, plasma density and ionization rate. The results can be cross-checked with the plasma density measurement carried out through the interferometer, thus providing a more reliable estimation of the properties of the plasma inside the thruster.

Spectrometers are, like the interferometer, non intrusive diagnostics characterized by a great flexibility; unlike the previous device, however, their performance is more directly related to the choice of the operating gas, since, for the sake of the CRM analysis, their operating wavelength range must include the emission lines of interest, which must be resolved with sufficient accuracy.

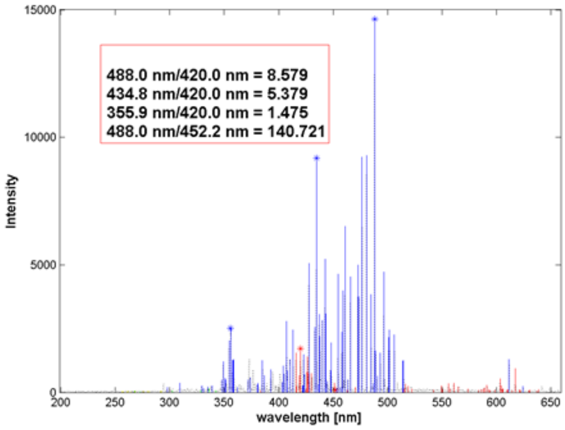

FIGURE 2.12: Example of elaborated Argon plasma spectrum. Red lines are related to excited neutrals, while blue ones are emitted from Ar^I ions. The strong prevalence of blue lines is indicative of an highly ionized plasma. In the text box a series of selected lines intensity ratios are calculated.

2.3.3 Faraday cup

The Faraday cup, so called after Michael Faraday, who first theorized the existence of ions, is an electrostatic device intended to collect charged particles in a vacuum and, in its simplest form, is typically composed of a polarized plate directly immersed in the flow of particles. In our case this device is employed to estimate the ion flow $\dot{m}_i$ ejected by the thruster, which is indicative of the ionization rate η_i:

$$\eta_i = \frac{\dot{m}_i}{\dot{m}_t} \tag{2.6}$$

where $\dot{m}_t$ represents the total mass flow rate of gas injected in the thruster. This estimate can be compared with those coming from the analysis of the emission spectrum and from interferometer measurements as an additional cross-chek, leading to an increased reliability of the measurements.

The Faraday probe available at CISAS, developed during HPH.COM, is structured as shown in Figure[2.13]: a ϕ=3 mm polarized nickel plate is employed as the collector, encased in a stainless steel cylinder which acts as a guard ring, granting a more uniform sheath around the collector when immersed in the plasma. The collector and the ring are electrically insulated; the ring is usually grounded, while the collector is connected to dedicated analog conditioning and acquisition electronics which measures the incoming ion current I_p, giving a corresponding voltage output $V_r = K \cdot I_p$, with K the gain; K is selectable and ranges between 1 and 1000 V/mA. V_r is read by a digital multimeter, with an accuracy of ±0.1 mV. Since the plasma ejected from the HPT is quasi-neutral, that is, the ion and electron fluxes are equal, a negative DC voltage bias is required in order to repel all the incoming electrons, thus ensuring that only ions are collected.

This condition is granted by progressively lowering the negative bias of the collector, V_p, enough for the ion current to enter a saturation regime, in which it becomes theoretically constant as the voltage is further lowered [8]:

$$j_{i,sat} = e\dot{n}_e\dot{c}_s \tag{2.7}$$

$$c_s = \sqrt{k_B \cdot (ZiT_e + \gamma_i T_i)/m_i} \tag{2.8}$$

Here $j_{i,sat}$ is the specific ion saturation current, c_s is the Bohm sound speed in the plasma, k_B is Boltzmann's constant, Z is the average ion charge state, m_i is the ion mass, T_e and T_i are the electron and ion temperatures respectively and γ_i is the adiabatic coefficient for ions.

The saturation curve of our Faraday probe is shown in Figure[2.14] with the Ar plasmas used in HPH.COM: it can be seen that a "true" saturation is never reached by the experimental data, due to an electrostatic focusing effect which, for increasingly negative V_p, tends to deviate the ion trajectories towards the probe, effectively increasing its capture area. In order to compensate this effect an ad-hoc Matlab script was developed within the early stages of this work (see A), capable of estimating the focusing efffect factor $fe = A_{p,eff}/A_{p,geom}$, where $A_{p,eff}$ is the effective probe collection area and $A_{p,geom}$ is the geometric area of the collector: by correcting the acquired data it can be seen that saturation occurs with $V_p \approx -50V$. As a a safety measure, we usually set V_p well beyond the saturation point, at around -150 V. Another source of error can come from secondary electrons emitted from the collector plate as primary particles impact its surface; this issue was mitigated through the use of nickel, which is characterized by a low secondary electron emission yield [20]; the effectiveness of this measure appears to be testified by the fact that the application of the electrostatic focusing correction is sufficent to achieve a constant ion current in the saturation regime, thus indicating that the contribution of secondary electrons is negligible in the tested conditions. The polarization of the plate, V_p, is provided through the acquisition electronics by a DC voltage supply.

The probe is mounted inside the vacuum chamber on a two-axis micrometric moving system, placed downstream the thruster, allowing the 2D mapping of the ejected plasma beam and thus the estimation of its mean divergence half-angle, α_p.

The calculation of the total ejected ion current can be calculated by integrating the measured radial current density profile over the corresponding circular area:

$$I_{tot} = \frac{1}{f_e}\int_0^R \int_0^{2\pi} \frac{I(r)/A_{p,geom}}{\cos\phi(r)} \cdot r d\theta \cdot dr = \frac{I_{geom}}{f_e} \tag{2.9}$$

where R is the radius of the scanned area, I_r is the experimentally measured current and $\phi(r)$ is the view angle between the probe and the plasma streamlines radiating center, which does not necessarily coincide with the outlet diaphragm of the thruster, due to the presence of a strong magnetic field which causes the plasma streamlines to diverge slightly as the plasma is expanded by the magnetic nozzle. With reference to Figure[2.15], the total plume divergence half-angle is calculated as $\alpha_{T,p} = \arctan{(r_{max} - r_{cone})/d_{pt}}$, with r_{max} the radius at which the detected current is $\leq 5\%$ of the current measured in the middle of the plume, r_{cone} the radius of the nozzle cone of the thruster and d_{pc} the distance between the probe scan plane and the nozzle cone; the distance of the probe scan plane to the radiating center of plasma streamlines can then be calculated as $d_{pc} = r_{cone}/\tan\alpha_{T,p} = r_{cone}/(r_{max} - r_{cone}) \cdot d_{pt}$, while the view angle becomes $\phi(r) = \arctan r/d_{pc}$. The uncertainty associated with current measurements mainly depends on two contributions: i) the uncertainty $\epsilon_{I,geom}$ due geometrical errors on probe alignment, positioning and size, and ii) the uncertainty ϵ_{focus} in the estimation of the focusing factor f_e, due to uncertainties in the estimation of ion mean energy, probe voltage bias and shielding effects. The uncertainty of the current detection electronics is ± 0.1 μA and can be considered negligible, since the detected currents typically range between a few μA and some hundreds of μA.

The uncertainty $\epsilon_{I,geom}$ can be quantified though a Monte-Carlo simulation as was done in 2.1.2, by calculating the uncorrected total ion current as:

$$I_{geom} = \int_0^R \int_0^{2\pi} \frac{I(r)/A_{p,geom}}{\cos\phi(r)} \cdot r d\theta \cdot dr \tag{2.10}$$

The parameters R, r, d_{pc}, r_{cone}, $\phi(r)$ and $A_{p,geom}$ were randomly varied according to the respective uncertainties, assuming in each case a gaussian error distribution and a 3σ confidence interval. Axial and radial distances are characterized by a ± 1 mm uncertainty, while the alignment of the probe and the thruster axis is achieved within ± 2°. The view angle $\phi(r)$ also depends on r, d_{pc} and r_{cone} and as such its uncertainty is given by the sum of the misalignment uncertainty and the uncertainty coming from errors in the radial and axial positioning and in the estimation of the nozzle cone diameter. The latter, as well as the diameter of the probe collection plate and its other dimensions, is known within ± 0.1 mm. A set of 233 Monte-Carlo iterations indicated that a value of $\epsilon_{I,geom} = \pm\ 8\ \%$ is enough to include all the typical operating conditions.

The estimation of focusing factor uncertainty resulted in an overall $\epsilon_{focus} = \pm\ 30\ \%$, as reported in A. The totall uncertainty on ion current measurement thus becomes:

$$\epsilon_I = \sqrt{\left(\frac{\epsilon_{I,geom}}{f_e}\right)^2 + \left(\frac{I_{geom}\epsilon_{focus}}{f_e^2}\right)^2} \tag{2.11}$$

Finally, the uncertainty associated to the estimation of the mean divergence half-angle of the plume, α_p was again estimated with a set of Monte-Carlo simulations (233 trials); the results indicate that an overall uncertainty of $\pm$ 10% can be conservatively assumed in order to guarantee a 3σ confidence interval in all the cases considered within this work.

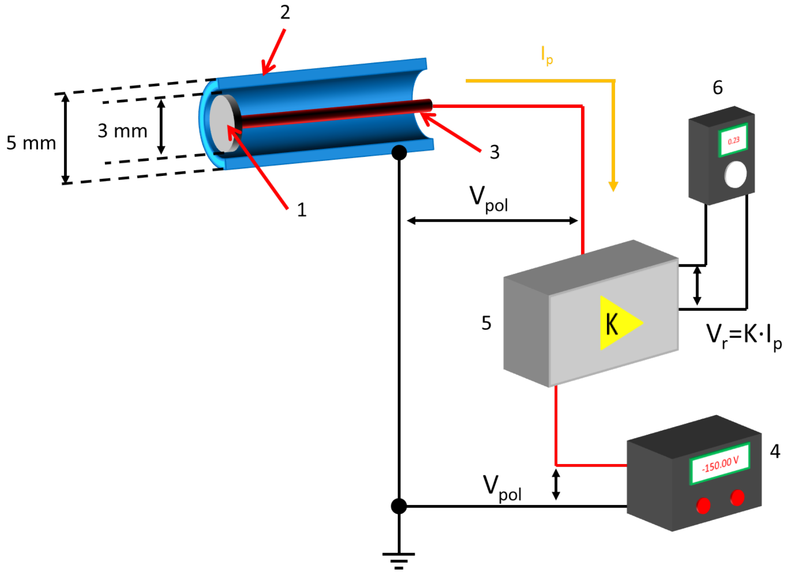

FIGURE 2.13: Scheme of the Faraday probe. 1: nickel collector plate. 2: steel guard ring. 3: internal conductor. 4: DC voltage supply. 5: acquisition electronics. 6: multimeter.

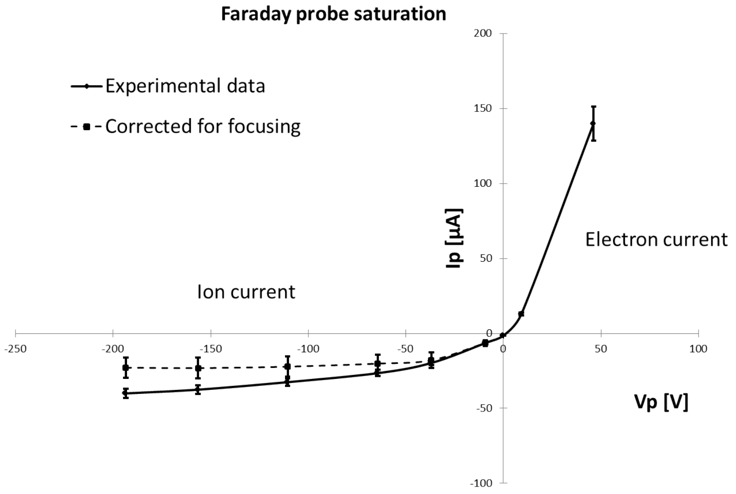

FIGURE 2.14: Saturation of the Faraday probe with the Argon plasma generated by a 50 W HPT. The ion current (negative values) is corrected for the electrostatic focusing effect. A saturation voltage of around -50 V was estimated. Uncorrected measurements do not incorporate the focusing factor f_e and are thus characterized by a lower uncertainty with respect to corrected values.

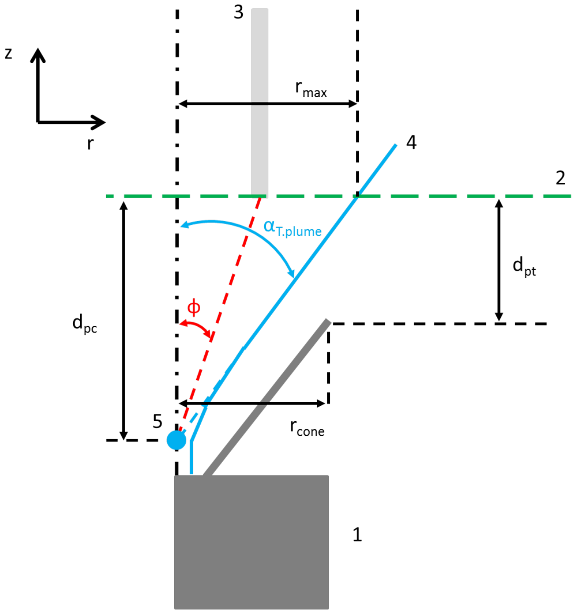

FIGURE 2.15: Scheme of radial plume scan with the Faraday probe.1: Helicon Plasma Thruster with conical baffle. 2: Faraday probe scan plane. 3: Faraday probe. 4: plasma streamlines. 5: plasma streamlines radiating center.

2.3.4 CCD cameras

Two Basler Sca1400-30FC cameras with a color CCD sensor of 1388x1038 pixels are available for the observation of the plasma. The cameras can mount focusing lenses and band-pass filters centered on the main ArI and ArII lines to monitor the distribution of ionized and excited particles within the source and the plasma beam. Two band-pass Omega Optical filters with a band width of 10nm are available for this purpose: i) a filter with a central wavelength equal to 488nm for ArII detection and ii) a filter with a central wavelength equal to 751nm for ArI detection.The choice of Argon emission wavelengths is due to the fact that the filters were acquired for project HPH.COM, which featured an Ar-fed HPT, but this does not preclude the employment of such tools for other gases, such as CO_2, provided that they present observable emission lines within the band allowed by the filters (see 5.3).

The main use of the filtered cameras is the determination of the actual diameter of the plasma column within the discharge chamber, which is required for the determination of plasma density from interferometric measurements as explained in 2.3.1. This analysis is necessary since the diameter of the plasma column is usually much smaller than the inner diameter of the discharge chamber.

The task is accomplished by taking a series of pictures of the plasma source, both filtered and unfiltered, centered on the zone in which the horns of the interferometer are placed:

- the camera is placed at a fixed position, in order to observe the zone of the plasma source in which the horns of the interferometer are placed. The focusing lenses are adjusted in order to achieve a nitid picture and then blocked;

- an unfiltered image is acquired before the beginning of the tests with the plasma and post-processed to determine the scale of the picture in mm/pixel;
- for each test the plasma discharge is photographed through the filter centered at 488 ±10 nm;
- each filtered picture is then numerically analyzed, determining the diameter in pixel of the plasma column. This value is then converted in mm according to the scale derived from the unfiltered picture.

The pictures are processed with the help of Matlab; filtered images of the plasma column, in particular, are converted black and white pictures through a thresholding process, in which the plasma column is identified as the zone in which the light intensity is ≥ 1 % of the peak intensity detected in the whole image.
The uncertainty associated with this process is related to i) the uncertainty of the reference length employed for scale determination, which is ± 0.1 mm, ii) the variation of the plasma column diameter along the axial direction and iii) the uncertainty associated with the thresholding process. While a precise estimation of the overall uncertainty is difficult experience indicates that a value of ± 0.25 mm can be considered sufficiently conservative.

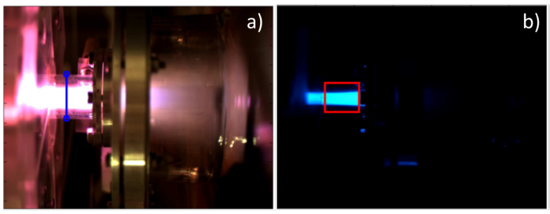

FIGURE 2.16: Example of the estimation of the actual plasma column diameter via CCD images, carried out on the HPH.COM plasma source. a) unfiltered reference picture, used to determine the scale in mm/pixel: the blue line corresponds to the known length of 24±0.1 mm, corresponding to the outer diameter of the Pyrex discharge chamber. b) filtered plasma discharge picture: the red box indicates the zone of the picture which is considered for the diameter determination. In this case the scale results to be 0.105 mm/pixel,while the plasma discharge diameter is estimated at 9.2 ± 0.24 mm.

Chapter 3

Numerical Modeling of the RF antenna

One of the key objectives of this work is the analysis, optimization and design of the RF system for Helicon Plasma Thrusters; one of the key aspects of this topic is represented by the electrical performance of the RF antenna, under the points of view of (i) operating frequency, (ii) input impedance and (iii) power efficiency, since:

- the first two points directly affect the design of the PPU devoted to the production of RF power (6);
- the third point gives a measure of how efficiently the power produced by the PPU is conveyed to the plasma.

In general the analysis of antenna performance must also include the effects of any other connection element placed between the antenna itself and the amplifier, such as voltage/current probes or cables. The former can usually be ignored, since, through a proper design, their impact on the overall electric performance of the system can be made negligible; the impact of connection cables may be neglected as well in a flight propulsion unit, since in the final design their length can be miminized, but, for laboratory experiments, this may not be always possible.

A considerable amount of work during this PhD thesis was devoted to the development of a lumped-parameters model of the RF Network, implemented in the well known Simulink environment, which allows both frequency-domain and time-domain simulations. The model is composed of elementary blocks connected together according to the equivalent electrical schemes of the various components, which include the antenna itself and all the elements connected between it and the RF amplifier feeding it, such as cables or matching devices, along of course with the plasma. All elements are modeled according to their actual physical structure, in order to provide a simulation as close as possible to their real behavior; the only exception is the plasma, which is modeled employing an equivalent plasma impedance according to the electrical effects that it produces on the antenna.

The model of each component was verified by checking that its frequency-domain characteristics (complex impedance as a function of frequency $Z(f)$) qualitatively reproduce those of the corresponding real component, measured by means of a network analyzer. The parameters of each block must then be calibrated in order to achieve also a quantitative match.

The verification and impedance tuning process also grants that the main output of the program, that is, the power coupled to and dissipated by each element, is validated; indeed, with reference to a generic k-th element, the coupled power is given by:

$$P_k = \frac{V_k^2}{Z_k} = \frac{V_k^2}{R_k + i \cdot X_k} \tag{3.1}$$

$$P_k = P_{eff,k} + i \cdot P_{ref,k} \tag{3.2}$$

If, for a given input voltage V_k, the complex impedance Z_k of the simulated component equals that of the real component, the coupled power P_k will also be the same, both in its *active* component $P_{eff,k}$ and in its *reflected* component $P_{ref,k}$. The current circulating in the component will of course be the same as well, since $I_k = V_k/Z_k$. This, however, cannot be directly applied to case of the net power coupled to the plasma, since this quantity is not directly accessible experimentally. The validity of such estimation, in fact, can only be inferred from the following considerations:

- the model is tuned in order to reproduce the characteristics of a given antenna;
- the antenna is characterized both numerically and experimentally without plasma, that is, in a condition in which all the power that it absorbs is dissipated by its parasitic resistances;
- if the estimated and measured power absorption coincide it is assumed that the parasitic resistances of the antenna have been correctly tuned;

- it is assumed that, during operation with the plasma, the electrical parameters of the antenna do not vary, thus meaning that any additional resistive/reactive elements altering the impedance (and thus the power absorption) of the antenna are due to the plasma alone. This assumption can be considered valid if the temperature of the antenna does not increase significantly due to the waste heat generated by itself and by the plasma source, that is (i) for short duration tests and (ii) after the thruster has reached its nominal temperature.

An other possibility lies in the employment of the net power estimation as an input of other plasma simulation codes; if the predicted plasma characteristics (in particular plasma density, which in CISAS set-up is easily accessible under an experimental point of view) agrees with the measured ones, the power estimation can be considered valid.

Once the verification and calibration process has been performed the model can be employed (i) in time domain, to estimate the power fluxes within the system, that is, to identify the source of parasitic power loss and to calculate the net power coupled to the plasma and (ii) in frequency domain, to analyze the impedance and phase angle of a given antenna with respect to frequency. With these indications the model becomes a simple yet powerful tool which can be employed in order to characterize existing antennae and, through the identification and minimization of power losses, optimize their design.

The sole lumped-parameters model cannot be employed for the design of a completely new antenna, since it needs to be calibrated with the characteristics of the antenna itself; the latter, however, can be preliminarily designed by means of a Finite Elements Method (FEM), which, starting from antenna geometry and materials, can be used to estimate its equivalent electrical scheme, to be then employed in the lumped-parameters model. The predictions of this method are affected by a greater degree of uncertainty with respect to the analysis of an existing antenna, but can provide an useful starting point for the manufacturing of a first prototype which can be progressively optimized.

3.1 Lumped-parameters models

3.1.1 RF Antenna

The RF antenna is modeled as a network of discrete inductances, capacitors and reactances, according to its equivalent electrical scheme. These elements are tuned in order to reproduce the complex impedance of real antennae both in frequency-domain and in time-domain,

- the values of inductances and capacitances are measured by means of an LC meter or estimated theoretically;
- the parasitic resistances are adjusted in order to match the impedance modulus.

Resistances, in particular, are in fact frequency-dependant (see 3.2), but are in general much smaller than reactances in the usual antenna designs and thus their variation with frequency can be neglected.

A typical example of antenna model is reported in Figure[3.1]: in this case the antenna is a simple inductive one, with an inductance L, a parasitic capacitance C and a parasitic resistance R. Such circuit in fact experiences a resonance for a frequency$f = 1/(2 \cdot \pi \cdot \sqrt{LC})$, in correspondence of which its impedance experiences a peak whose amplitude tends to infinite and is limited only by the entity of the parasitic resistance R. Along with this scheme other antenna configurations are possible, choosing different arrangements and values of the reactive elements, while resistive ones usually constitutes an undesired side-effect of real conductors.

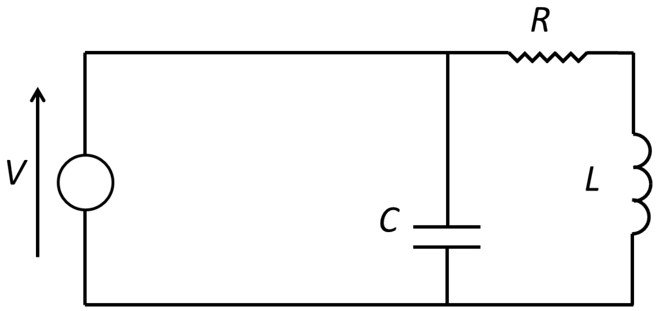

FIGURE 3.1: Equivalent electrical model of an inductive antenna.

The verification of the model was performed by comparing the frequency-domain characterization of the simulated antenna, in terms of impedance modulus and phase angle, to the corresponding experimental parameters of a real inductive antenna, resonating near 4.8 MHz due to its parasitic capacitance. The experimental data was taken by means of a DG8SAQ 2.6 vector network analyzer, calibrated to 1 % accuracy, and were employed as a benchmark for the tuning of the electrical parameters of the model. The result is shown in Figure[3.2] and Figure[3.3]: the frequency-domain characterization of the real antenna is matched by numerical data within 6.5 % in the case of impedance modulus and wihtin 9 % in the case of the phase angle. The relative error is smoothed over a 500 kHz interval in order to cancel false error peaks in correspondence of the resonances, where small absolute errors can generate great relative errors:

$$err_{A,smooth}(f) = \left[\int_{f-\Delta f/2}^{f+\Delta f/2} (err_A(f) \cdot A(f)df)\right] / \left[\int_{f-\Delta f/2}^{f+\Delta f/2} (A(f)df)\right]. \tag{3.3}$$

where A represents the parameter to which the error is referred (impedance modulus or phase angle).

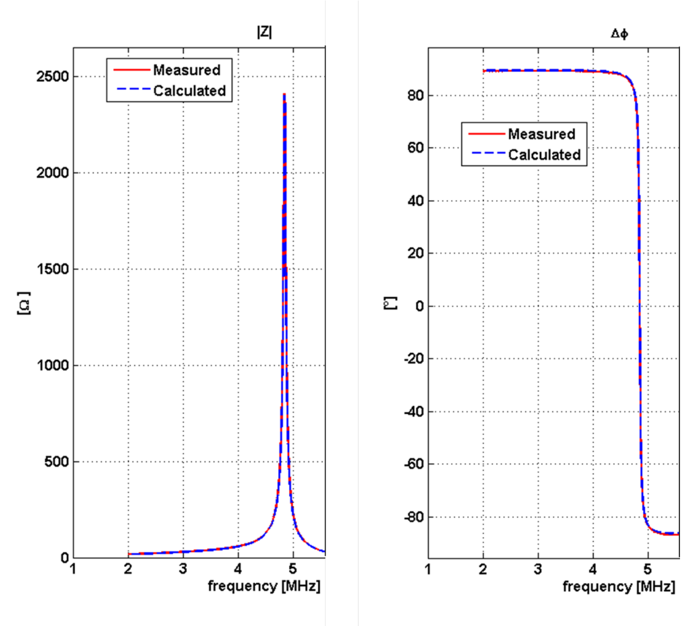

FIGURE 3.2: Model verification: reproduction of the frequency-domain characteristics of an inductive antenna. The matching between simulations and experimental data is clearly observable.

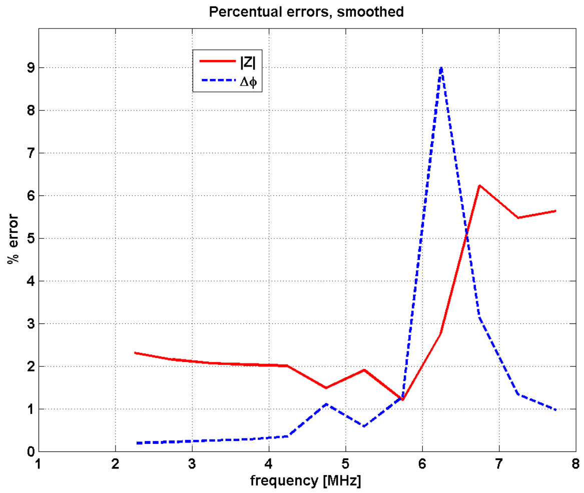

FIGURE 3.3: Antenna model verification: relative error of the esimated impedance modulus and phase, smoothed over a $\Delta f = 500$ kHz interval.

3.1.2 Plasma model

The analysis of the antenna model in 3.1 was performed without taking into account the effect of plasma on the overall performance of the antenna, which is equivalent to analyze the device when operating without a load. In fact the experience gained during experimental activity shows that the presence of plasma produces significant alterations on the electrical behavior of the antenna, under the following points of view:

- the reactive part of antenna impedance experiences an increase with respect to operation with no load. The entity of this variation depends on the antenna and to the operating conditions;
- the impedance modulus of the antenna experiences strong variations (up to a factor of 10-20).

The entity of these effects varies from antenna to antenna and, for a given device, appear to depend mostly on plasma density and temperature (and thus from the power level). In order to rigorously model this behavior an accurate analysis of the antenna-plasma interaction shall be carried out, but this would have resulted in an over-complication which goes beyond the scope of the lumped-parameters model. The latter, as already stated, has the purpose of analyzing the power fluxes inside the RF antenna and its electrical behavior, meaning that, under this point of view, it is enough to model the plasma as an equivalent plasma impedance $Z_p = R_P + iX_P$, to be inserted in the equivalent circuit of the antenna and tuned in order to reproduce the experimentally observed ω_r and Z_{max}. Assuming that the antenna has not changed its electrical parameters with

respect to the case without plasma, this allows to estimate the effective active power coupled to the plasma as the power dissipated by R_P with a time-domain analysis. This hypothesis in fact holds when the simulation is performed with fixed operating conditions (and thus fixed frequency and temperature).
The phenomenological reproduction of the electrical behavior of the antenna in presence of a plasma can be achieved by means of two simple schemes, illustrated in Figure[3.4]: as it can be seen Z_P can either be inserted in series to the antenna or in parallel to it; both models are capable of reproducing the effects of a plasma on a given antenna, of course with different required values of R_P and X_P. The power fluxes estimated with both models are the same, since:

- the overall antenna impedance is the same in both cases and thus the total absorbed power will be the same for given voltage and frequency;
- from the consideration above it is possible to infer that the coil and parasitic resistance will be crossed by the same current in both cases and thus the parasitic power dissipation will be the same;
- with the same overall power coupled and the same power dissipation in both cases, also the power coupled to the plasma will be the same.

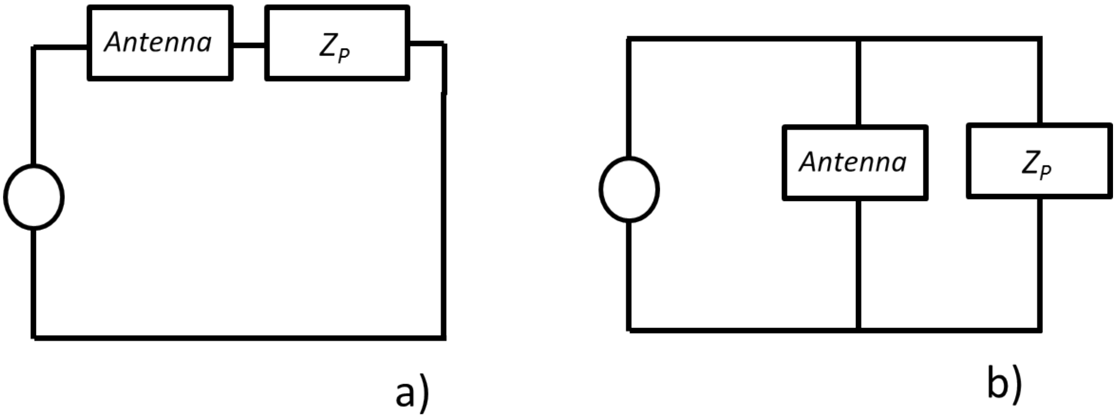

FIGURE 3.4: Plasma impedance models. a) in series with the antenna. b) in parallel with the antenna.

3.1.3 Cables model

Cables can be considered a minor issue in the analysis of the antennae, especially since their length, and thus their effect, would be minimized in a true flight propulsion unit. In laboratory analyses, however, their effect may become sensible, especially when, for mounting issues, the V/I probes cannot be directly attached to the antenna.

All the cables used in our experiment for RF applications are coaxial cables, which are composed of an inner conducting core and an external conducting jacket, phisically insulated by a ring of dielectric material put between them (Figure[3.5]). The outer jacket, which is usually grounded, virtually confines all the electric field within the cable. This means that coaxial cables can be bent and twisted without consequences on the signal they carry and that they effectively screen the inner conductor from external ones and vice versa.

A coaxial cable may be easily modeled as a transmission line [21], as shown in Figure[3.6]: the cable is composed of an ideally infinte series of RLC circuits , each representing an infinitesimal length. The parameters R_c, G_c, L_c and C_c are the distributed resistance, inductance and capacitance of the cable, respectively expressed in Ω/m, S/m, $\mu H/m$ and pF/m. This approach can be adapted to a lumped-parameters model: for a given frequency, it will be enough to discretize the cable with a sufficient number of RLC elements, each of which will have a finite resistance, inductance and capacitance calculated as $\delta R = R_c \cdot \delta l$, $\delta L = L_c \cdot \delta l$ and $\delta C = C_c \cdot \delta l$, where δl is the length of a single cable element. The size of the single element depends on the frequency and can be determined by means of a sensitivity analysis, in which a cable of a given total length L_c is discretized with a progressively higher number of elements and subject to a frequency domain analysis, until no change in the output of the simulation is achieved. Table[3.1] are reported the typical electric parameters of the commercial coaxial cables most commonly employed at CISAS: these belong mainly to two types, the smaller RG-58, rated for a maximum voltage of 1900 V DC and used for signal transmission, and the bigger RG-214, rated for 25 kV DC, used for power transmission. As it can be seen from a parameter defined *characteristic impedance* is indicated: this is the ratio of the amplitudes of voltage and current of a single wave propagating along the line:

$$Z_0 = \sqrt{\frac{R + i\omega L}{G + i\omega C}} \tag{3.4}$$

Since usually G_c and R_c are very small their effect can be neglected and thus the characteristic impedance becomes:

$$Z_0 \approx \sqrt{\frac{L}{C}} \tag{3.5}$$

If the cables are connected to an RF amplifier with an output impedance equal to their characteristic impedance at an end and to a load with the same impedance at the other end, do not experience power reflections. Since all commercially available RF amplifiers are standardized on a 50 or 75 Ω output impedance, the same applies for the vast majority of commercial coaxial cables.

Model	Characteristic impedance [Ω]	Inner core diameter [mm]	Jacket diameter [mm]	Attenuation @ 28 MHz [dB/m]	Specific capacitance [pF/m]	Specific inductance [μH/m]
RG-58	50	0.9	5	0.079	101	0.253
RG213	50	2.3	10	0.035	101	0.253

TABLE 3.1: Main features of the coaxial cables employed at CISAS. The RG-58 cables are used for signal transmission, while the bigger RG-213 carries RF power.

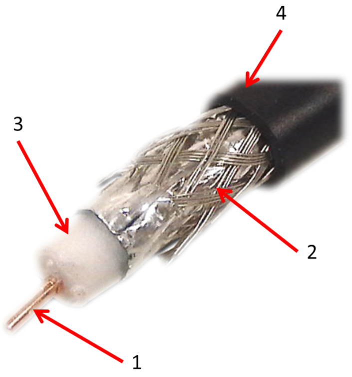

FIGURE 3.5: Example of coaxial cable. 1: inner conductor. 2: outer conductive jacket. 3: inner insulator (usually PTFE or PE). 4: outer insulator (usually PVC).

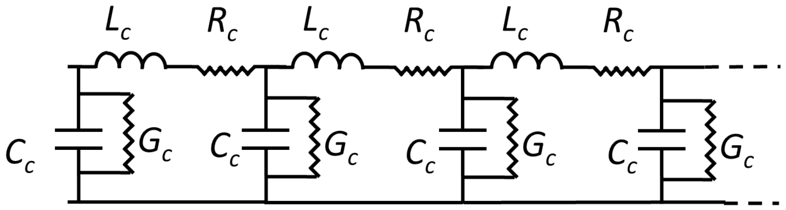

FIGURE 3.6: Coaxial cable equivalent electrical model, composed by an infinite series of elementary elements.

The cable model was verified according to the same procedure adopted for the antenna, adpoting a 2m long RG-58 cable. The results are reported in Figure[3.8] and Figure[3.9].

3.1.4 Matching box modell

The matching box available at CISAS for impedance matching is a custom-built capacitive device, employing two high vacuum variable capacitors (0 - 1250 pF each) connected as in Figure[3.10]. The device is modeled according to such scheme.

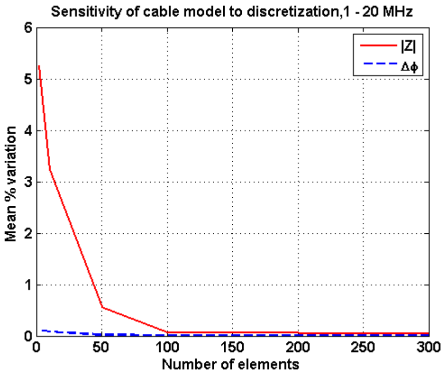

FIGURE 3.7: Sensitivity analysis carried out for a 2m long rg-58 cable up to 20 MHz.

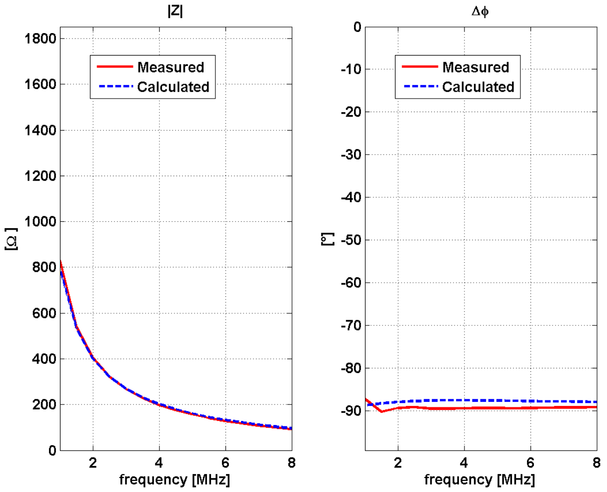

FIGURE 3.8: Coaxial cable model verification: frequency domain characterization of a 2 m long RG-58 coaxial cable.

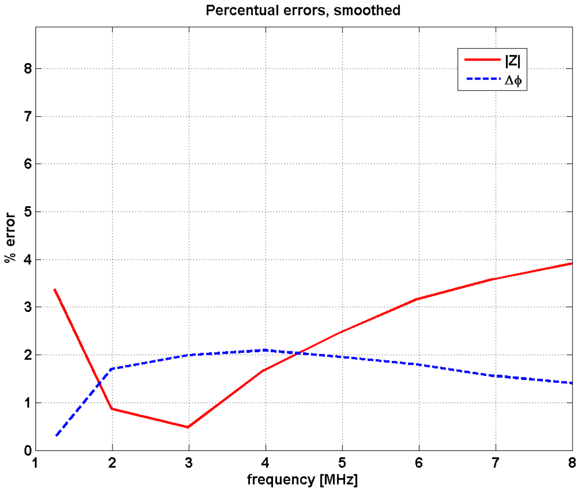

FIGURE 3.9: Coaxial cable model verification: relative error between simulated and measured data, smoothed over a 500 kHz interval.

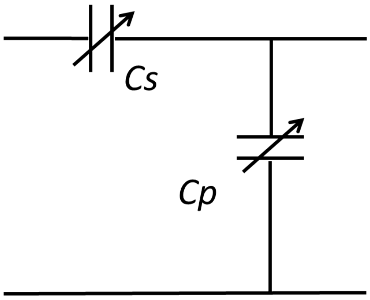

FIGURE 3.10: Matching box model.

3.2 Implementation

The lumped parameters model was implemented in Simulink®, MathWork's well known block diagram environment for multi-domain simulation. The models described in the previous paragraphs were directly assembled by putting together elementary resistors, inductors and capacitors, according to the illustrated schemes.
In general two Simulink libraries are employed:

- the SimPowerSystem library, which provides a toolbox of components specifically designed for the simulation of electrical system. This library is mainly employed for the frequency-domain analysis of the models, which allows to tune their electrical parameters in order to reproduce the same behavior observed by means of a network analyzer on the real components.
- the SimScape library, mainly devoted to the simulation of any kind of physical system, which for this application is favored for time-domain simulations since it allows to reproduce the physical structure of the RF system, resulting in a more accurate analysis of power fluxes and potentially allows multi-physics simulations. In Figure[3.11] the same antenna model is shown connected to a voltage generator, reproducing the operating voltage and frequency to which the real antenna was subject. Numerous voltage and current probes are placed within the circuit, in order to monitor power dissipation.

When performing time-domain analyses Simulink basically proceeds as follows:

- block diagram model compilation;
- memory allocation and block execution priority establishment;
- simulation loop. This step is composed by the iteration of two sub-steps, (i) model output calculation and (ii) model states update.

The simulation loop is substantially performed by propagating in time a set of differential equations by means of an integration algorithm, starting from the specified initial conditions.The preferred solution algorithm for time-domain simulations is Matlab's Ode15s, which is particularly indicated if the system has a stiff solution matrix, as it frequently is the case with this application. An adaptive time step is employed, in order to minimize computational time. The relative error tolerance, which determines the stopping condition of the solutor at every time step, is determined with a sensitivity analysis, in which it is progressively reduced until no change in the output is observed; its value typically ranges between 10^{-4} and 10_{-6}, depending on the simulation, thus in general a value of 10^{-6} is preliminarily adopted if not otherwise required.

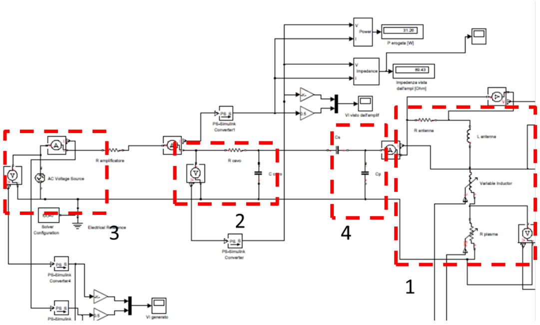

FIGURE 3.11: Simulink implementation of the lumped-parameters model, featuring the RF amplifier (3), the connection cable (2), the matching box (4) and the antenna (1).

As a final note, it is important to underline that, unlike inductances and capacitances, which are substantially unrelated to frequency, parasitic resistances are not constant and depend from the operating frequency due to skin effect and proximity effect. The lumped-parameters model operates under the hypothesis of fixed electrical parameters and thus cannot consider these effects, but this is not a limitation, since:

- usually parasitic resistances are very small with respect to the reactances involved in the circuit and their variation in the range of freqency of interest has a negligible impact on frequency-domain analyses;
- in time-domain analyses the model simulates an antenna at a given temperature and operating frequency, thus it is enough to calibrate the value of the parasitic resistances for the selected test case. Different test runs at different temperature or frequency can be emplyed for a temperature or frequency sensitivity analysis;
- the combined influence of skin and proximity effects expresses itself as parasitic power dissipation which scan be effectively condensated in an overall equivalent

resistance, whose value must be calibrated for the given operating frequency and temperature.

3.3 Performance prediction

As stated in 3.1 the lumped-parameters model needs to be tuned to the characteristics of an existing antenna, thus being an *analysis* tool rather than a *design* tool. On the other hand a simple estimation of the electrical parameters of an antenna by means of simple calculations is difficult, due to the presence of distributed effects such as parasitic resistances or capacitances, often requiring a long prototyping phase; in order to overcome this issue an antenna preliminary design approach was developed, aiming at the estimation of the electrical parameters of a new antenna from its geometry and design, in order to provide the input required by the lumped-parameters model.
Such approach is based on the employment of the free ware FEM software FEMM [22] (see A), which enables both electrostatic and magneto-static simulations on an antenna FEM model and allows a preliminary estimation of the electrical characteristics of a new antenna, easing the design and manufacturing of a prototype starting from which an optimization process can take place.

3.3.1 Finite elements simulation

The antenna is simulated in FEMM according to its real geometry and materials; the software can treat only planar or axisymmetric designs, but this is not a limitation for the purposes of this work since usually the antennas employed in the HPT are axisymmetric.
For the purposes of the simulations the antenna is seen as a combination of capacitances, both discrete and distributed, inductances, usually multi-winding coils, and resistances, connected according to its particular electrical scheme. Discrete elements are known and present no particular issues, while distributed parameters are thus estimated:

- the parasitic capacitances are preliminarily calculated with the help of electrostatic FEMM simulations: the antenna winding is approximated by one or more cylindric conductors, arranged according to the real set-up. Each conductor is given an uniform equivalent voltage $V_{eq} = (V_{max,c} - V_{min,c})/2$, where $V_{max,c}$ and $V_{min,c}$ are the voltage at coil input and output respectively. The windings are spaced according to their real disposition inside the antenna, with an additional spacing $ds = \phi_w$ between two consecutive windings which takes into account the

Elelement	Geometry	Material
Support tube	ϕ_{in}=29 mm, ϕ_{out} = 34 mm, l=80 mm	Quartz
Winding	ϕ_{mean}=30 mm, l=45 mm, ϕ_w=1.6 mm, N=56 loops (2 x 28)	Copper

TABLE 3.2: Key features of the simulated antenna.

round surface of the wires. The total parasitic capacitance of the winding is then calculated as $C_{coil} = Q_{low}/(\Delta V)$, where Q_{tot} is the absolute value of the total accumulated charge and ΔV is the total voltage drop experienced by the winding. Q_{tot} is calculated by summing either all negative or all positive charge accumulations on the various conductors, since the absolute value of the resulting sum must be the same in both cases. This formulation was chosen since the capacitance is modeled as in parallel to the winding and thus is subject to the same voltage drop; The absolute value of the voltages employed in the simulation is not critical, since the accumulated charge will vary according to the capacitance, which remains constant. What is important is that the voltage *ratios* between the various elements are respected, since this reproduces the actual voltage drop across the coils.

- the antenna is modeled in an axysimmetric magnetic FEMM simulation simulation as a simple coil with one or more layers, according to the chosen geometry. The diameter is constrained by antenna geometry, while the number of windings is an optimization parameter and is at first guessed according to experience. FEMM is capable of directly estimating the inductance and the parasitic resistance of the winding at the desired frequency, due to both skin and proximity effect.

After this process the distributed and discrete parameters, combined according to the electrical scheme of the antenna, can be employed to preliminarily estimate its frequency-domain impedance trend. The output of this design tool, as it will become clear in 3.3.2, cannot be directly employed for a detailed design of a new antenna, but is capable of providing a reliable estimation of its electrical characteristics, useful for RF system preliminary design and for antenna prototype development.

3.3.2 Finite elements model validation

The preliminary antenna design tool was validated against experimental data employing the same antenna used for the verification and validation of the lumped-parameters model, characterized by a resonance at 4.84 MHz and an impedance peak of about 2400 kΩ. The geometry and materials of the antenna were modeled in two electrostatic and magnetic FEMM simulation files, according to the data reported in Table[3.2]:

With these data the script was able to estimate the electrical parameters of the antenna, reconstructing its impedance vs frequency curve as shown in Figure[3.12], where it is compared to the experimentally measured one: the matching between experimental and numerical data shows a certain degree of error, probably due to imprecisions in the FEMM models, but the key features of the antenna, namely its resonant frequency and impedance peak at resonance, 4.838 MHz and 2.605 kΩ respectively, are predicted with a fairly good error margin, below to 1% and 10% respectively.

In all, it can be concluded that the preliminary design approach here presented has confirmed its validity, providing useful estimations on antenna performance which can be used to preliminarily size the RF network and to significantly reduce antenna prototyping time and resources.

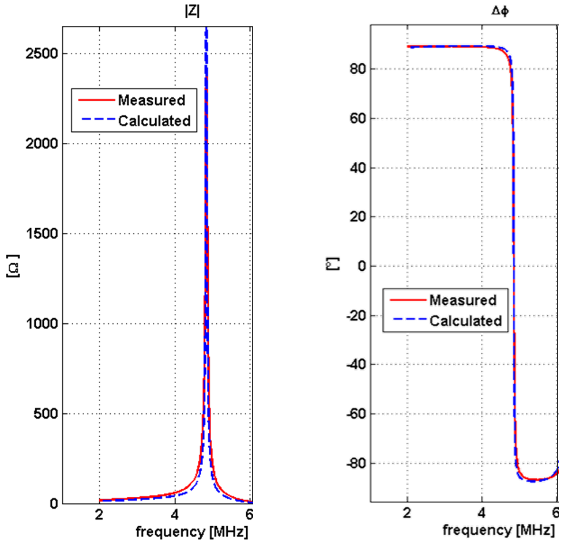

FIGURE 3.12: Frequency domain characterization of the antenna with electrical parameters estimated by FEMM, compared against experimental values .

Chapter 4

Experiment Upgrade and Low-Power Optimization

As a preliminary step before the design and development of an high power HPT test-bed it was decided to preliminarily perform a further optimization near the input power level and mass flow rate of HPH.Com ($\approx$ 50 W, $\approx$ 0.1 mg/s), employing the existing experimental set-up. The chosen gas was Argon, the same used in project HPH.Com, due to the operating experiency accumulated with this gas.

The optimization involved two main aspects: as a first step, the design of the RF network of the thruster was upgraded with additional electrodes and geometrical modifications, aiming at the maximization of the electric field; after this phase the thruster employing the upgraded network was subject to a geometrical optimization. The results allowed to identify the solutions over which to base the design of an high power HPT. The activity was carried out employing the vacuum HPT model available at CISAS laboratory (see 2.2.2), since (i) it is closer to the configuration of a real thruster with respect to the external set-up (2.2.1) and (ii) it allows testing in conditions which are more representative of the real operating environment. The optimization was carried out acting on several geometrical and electrical parameters of the thruster, achieving a net performance increase whose entity will be quantified in 4.5.

4.1 Experimental set-up

The experiments employed the existing high vacuum facility (see 2.1) and thruster laboratory model (see 2.2.2) used during HPH.Com. The adopted set-up is shown in Figure[4.2]: the thruster laboratory model was mounted inside the vacuum chamber and positioned in order to be directly observable and accessible by means of a lateral

DN300 observation/maintenance port. The thruster was fed with RF power by the externally-placed HFPA-300 RF amplifier through N type electric feed-throughs. A V/I measurement unit was placed inside the vacuum chamber, in order to reduce as much as possible the length of the cable connecting it to the thruster, and employed to monitor the impedance and input power of the antenna during operation. Two PT-3850 thermo-resistances were applied to the thruster in order to monitor its temperature; in particular one, denominated T1, was attached to the antenna, while the other, indicated with T2, was placed on the conical baffle, which forms a single part with the discharge chamber. The thruster was fed with Argon, whose mass flow rate was set by means of the MKS flow controller.

The choice of employing the in-vacuum model means that not all the plasma diagnostics available at the propulsion laboratory could be employed, in particular:

- the microwave interferometer (2.3.1) cannot be used for measurements inside the vacuum chamber, due to size and mounting constraints;
- optical spectrometers (2.3.2) cannot always be employed since the vacuum model, being close to a real thruster, has a very compact design, meaning that the plasma inside the discharge chamber is often masked by the antenna and the magnets and cannot be observed;

In addition to this the RPA ([3]) suffered damage to the grids due to electric breakdown and could not be repaired in time to take part in the measurements. For these reasons the only viable plasma diagnostic was the Faraday probe (2.3.3). The probe was placed on a 2 axis movement system for axial and radial scans of the ejected plasma plume (radial excursion: 200 mm, axial excursion: 300 mm). The distance d_{pt} between the thruster and the probe during radial scans was usually set at 20 mm, in order to be sure to include borders of the plume. In all tests the probe was biased at -150 V, in order to be sure that the detected ion current lies well within the saturation range.

4.2 Operating procedure

Each test was performed according to the following procedure was:

- thruster activation with $\dot{m}$ 0.2-0.4 mg/s at 50 - 100 W. These conditions always ensured plasma ignition;
- adjustment of RF amplifier output at $\approx$ 50 W;

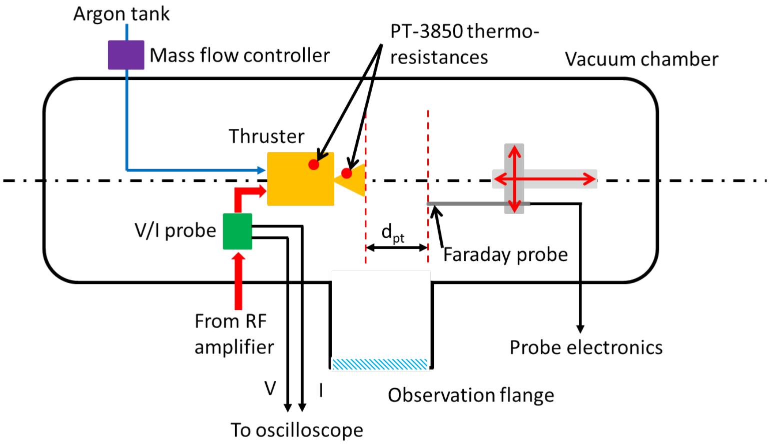

FIGURE 4.1: Experimental set-up employed during the low power optimization tests. The vacuum facility and the thruster laboratory model are those described in 2.

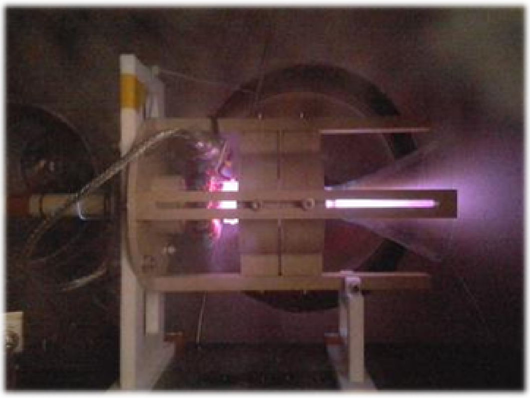

FIGURE 4.2: Experimental activity: the thruster firing.

- progressive decrease of $\dot{m}$ in order to find its minimum value capable of sustaining the plasma;
- frequency adjustment in order to maximize the power transfer between the RF amplifier and the antenna;
- current measurements.

It was not always possible to completely eliminate the imaginary part of antenna impedance via frequency adjustment, due to the strong effect of the plasma; this generated power reflections which reduced the effective power coupled to the antenna below 50 W, in spite of an amplifier output set to that value. This effect could not always be appreciated in real time and was often observed after the elaboration of oscilloscope plots.

During operation the waste heat generated by the plasma source and the ohmic dissipations in conductors progressively increased the temperature of the thruster, leading to a temporal drift of the ejected current; for this reason temperature was monitored by means of the two thermo-resistances placed on the antenna and on the plasma source and tests were performed with brief (1-2 min) firings followed by a relatively long cooling time, in order to ensure that all tests were performed in the same temperature ranges, approximately 40-45 °C.

4.3 Performance parameters

During the thest the performance of the thruster was quantified by means of the following two parameters, both accessible through Faraday probe measurements as explained in 2.3.3 and A:

- the total current ejected from the thruster as a function of the input power, I_{tot}/P;
- the plasma plume divergence demi-angle α_p

An higher total current per input watt implies an higher ionization fraction, which in turn leads to an higher specific impulse, since there are more ions in the plume, which are much more energetic than neutral atoms; a smaller α_p, on the other hand, indicates a smaller plume divergence and thus a more efficient propulsive use of the ejected mass flow rate. The two effects together lead to an increase in thrust, since $T = \dot{(m)} g_0 I_{sp} \cos\alpha_p$. The choice of the ratio I_{tot}/P is justified by the fact that, as already explained, the power level could not be kept constant among all the tests, thus introducing the need of a more general parameter to compare the performance of each thruster configuration. The uncertainty estimation for α_p is illustrated in 2.3.3, while for I_{tot}/P the uncertainty was calculated as $\epsilon = \sqrt{(\epsilon_I/P)^2 + (I_{tot} \cdot \epsilon_P/P^2)^2}$, with ϵ_I and ϵ_P the absolute uncertainties related to current and power respectively.

4.4 RF thruster design optimization

During the tests the thruster laboratory model featured the RF network employed during HPH.Com, based on a 75 mm long inductive-capacitive antenna built on an 80 mm long quartz support tube, developed for low-power operation and usually fed with a 60-80 V input voltage. This design was optimized aiming at the maximization of the electric field in the plasma source while keeping the operating voltages constant. This was achieved by means of two simple yet effective solutions:

- reduction of antenna length l_a (potential increase of the axial electric field E_z);
- additional electrodes (potential increase of both components of E).

4.4.1 Antenna length

The effect of antenna length variation was explored by testing two different antenna lengths, 75 mm and 55 mm, on the same thruster configuration. The first value nears the maximum of 80 mm allowed by the quartz support, while the other is the minimum practically achievable without changing antenna components. The length of the antenna is known within ± 1 mm.

The results are reported in Figure[4.3]: the plume divergence demi-angle appears to be practically unaffected by the variation of l_a, while I_{tot}/P experiences a very limited ($\approx$ 10%) increase for an antenna length decrease of $\approx$ 33%. These results substantially indicate that l_a has a relatively small impact on thruster performance, although smaller values seemingly produce an improvement of thruster performance. For this reason it was decided to adopt a 55 mm long antenna for the second part of the optimization process.

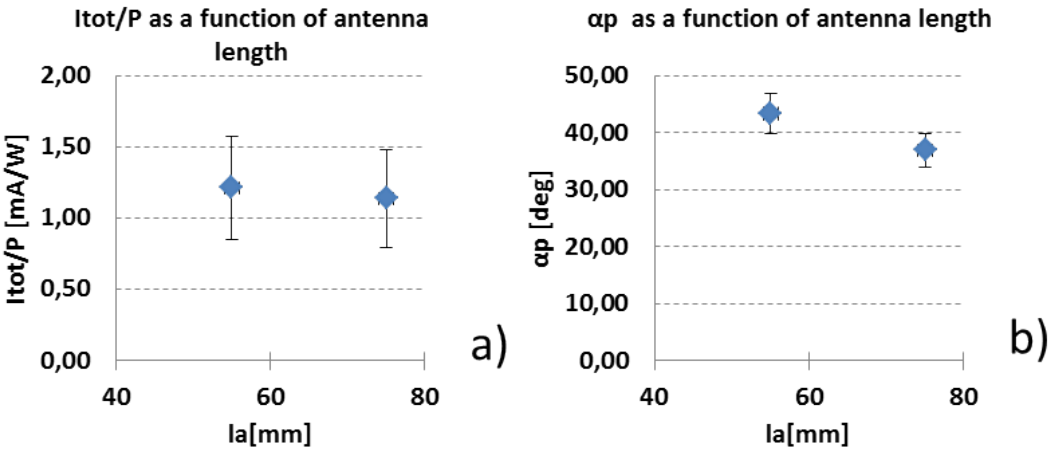

FIGURE 4.3: Effect of different antenna lengths on thruster performance.

4.4.2 Additional electrodes

The possibility of inserting additional electrodes was at first studied by means of electrostatic FEMM simulations, in order to estimate the increase in the electric field produced by their presence. The aim is to elevate the overall electric field in the discharge chamber, without increasing the voltage applied to the antenna and without over-complicating the antenna structure; the simplest way of achieving this was found in the application of

	No electrode	Grounded electrode
P [W]	52,5 ± 4.2	54,1 ± 4.3
$\dot{m}$ [kg/s]	$1.25 \cdot 10^{-7} \pm 4.2 \cdot 10^{-10}$	$1 \cdot 10^{-7} \pm 4.2 \cdot 10^{-10}$
I_{tot}/P [mA/W]	0.9 ± 0.32	0.86 ± 0.3
α_p [°]	43 ± 3.44	35 ± 2.8

Table 4.1: Analysis of the effect of the grounded electrode on thruster performance. The tests were performed on the same HPT configuration.

a grounded metal ring facing the outlet side of the antenna. The application of the grounded electrode forces a steep voltage drop across the outlet region, effectively increasing the electrical field without requiring an higher antenna voltage or the insertion of ever more complex solutions such as transformer stages, whose implementation resulted troublesome due to size and electric interference issues and was abandoned early in the initial phases of the work. Figure[4.4] shows the results of the FEMM simulations, evidencing the net increase of the electric field modulus in the outlet zone, which should lead to better plasma ionization and acceleration.

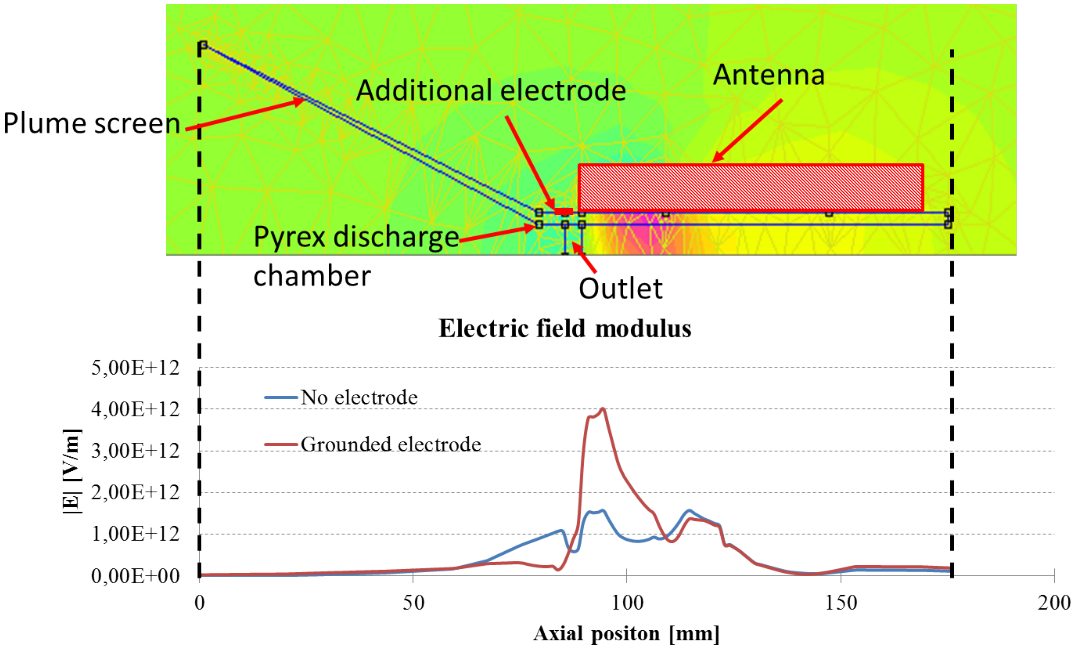

Figure 4.4: Electrostatic antenna simulations exploring the effect of an additional grounded electrode.

The effectiveness of the grounded electrode was tested on the same HPT configuration, finding out that it had a strong impact on thruster efficiency, since it allowed the thruster to achieve the same I_{tot}/P with a sensibly lower mass flow rate while reducing α_p, as illustrated in Table[4.1]. For this reason it was decided to permanently incorporate this upgrade in the final antenna configuration.

4.5 Thruster geometry optimization

As already stated, after the upgrade of the antenna the thruster was subject to a geometrical optimization activity, which involved several parameters:

- the diameter of the outlet section, ϕ_o;
- the length of the discharge chamber, l_s;
- the position of the magnets, Δx_{m-o};
- the position of the antenna, Δx_{a-o};
- the magnets - antenna relative positioning, $\Delta x_{m-a} = \Delta x_{m-o} - \Delta x_{a-o}$;

These parameters are indicated in Figure[4.5], which shows a scheme of the geometry of the HPT laboratory model; the positions of the antenna and magnets are expressed according to the reference system composed of the r and z axes, centered on thruster axis in correspondence of the inner face of the outlet section, chosen for practical reasons. The adjustment of thruster geometry is expected to have a sensible impact on thuster performance, in particular:

- the diameter of the outlet section and the length of the discharge chamber should affect the neutral gas pressure profile inside the plasma source, with a direct influence on ionization efficiency;
- the positioning of antenna and magnets should influence the relative alignment of the AC electric and DC magnetic field inside the plasma source, with effects on ionization efficiency and plasma confinement. The position of the magnets is also expected to influence the behavior of the "magnetic nozzle" into which plasma expands, in particular under the point of view of plume divergence.

Table[4.2] reports the tested configurations and the related operating conditions. All geometric parameters are known within ± 1 mm, except for the outlet diameter which is known within ± 0.1 mm. The uncertainty associated with power is $\pm 8\%$ (see 2.1.2), while that associated to the mass flow rate is $\approx 4.2 \cdot 10^{-10}$ kg/s and can thus be neglected.

In order to explore all the possible combinations of the five considered geometric parameters it would have been necessary to perform an excessively high number of tests, even considering only three values for each parameter (3^5 experimental points); for this

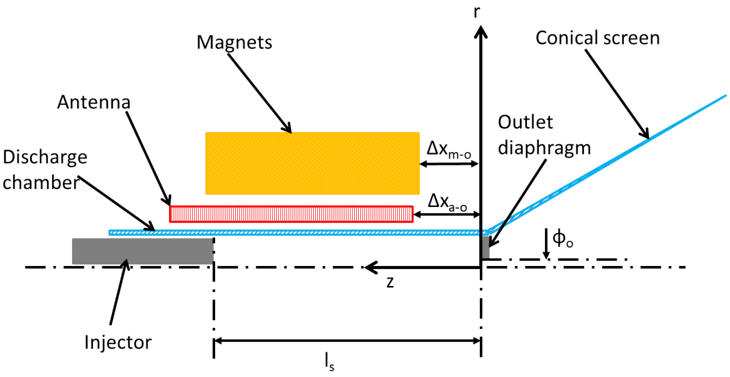

FIGURE 4.5: Geometrical parameters of the laboratory model.

Geometry						**Operating conditions**	
Source length ls [mm]	**Source inner diameter φs [mm]**	**Outlet section diameter φo [mm]**	**Magnets - outlet relative position Δx m-o [mm]**	**Antenna-outlet relative position Δx a-o [mm]**	**Antenna-magnets relative position Δx a-m [mm]**	**Mass flow rate $\dot{m}$ [kg/s]**	**Input power P [W]**
65	19	5	0	-2	2	1,00E-07	55,6
65	19	5	0	-2	2	1,00E-07	55,6
65	19	5	0	-5	5	1,67E-07	48,5
65	19	5	0	-9	9	1,67E-07	52
65	19	5	-5	-13	8	1,67E-07	50,2
65	19	5	6	2	4	1,42E-07	55
65	19	5	0	5	-5	1,25E-07	52,50
65	19	5	0	10	-10	1,25E-07	53,30
95	19	5	0	10	-10	1,25E-07	52,50
95	19	5	0	15	-15	1,25E-07	57,40
95	19	5	5	13	-8	1,25E-07	51
95	19	5	0	4	-4	1,00E-07	54,1
65	19	5	0	4	-4	1,00E-07	52,4
80	19	5	-24	0	-24	1,25E-07	39,5
80	19	4	-24	0	-24	1,25E-07	48,8
80	19	4	-24	0	-24	1,50E-07	54,2
80	19	3	-24	0	-24	1,25E-07	28,08
80	19	4	-16	0	-16	1,17E-07	51,24

TABLE 4.2: Test matrix for the geometrical optimization phase. All geometric parameters are known within ± 1 mm, except for the outlet diameter which is known within ± 0.1 mm. The uncertainty associated with power is ±8%, while that associated to the mass flow rate is $\approx 4.2 \cdot 10^{-10}$ kg/s and can thus be neglected.

reason it was decided to perform only a fraction of the required tests, covering the variation of all involved parameters without necessarily including all possible combinations. The results are reported in Figure[4.6] and Figure[4.7]; with reference to these plots the following conclusions can be drawn:

- the combined analysis of Figures [4.6a), b), d)] and [4.7a), b), d)] reveals that the positioning of the magnets with respect to the outlet section, Δx_{m-o}, has a sensible impact on thruster performance, since it leads to a sensible increase in the ion current per input watt, while its effect on the plume divergence angle is much more limited. No net dependence of the performance parameters on Δx_{a-o} emerges on both performance parameters;

- the length of the discharge chamber, l_s (Figures [4.6c)] and [4.7c)]), has a negligible impact on thruster performance in the explored dimensional range, since the apparent peak performance at l_s= 80 mm is due to the more efficient magnets position;
- the outlet diameter, as the magnets position, plays a key role in the definition of thruster performance, as is clear from Figures [4.6e)] and [4.7e)]. In particular a smaller outlet diameter increases the performance under the point of view of both the current and the divergence angle, probably thanks to a more efficient pressure profile inside the discharge chamber and to a better geometrical focalization effect.

Table[4.3] reports the comparison between the final result of the optimizaton process and the initial thruster configuration: thanks to the geometric optimization carried out within this analysis it was possible to cut to half the divergence angle of the plume and to increase the output ion current per unit watt of ≈ 3.5 times.

The electrical and geometrical optimization process carried out during this phase of the work led (i) to the development of simple yet effective upgrades for the existing thruster RF network and (ii) to the identification of optimization solutions to be employed in the high power HPT.

Parameter	Optimized	Initial
ϕ_o [mm]	3 ±1	5±1
l_s [mm]	80 ±1	65±1
Δx_{m_o} [mm]	-24±1	0±1
Δx_{a-o} [mm]	0±1	-5±1
I_{tot}/P [mA/W]	2.81 ±1	0.78±0.28
α_p [°]	36.13 ±1.4	18±2.9

TABLE 4.3: Optimized and initial geometrical configurations of the low power HPT.

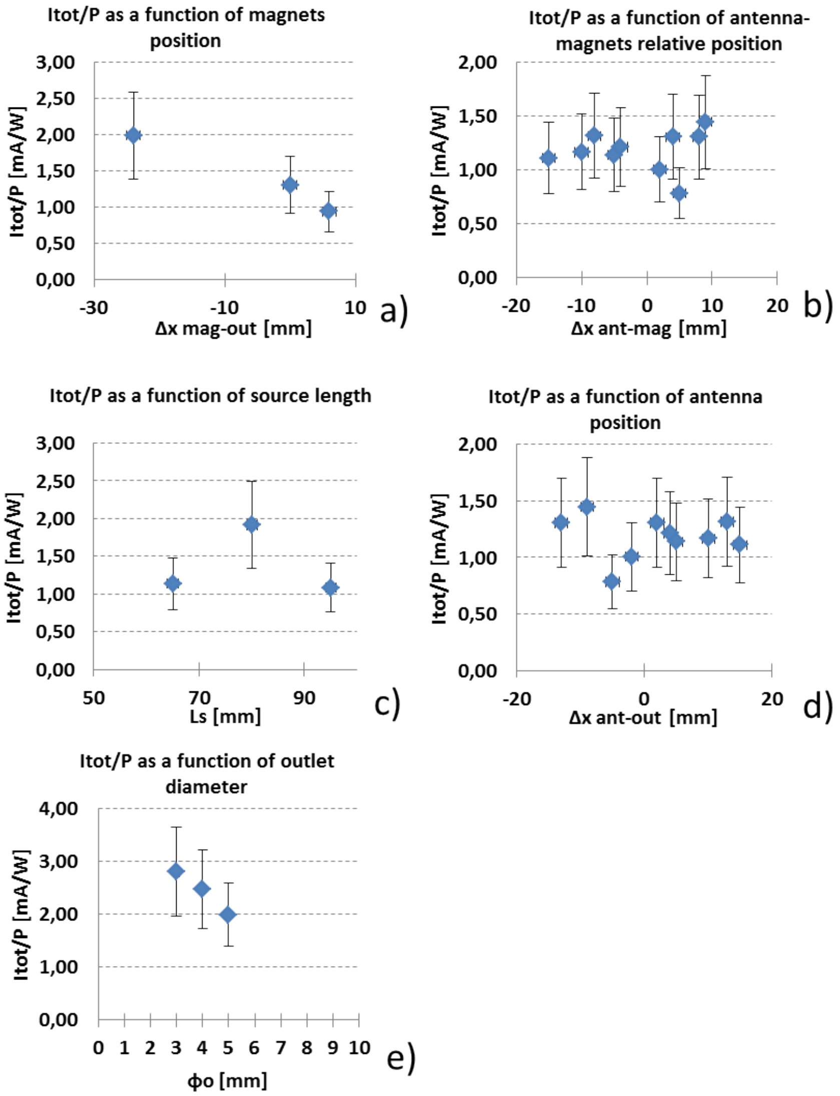

FIGURE 4.6: I_{tot}/P as a function of thruster geometry. The positioning of the magnets and the diameter of the outlet section appear to have the most sensible impact on the total ejected ion current per input watt.

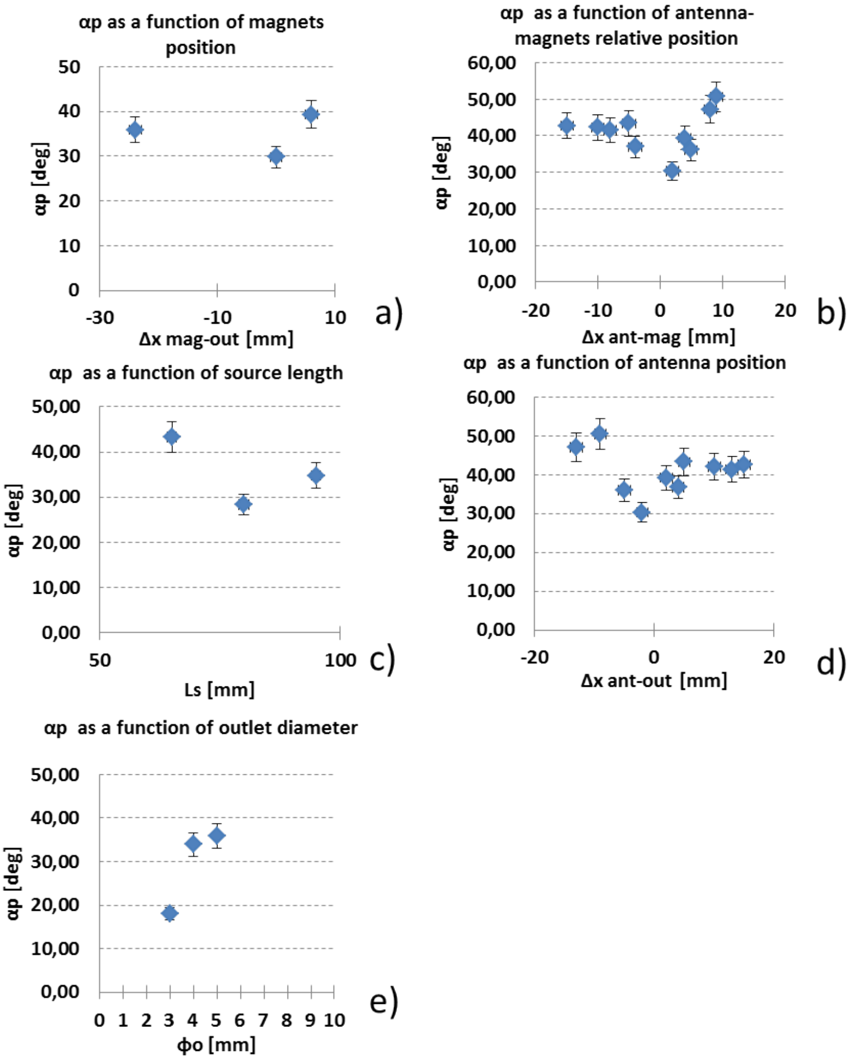

FIGURE 4.7: α_p as a function of thruster geometry. The positioning of the magnets and the diameter of the outlet section appear to have the most sensible impact on the effective plume divergence half-angle.

Chapter 5

Test-Bed Development for High power testing With Different Propellants

This chapter illustrates the development of an high power HPT test-bed for multi-propellant operation, which, along with the RF system destined to power it, constitutes a part of the high power experiment developed during this work. The activity was carried out following a series of progressive steps, each covering a key issue of such application:

- identification of the main system requirements;
- preliminary low-power characterization with propellants different from Argon;
- preliminary testing at the target power density with the existing test-bed and subsequent analysis of:
  - issues related to the plasma source;
  - issues related to accessory sistems and components, such as cables, V/I probes and vacuum pumps;
- design and development of the high power test-bed;

The reconfigurable, externally mounted experiment developed for HPH.Com (2.2.1)was chosen as the base from which to develop the new test-bed, since (i) it allows to employ the whole array of available plasma diagnostics, (ii) it is highly accessible even during operation, thus reducing the complexity of re-configuration operations, (iii) it allows an easier waste heat dissipation with respect to an in-vacuum model and (iv) it allows to re-employ already existing components, thus reducing costs.

5.1 Target HPT configuration

The design of the high power test bed was carried out as a function of the research projects ongoing at CISAS on the subject of high power HPTs, such as project S.T.R.O.N.G. [1], aiming at the development of an 1-1.5 kW HPT prototype operating on Argon or CO_2, with a target thrust in the range of 75-100 mN and a specific impulse near 2000 s, enabling a wide array of potential applications.
Argon is currently seen as a good candidtate propellant for electric thrusters, thanks to its relatively low cost and high availability with respect to other traditional propellants, such as Xenon or Kripton.
CO_2, on the other hand, may enable a wide array of potential mission scenarios involving the International Space Station (ISS) as a refueling base for non-expendable spacecraft: the ISS has regenerative systems capable of recycling a wide range of by-products of the human presence and activity [23], but requires some residual gases to be vented in space: in particular the 6-elements human crew produces relevant quantities of CO_2 (about 1 kg/day per person), reaching about 6 kg/day of storable gas which can represent a reliable source of propellant for an electric propulsion subsystem able to utilize it. Testing CO_2 on the HPT will also provide an occasion to investigate the behavior of molecular gases in the Helicon plasma source, potentially opening the way to additional industrial or medical applications.

The requirements on thrust, specific impulse and propellant type reported in 5.1 were employed as constraints in an optmization algorithm involving a plasma source global model, developed at CISAS within another PhD work [24]. The results, reported in Table[5.1], provided the estimated configuration of the thruster for the target performance level, over which to base the design of the HPT test-bed.
As it can be seen from Table[5.1] the HPT configurations for Argon and carbon dioxide are very similar under all points of view, with the sole notable difference of the outlet section diameter, and operate in the same range of power and mass flow rate. Thanks to these results it is possible to limit the complexity of the test-bed:

- the length and inner diameter of the discharge chamber are very similar, indicating that the same dielectric tube can be employed for both gases;
- the required magnetic field is the same, thus the same magnetic system can be employed;
- the mass flow rate levels lie in the same range and can be provided by a single mass flow controller;

Under these points of view the high power test-bed can be developed according to the same philosphy adopted for the low power experiment (2.2.1, 2.2.2), featuring a single discharge chamber with a fixed diameter, in order to simplify the design, but nonetheless allowing the characterization and optimization process acting on the following parameters:

- plasma source length;
- outlet section diameter;
- magnetic field intensity;
- magnetic field position;

The final target of the test-bed is to (i) characterize the effect of each parameter on thruster performance, providing also data for the validation of the numerical predictions and (ii) optimize the parameters, starting from the results of global model simulations, in order to minimize the input power and mass flow rate required to reach the desired performance. In order to do so the test-bed must allow the independent variation of these parameters around the numerically estimated values in the greatest possible range, without over-complicating the design.

Gas	l [mm]	ϕ_{in} [mm]	ϕ_{out} [mm]	$\dot{m}$ [kg/s]	B [G]	P [W]	T [mN]	I_{sp} [s]	n_e [m^{-3}]
Ar	109	38.8	16	$4.4{\cdot}10^{-6}$	1500	1456	96.5	2110	$1.2{\cdot}10^{20}$
CO_2	109	49	42	$3.04{\cdot}10^{-6}$	1500	1496	94	2139	$2{\cdot}10^{19}$

TABLE 5.1: Results of the global model simulation. l, $\phi_{in}$and ϕ_{out} are the length, inner diameter and outlet section diameter of the discharge chamber, $\dot{m}$ is the mass flow rate, B is the mean axial magnetic field at the lateral boundary of the chamber, P is the input power and n_e is the plasma density.

5.2 Plasma diagnostic systems

The majority of the plasma diagnostics already existing at CISAS resulted employable for high power operation with Argon and CO_2, although with some limitations:

- the microwave interferometer is independent from the type of propellant and the spacing between the waveguide horns conveying the microwave beam through the plasma is of about 50 mm, granting the possibility of operation with plasma source diameters of the order of those required for the high power HPT. The instrument, however, has an upper density limit of $7{\cdot}10^{19}$ m^{-3}, at which the 75 GHz signal of the interferometer experiences a cut-off [17]. This indicates that the device is employable "as is" with both Argon and carbon dioxide at high power, but may not be ableto measure the highest density peaks produced during operation, although its density limit is quite close to the maximum expected value;

- the Faraday probe is also independent from the type of propellant and does not present issues related to the higher power level, provided that the distance from the thruster exhaust is great enough to avoid thermal damage and excessive erosion. For these reasons also this diagnostic was judged employable "as is" in the new set-up;

- the optical spectrometers, although unaffected by the operating power, can observe only a specific, pre-determined wavelength range and thus may not be suitable for operation with propellants whose significant emission lines fall outside such range. The combined wavelength coverage of the exisiting spectrometers lies in the 200-1100 nm range, fortunately including both Argon [19] and CO_2 [25] emission lines which can be used for spectrometric estimations;

- the bandpass optical filters employed by the CCD cameras for the estimation of the actual plasma column diameter are specific for Argon, but also in this case they can be employed also for CO_2 to some degree, as it will be shown in 5.3.

These diagnostics together are capable of providing some significant insight on thruster and plasma source performance, in particular about the ionization level, plasma density and electron temperature, but lack a mean of measuring the actual ion energy distribution function (IEDF), which is mandatory for the estimation of the specific impulse and thus of thrust. Unfortunately the existing RPA, developed for project HPH.COM ([3]), devoted to this task, required a partial re-design in order to be employable in the new set-up, due to the higher expected density levesl, which may lead to excessive pressure within the device and electric arcing between its grids; such activity could not be carried out in time within this work, however, if a matching between the other experimentally accessible quantities and their numerical estimations is achieved, the numerical estimation of specific impulse can then be considered reliable.
In addition to the experimental activity at CISAS it is planned to test the HPT in-vacuum model in the facilities of other partners of the project, equipped with thrust measurement systems whose output can complement the data provided by CISAS diagnostics and allow a complete estimation of the real thruster performance.

5.3 Low power investigation of new propellants

Since a great amount of data on low power operation with Argon was already collected during HPH.Com, providing a starting knowledge base, it was decided to carry out a preliminary low power survey on CO_2 in order to gain a first experimental experience on the behavior of the HPT with such propellant and provide data for the comparison with respect to operation with Argon.

5.3.1 The set-up

The tests were carried out employing the external experiment described in 2.2.1, according to the layout reported in Figure[5.1], reproducing one of the most performing configurations tested with Argon [3]: the plasma source featured a length l_s of 140 mm, an inner diameter of 19 mm and an outlet diameter ϕ_o=5 mm; the magnetic system was the one used during HPH.Com, based on permanent magnets (see 2.2.1), and was placed at a distance Δx_{m-o}=40mm from the outlet flange. The antenna, of the same inductive-capacitive type used for the low-power optimization tests (4), was positioned at a fixed distance Δx_{a-o}=75mm with respect to the outlet flange, due to geometrical constraints imposed by the presence of the plasma diagnostics. The employed diagnostics were:

- an Ocean Optics HR4000+ spectrometer, covering a wavelength range of 220-650 nm, employing a 2 m long, 600 μm core optical fiber;
- the microwave interferometer.

Both diagnostics were placed near the outlet region, centered on a point at Δx_{d-o}=27mm from the outlet flange.

The impedance matching and input power of the antenna was monitored by means of a single V/I module, directly connected to the antenna itself.

Figure[5.2] portays the set-up.

5.3.2 Experimental activity

The behavior of the plasma source was tested by performing a power and mass flow rate sweep, according to the test matrix reported in Table[5.2]: the lower mass flow rate value is the experimentally determined minimum one capable of sustaining a discharge within the tested power range, while the upper value corresponds to the maximum allowed by the mass flow controller. The input power range is the same explored during HPH.Com.

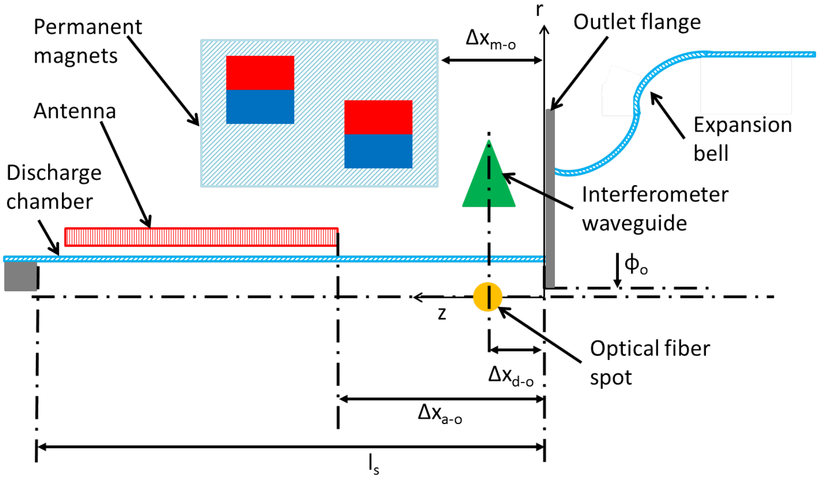

FIGURE 5.1: Scheme of the set-up for CO_2 testing.

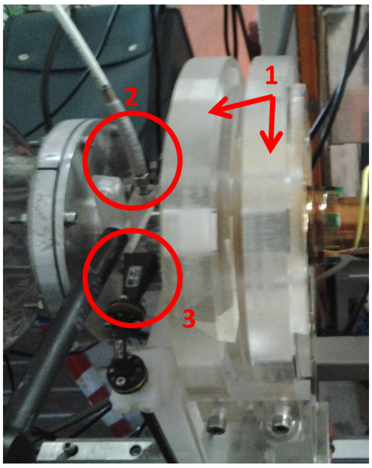

FIGURE 5.2: Picture of the set-up. The plexiglass casings for permanent magnets (1) are clearly visible in the middle left of the picture, while on the far left the optical fiber(2) and the interferometer waveguides (3) are evidenced.

The employment of the interferometer required the estimation of the actual plasma discharge diameter, as explained in 2.3.1; this was accomplished by means of a CCD camera equipped with a 488BP10 filter, centered on the 488±10 nm band, which includes a intense ionized Argon emission line at 488.0 nm. CO_2 is characterized by strong emission in this band as well, which is however related to both ions and excited neutrals; in spite of this the plasma diameter estimation was possible, adopting the following procedure:

- after the test matrix was completed an unfiltered reference image was taken with the plasma turned off, in order to estimate the scale of the pictures;

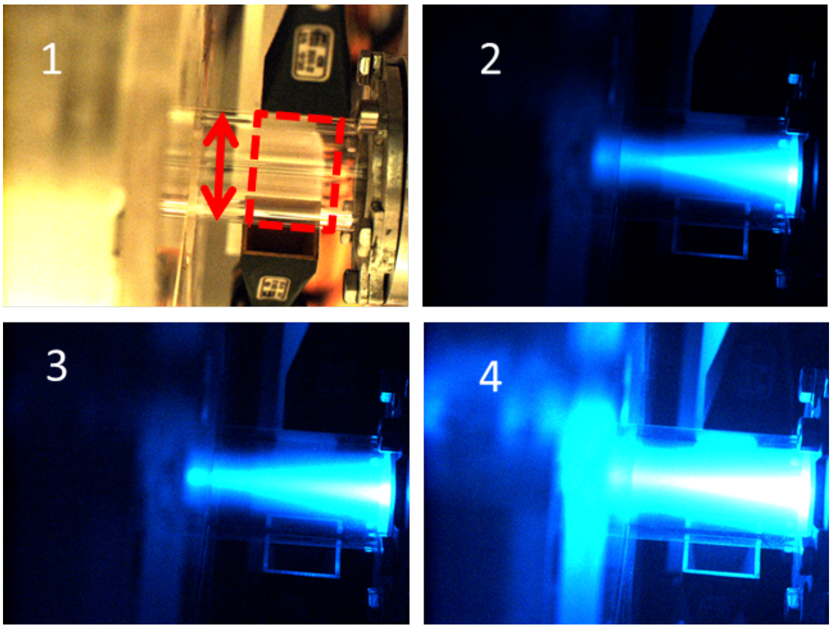

Figure 5.3: Estimation of effective plasma column diameter for interferometric measurements. 1: unfiltered reference image. 2: pure Ar discharge. 3: Ar-CO_2 mixture. 4: pure CO_2 discharge.

- the gas adduction line was cleansed of the remaining CO_2 and filled with Argon, which was employed to ignite a new plasma with a power level around 50 W. A first filtered frame was taken;
- with the plasma still on the CO_2 tank was connected to the adduction line in parallel with the Argon one, in order to achieve a 50% Ar, 50% CO_2 mixture. A second filtered frame was taken in this condition;
- finally the Argon tank was disconnected with the plasma source still in function, and, after all the Argon remanining within the gas line was depleted, a final filtered frame was taken with a pure CO_2 discharge.

In figure[5.3.2] Argon produces the aforementioned discharge structure, the blue emission is concentrated in the core; as the CO_2 percentage is raised, the outer zones of the volume are progressively filled with blue emissions, due to excited neutrals, however the strongest part of the emission is still concentrated in the core, indicating the region populated by the charged particles, figure[5.3.3] and figure[5.3.4]. Core diameters ranging between 5-7 mm were estimated in the zone covered by the interferometer waveguides, leading us to the choice of a mean value of 6 mm.

The resulting plasma densities are reported in Figure[5.4]: as it can be seen plasma density exhibits a maximum for a mass flow rate of $1.8 \cdot 10^{-7}$ kg/s, apparently indicating the existence of an optimal pressure profile inside the discharge chamber, a behavior already experienced with some plasma source configurations during operation with Argon. The electron temperature was estimated from the emission spectra by means of the plasma source global model, achieving values comprised between 2 and 2.4 eV.

From a qualitative point of view the behavior of the discharge was similar to what already observed with Argon, both in terms of visual observation of the plasma and impedance matching between the amplifier and the antenna. At the lowest tested mass flow rate, however, the discharge was not stable, probably due to the combination of the relatively high ionization energy of CO_2 and of an unfavorable neutral gas profile within the discharge chamber. For this reason it was not possible to perform a test at 120-130 W with low mass flow rate, due to an abrupt change in the plasma discharge regime, detected through the sudden change of antenna impedance, resulting in the experimental point 06, which was considered as spurious. Such effects were encountered also with Argon, but typically at lower mass flow rates.

An additional series of tests was attempted with a 15 mm outlet diameter, but the discharge was unstable and of very difficult ignition.

The same plasma source configuration employed in this series of tests has already been tested during HPH.COM in the same range of mass flow rate employing Argon [3] and an input power of 50 W; the results were employed as a benchmarck against which the performance with CO_2 was evaluated, as shown in Figure[5.5], which compares the trend of plasma density against mass flow rate for the two gases, for a constant input power of 50 W. For the sake of comparability the values of plasma density at 50 W for CO_2 were extrapolated from the plots of Figure[5.4], employing polynomial fits; the experimental point 06, which was judged spurious, was not considered, resulting in a linear interpolation between the remaining two points. From the plots of Figure[5.5] two key observations can be carried out:

- both gases exhibit a maximum in plasma density at a specific mass flow rate, which thus appears to be a feature related to the configuration of the plasma source and not to the type of propellant;
- Argon in general allows to obtain higher densities with respect to CO_2, a fact that is probably related to a lower ionization energy ($\approx$ 15eV vs eV).

The different quantitative performance of the two gases can be considered in agreement with global model predictions, which indicate that, in order to achieve optimal operation, different geometric configurations of the HPT and mass flow rate levels must be adopted; this appears to be supported by the the similar qualitative performance, which indicates that a geometric optimization of the thruster, similar to the one carried out in 4 on the Argon-fed low power HPT model, is possible also for CO_2.

Further experimental investigation involving characterization and optimization tests with CO_2 is foreseen in the next future at CISAS, whithin the frame of the existing research programs.

Test	$\dot{m}$ [kg/s]	f [MHz]	P [W]
01	$2.5 \cdot 10^{-7}$	1.4	36.2
02	$2.5 \cdot 10^{-7}$	10.61	72
03	$2.5 \cdot 10^{-7}$	10.57	131.7
04	$1.3 \cdot 10^{-7}$	11.14	33.4
05	$1.3 \cdot 10^{-7}$	11.27	62
06	$1.3 \cdot 10^{-7}$	11.7	44
07	$1.8 \cdot 10^{-7}$	10.81	53.6
08	$1.8 \cdot 10^{-7}$	10.69	81.3
09	$1.8 \cdot 10^{-7}$	10.65	133.1

TABLE 5.2: Test matrix employed during CO_2 testing.

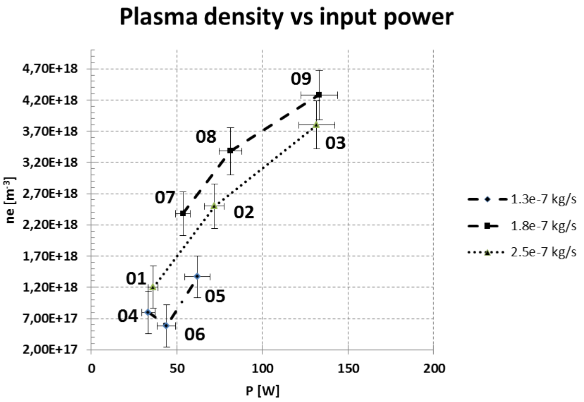

FIGURE 5.4: Plasma density as a function of input power for three mass flow rates. The reference numbers of the experimental points are reported. The intermediate value of $1.8 \cdot 10^{-7}$ kg/s produces the highest densities, indicating the existence of an optimal mass flow rate within the explored range. Point 06 was judged spurious, since

5.4 Intermediate power testing

From the preliminary HPT configuration presented in 5.1 it emerges that the high power HPT presents an higher surface power density P_{in}/S with respect to HPH.Com: indeed the ratio between the overall surface of the HPH.Com plasma source (19 mm in diameter and 50 mm in length [13])and that of the new high power HPT is $S_{highP}/S_{HPH} \approx 3$, while the ratio between the corresponding input power ranges between 20 and 30, meaning that the new thruster will have approximately 7-10 times the surface power density of HPH.Com. This is important for thermal control issues, since,for a given plasma

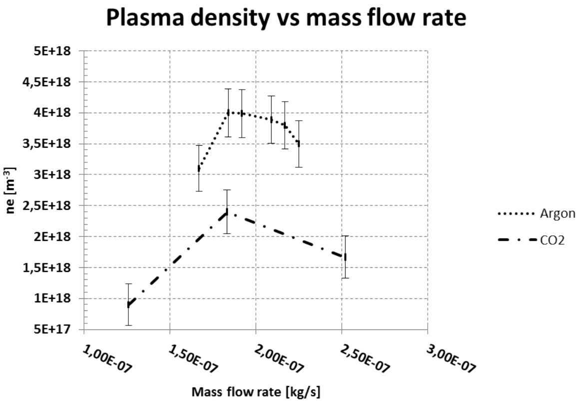

FIGURE 5.5: Plasma density as a function of mass flow rate for an input power of 50 W for the tested plasma source configuration. Both Argon and CO_2 exhibit an optimal mass flow rate, which appears to be related to the configuration of the source itself and not to the type of propellant. Argon allows to obtain higher densities with respect to CO_2, probably due to a lower ionization energy.

source efficiency η_s , the waste heat flux to be dissipated becomes $Q_w = P_{in} \cdot (1 - \eta_s)$, which is directly proportional to P_{in}, meaning that the high power thruster will have to dissipate a waste heat 20-30 times that of HPH with only 3 times the surface to do it. This results in higher operating temperatures, which may affect the performance of the plasma source, thus requiring a preliminary investigation of this new operating regime. Tests at a power level up to 480 W were performed on the existing plasma source, with the goals of (i) observing how its performance scales with increasing power and (ii) exploring the occurrence of issues related to the higher power density, with special attention on antenna performance and thermal or electrical damage to components. The plasma source configuration employed in the tests is the same described in 5.3. The operating gas was Argon, in order to allow a comparison with the low power measurements performed in HPH.Com.

5.4.1 RF atenna performance

A preliminary series of tests (Figure[5.6]) with power up to 265 W was carried out with the low power RF antenna developed for the 50 W HPH.Com thruster, monitoring its electrical impedance as the power level was raised, as reported in Table[5.3]. During operation it was observed that, as the power was increased up to 160 W, the impedance of the antenna progressively decreased below 30 Ω, in spite of the attempts of impedance matching. This may indicate that there is a probability that for the higher power levels required by this work this value may experience a further decrease, which would in fact hamper the impedance matching with the RF amplifier, decreasing the power transfer efficiency.

Test	$\dot{m}$ [kg/s]	f [MHz]	V [V]	I [A]	$\Delta\phi_1$ [°]	P [W]	Z [Ω]
1	$2{\cdot}10^{-7}$	12.90	65	1.7	0	54	38
2	$2{\cdot}10^{-7}$	12.90	75	2	0	75	37.5
3	$2{\cdot}10^{-7}$	12.88	90	2.5	0	112.5	36
4	$2{\cdot}10^{-7}$	13.13	95	3.5	0	156	27

Table 5.3: Preliminary power scaling test.

.

In order to contain this effect it was decided to increase the inductive part of the antenna, in order to increase its impedance near the same operating frequency. A new antenna was jointly designed and manufactured with RESIA with this goal and tested without impedance matching issues up to 275 W (Table[5.4], Figure[5.6]), testifying the validity of the adopted solution.

Test	$\dot{m}$ [kg/s]	f [MHz]	V_1 [V]	I_1 [A]	$\Delta\phi_1$ [°]	P [W]	Z [Ω]
1	$2{\cdot}10^{-7}$	10.07	240	1.8	0	194	133
2	$2{\cdot}10^{-7}$	10.05	265	2	0	239	132
3	$2{\cdot}10^{-7}$	10.03	290	2	0	275	145

Table 5.4: Testing of the high power RF antenna. The new design was capable of operation up to 275 W without relevant issues related to impedance matching.

.

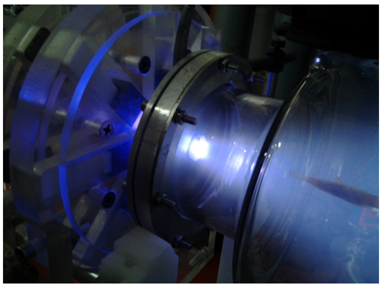

Figure 5.6: Testing at 275 W: the plasma source in action.

5.4.2 Plasma source issues

Operation with RF at higher power levels and power density introduces on the plasma source a series of issues related both to electrical insulation and thermal loads, which were explored during the preliminary testing:

- the increase in the operating power led to higher electric power losses in the antenna and higher waste heat generation from the plasma source; the correspondingly higher thermal loads produce higher temperatures, which in turn lead to an increase in the resistivity of conductors and to the modification of the dielectric properties of insulating materials;

- due to the increase in temperature connected to higher thermal fluxes the antenna is subject to a sensible decrease of its efficiency, since parasitic resistances increase, as shown in Figure[5.7]: as the temperature of the antenna increases its input impedance, measured by means of a V/I probe, decreases progressively, indicating an increase in the parasitic resistances. The impedance was measured without plasma, so that any resistive components were due to parasitic resistances alone. Both ohmic dissipation and power loss in the dielectric of the capacitor contribute to parasitic dissipation.
  No dielectric breakdown phenomena on the antenna occurred during the tests, but this possibility must still be considered as the operating voltage will have to be further increase in order to reach the target operating power;

- the Pyrex tube containing the plasma is subject to the same intense thermal loads experienced by the antenna, aggravated by the erosive effect of particle fluxes against its inner walls and by the high voltage difference between the antenna conductors (2 kV or more) on the outside and the plasma on the inside of the chamber. The combined effect of these issues was heavy: indeed catastrophic perforations of the Pyrex wall of the chamber were observed after prolonged (¿ 5 min) continued operation, generating the damage shown in (Figure[5.8]): a small hole, surrounded by a zone in which glass appears to have melted and solidified again, apparently testifying an electric arc between the plasma and the antenna though the Pyrex wall, probably triggered by temperature and voltage and facilitated by impurities in the wall itself.
  The issue was mitigated by means of kapton tape placed between the antenna and the discharge chamber outer wall, which greatly improved the electrical insulation.

The SmCo permanent magnets rings constituting the magnetic system of the plasma source 2.2.1, on the other hand, experienced only limited heating, since their temperature never exceeded 30 $\circ$C. This implies that this subsystem faces much less critical power density issues with respect to the antenna and the discharge chamber, expecially if it is considered that such magnets can operate up to a temperature of 250 - 300 $\circ$C [26].

These observations led to the following solutions for the high power HPT test-bed, aimed at ensuring operation with the target power density while containing complexity and costs:

- in-air mounting, in the fashion of the external experiment developed during HPH.Com (2.2.1), in order to ease heat dissipation with the help of the surrounding atmosphere;
- employiment of high temperature electrically insulating materials, such as kapton;
- minimization of parasitic resistances in the antenna, by means of Litz wire or other conductors more suited for operation in presence of skin effect [27];
- limitation of the operating time, with relatively brief plasma ignitions followed by a proper cooling time.

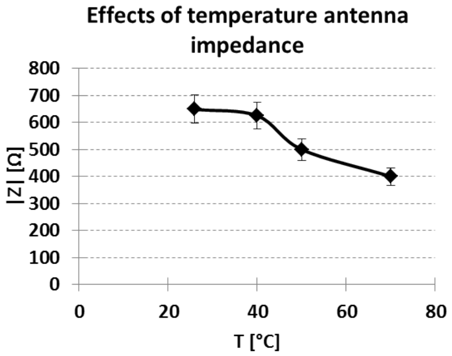

FIGURE 5.7: Experimental characterization of the effect of temperature on antenna impedance, measured without plasma. The temperature was measured with a PT-3850 thermo-resistance placed directly on the quartz support of the antenna, while the impedance was monitored by means of a V/I probe

FIGURE 5.8: Perforation of the discharge chamber wall: the damage is limited to a relatively small hole, surrounded by a zone showing signs of thermal stress. This was interpreted as a sign of an electric arc between the plasma and the antenna.

5.4.3 Performance scaling

The new high inductance antenna developed in 5.4.1, after having proven capable of operation at power levels superior to those of previous antennae, was employed to characterize the performance of the plasma source up to the target intermediate power of 500 W, in terms of emission spectra and plasma density. The set-up was the same used for the preliminary antenna characterization (5.4.1), with the exception of the outlet section diameter, set at 10 mm since during the previous tests the 5 mm outlet disk was subject to intense wearing and was removed. The operating gas was again Argon.

In order to eliminate thermal effects on antenna efficiency all measurements were taken after antenna cool-down to room temperature. The test matrix is reported in Table[5.5]: it was decided to perform all measurements witoh the same mass flow rate, in order to observe the effects of the input power alone. A maximum peak of 480 W was reached, corresponding to a power density ten times superior to that of project HPH.Com.

Test	$\dot{m}$ [kg/s]	f [MHz]	V_1 [V]	I_1 [A]	$\Delta\phi_1$ [°]	P [W]	Z [Ω]
1	$2{\cdot}10^{-7}$	10.17	110	0.85	0	47	129
2	$2{\cdot}10^{-7}$	10.12	150	1.2	0	90	125
3	$2{\cdot}10^{-7}$	10.08	225	1.9	0	214	118
4	$2{\cdot}10^{-7}$	10.00	300	2.5	0	362	116
5	$2{\cdot}10^{-7}$	10.06	320	3	0	480	107

TABLE 5.5: Plasma source performance scaling.

.

The electrical performance of the antenna appears qualitatively unchanged as the power level is increased. No discontinuities in the variation of the impedance matching were registered, indicating that probably the plasma discharge mantains the same regime, although at progressively higher ionization level. This is supported also by observation of the plasma by means of CCD cameras, which reveals that in all cases the same discharge structure usually observed in the CISAS plasma source, characterized by a rather small and intensely bright plasma core surrounded by excited neutrals, takes place (Figure[5.11], cfr. with Figure[2.16]).

Figure[5.9] reports the measured values of plasma density plotted against the corresponding input power: the density is monotonically increasing with power, following a trend which is well modeled by a power fit of the data, resulting in a curve with equation $n_e(P)$=$3 \cdot 10^{17} \cdot P^{0.492}$, with P in watts and n_e in m^{-3}. A qualitatively similar trend is exhibited by the ArII/ArI lines intensity ratios , calculated as explained in 2.3.2, as shown in Figure[5.10]: all the four ratios monotonically increase with power, indicating that a progressively greater part of the gas is ionized, but the increase becomes smaller as power is increased. The overall trend against the input power was estimated by performing an analytical fit of the cloud of points obtained by plotting together the four ratios, resulting in a power law with equation $ArII/ArI(P)$=$0.194 \cdot P^{0.265}$, with P in watts.

This effect may be related to some sort of saturation mechanism, such as the progressive depletion of neutrals from the source and the progressive increase of plasma losses towards the walls of the discharge chamber and through the outlet orifice, which is compatible with the increased power density level.

In all, the experimental observations indicate that it is possible to scale this plasma source technology at the power density required by this work without alteration of the qualitative behavior of the antenna and the plasma discharge; the performance of the source, in terms of plasma density and ionization fraction, scales monotonically with power, following a non-linear trend probably indicating a progressive saturation mechanism. Furhter testing at higher mass flow rate levels is currently planned in the immediate future within the existing research programs at CISAS.

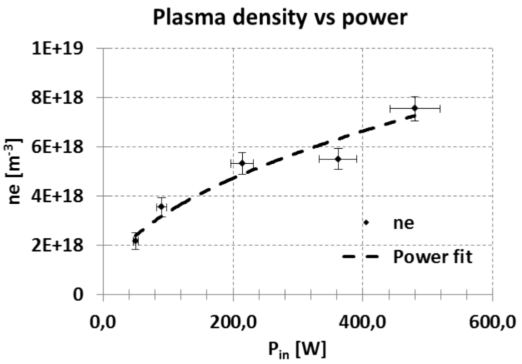

FIGURE 5.9: Experimental measurement of plasma density against the input power. Density increases monotonically with the input power, according to a trend well modeled according to the power law $n_e(P)=3 \cdot 10^{17} \cdot P^{0.492}$.

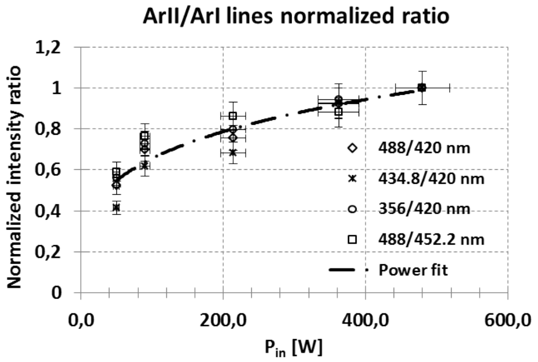

FIGURE 5.10: Trends of the ArII/ArI lines intensity ratios, normalized to their maximum value, plotted against the input power. The cloud of points resulting from the plotting of the four ratios is well fitted by the power law $ArII/ArI(P)=0.194 \cdot P^{0.265}$, thus indicating that the trend against the input power of the ArII/ArI ratios is similar to the one exhibited by plasma density.

5.5 Accessory systems and components

Accessory systems include all the elements of the experimental set-up which are not directly part of the plasma source but are essential to its operation, such as cables, V/I probes, the mass flow rate controller and vacuum pumps. The performance of these systems at the target power and mass flow rate levels has thus to be analyzed, in order

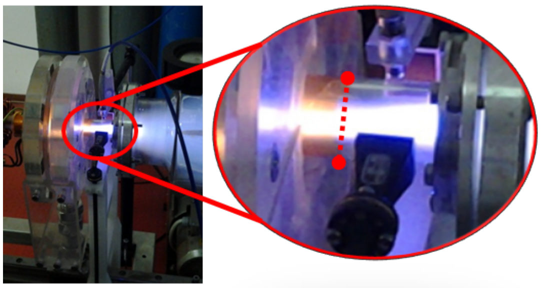

FIGURE 5.11: 275 W plasma discharge, with a zoom on the plasma immediately upstream the outlet section. The red dotted line evidences the diameter of the di scharge chamber, which is sensibly larger than the diameter of the plasma column.

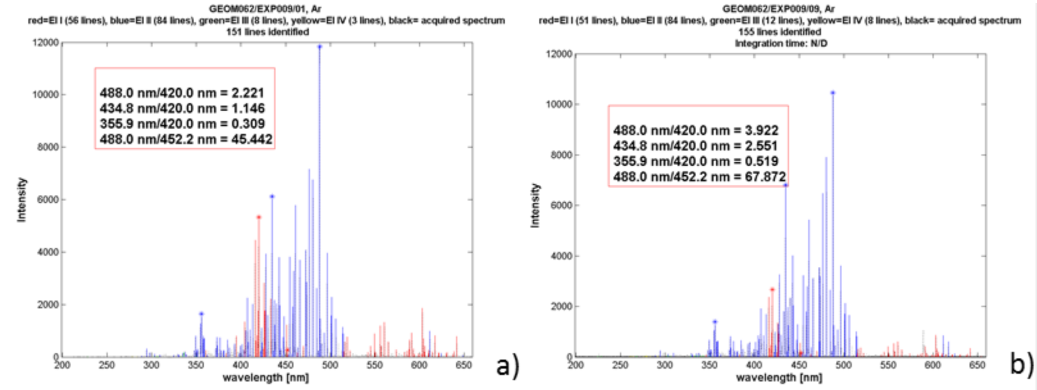

FIGURE 5.12: Comparison of the emission spectra in the 220-650 nm range taken at 47 W (a) and 480 W(b). Blue lines are those related to ArII (ions) emission, while red is used to evidence ArI (excited neutrals) emission lines. As it can be seen the relative intensity of ArII lines with respect to ArI lines increases in the high power spectrum, indicating a greater ionization level which is coherent with the measured increase in plasma density.

to identify the eventual upgrade interventions required to enable the desired tests. During the intermediate power testing the elements of the RF circuit devoted to feed the antenna, such as coaxial cables and V/I probes, did not experience significant heating phenomena; operating at the target power level of 1-1.5 kW, however, will further increase the stress to which these components are subject, in terms of operating voltages, currents and waste heat generation. In the existing set-up power is carried by RG-213 cables equipped with N-type connectors, rated for a maximum RMS voltage of 1000 V and a maximum power ranging up to 2.5 kW for an operating frequency within 10 MHz [28, 29], which includes the typical operating frequency of CISAS HPT (2-15 MHz). Thanks to these characteristics these cables are capable of withstanding the operating power needed for high power testing, provided that the maximum RMS voltage is is not exceeded.

V/I probes, on the other hand, are rated for operation up to 500 W by RESIA, which will provide upgraded probes for higher power operation. The mass flow rate controller currently in use has a maximum output of 11 SCCM of Nitrogen (2.2.1), corresponding to $\approx 4.6 \cdot 10^{-7}$ kg/s of Argon and $\approx 2.5 \cdot 10^{-7}$ kg/s of CO_2, meaning that a new controller will be required. The same family of devices [30], however, includes devices capable of operation at much higher mass flow rates, among which the MKS 1179A01322CS1BV [30], capable of 200 SCCM of Nitrogen, was selected, although not yet purchased at the time this thesis was being written. The new device shall provide up to $9.2 \cdot 10^{-6}$ of Argon and $5 \cdot 10^{-6}$ of CO_2, fully satisfying the design mass flow rate requirements.

The last note is related to the analysis of the high vacuum pumping system (2.1.1), in order to develop a reliable estimation of the pressure level which is expected at the mass flow rate levels required by high power operation (up to $4.4 \cdot 10^{-6}$ kg/s, about ten times HPH.COM). This was done by first estimating the actual pumping capacity of the vacuum system, which, due to tubes and other connection elements placed between the pumps and the vacuum chamber, is tipically inferior to the nominal capacity of the pumps themselves. This analysis was based on the following relation, expressing the pumping capacity Q to the required operating pressure P_0 and to the vacuum chamber volume v [31]:

$$Q = \frac{dP}{dt} \cdot \frac{v}{P_0} \tag{5.1}$$

Here dP/dt is the pressure increase as a function of time generated by the input mass flow rate to be compensated by the pumps, connected to the gas mass flow rate through the following relation:

$$\frac{dP}{dt} = \frac{1}{v} \cdot \frac{\dot{m}}{M_m} \cdot R \cdot T \tag{5.2}$$

with $\dot{m}$ the mass flow rate, M_M the molar mass of the gas, R the universal gas constant and T the gas temperature in K. This flow includes both the propellant employed by the thruster, which is set and known with an accuracy of ± 0.01 SCCM ($4 \cdot 10^{-7}$ kg/s of Ar), and the undesired leakage flux of external air from vacuum seals and outgassing from materials inside the chamber.

The overall leakage flux and the effective pumping capacity Q_{eff} were determined iteratively from eq. 5.1, substiuting to P_0 the typical base pressure detected inside the vacuum chamber without a propellant mass flow rate, corresponding to $8 \cdot 10^{-6} \pm 30$ % mbar. The volume of the chamber is $v = 2 \cdot \pi \cdot (0.6/2)^2 = 0.57$ m^3.

Starting from the nominal pumping capacity of the vacuum system (Q_{nom}=12600 l/s) the iterations converged to Q_{eff}=3045 ± 30 % l/s, with a leakage pressure rise dp_l/dt=4.37

± 30 % Pa/s; as expected the value of Q_{eff} is considerably lower than the nominal capacity of the pumps, mainly due to the tubes connecting the pumps to the vacuum chamber, whose usage was imposed by the geometrical constraints of the facility.

Q_{eff} was used to estimate the operating pressures of the chamber for various mass flow rates, performing also a comparison against experimentally measured pressure, detected by means of the Edwards AIM-S-NW25 active inverted magnetron gauge described in 2.1.1. The results are portrayed in Figure[5.13]: the theoretical predictions match the experimental measures within the respective uncertainty ranges, confirming the validity of the estimation of Q_{eff}, but this implies that, at the mass flow rate values required by high power operation, the operating pressure will be an order of magnitude higher with respect to that experienced during low power testing (up to 10^{-3} mbar against a maximum of 10^{-4} mbar). This will probably affect the measurements performed with electrostatic probes in the plume of the thruster, but similar operating conditions are experienced in other high power HPT experiments, such as the one described by Takahashi and Boswell [32], executed in a 0.6 m wide and 1.4 m long cylindrical vacuum chamber connected to a 400 l/s pump: in this case a 25 SCCM mass flow rate of Argon ($1.5 \cdot 10^{-6}$kg/s) results in a pressure of 0.8 mTorr ($\approx 1.05 \cdot 10^{-3}$ mbar), relatively higher than the 2-4 $\cdot\ 10^{-4}$ mbar allowed by CISAS facility for the same mass flow rate. This indicates that the testing conditions at CISAS will be similar or even better than those experienced by other similar experiments under the point of view of the operating pressures; this, however, does not exclude the eventuality of an improvement, which may be required to improve the quality of plume diagnostics measurements, but in this case Q_{eff} may be increased by re-arranging the connection tubes between the pumps and the vacuum chamber, reducing wherever possible the presence of L-shaped turns and enlarging their diameters in order to improve their conductance and thus take more profit from the full pumping capacity of the existing system.

5.6 High power test-bed design and development

This part of the work saw its culmination in the design and development of the high power test-bed, carried out according to what was observed in the previous phases. In order to contain costs and complexity it was decided to develop the new set-up as an upgrade of the low power external experiment (2.2.1), thus employing as much of its existing components as possible while respecting the requirements illustrated in 5.1.

This activity was subdivided into three main parts, each one related to the key subsystems of the test-bed, namely (i) the discharge chamber, (ii) the RF antenna and (iii) the magnetic system.

As a final side activity, it was decided to perform the preliminary design of an high

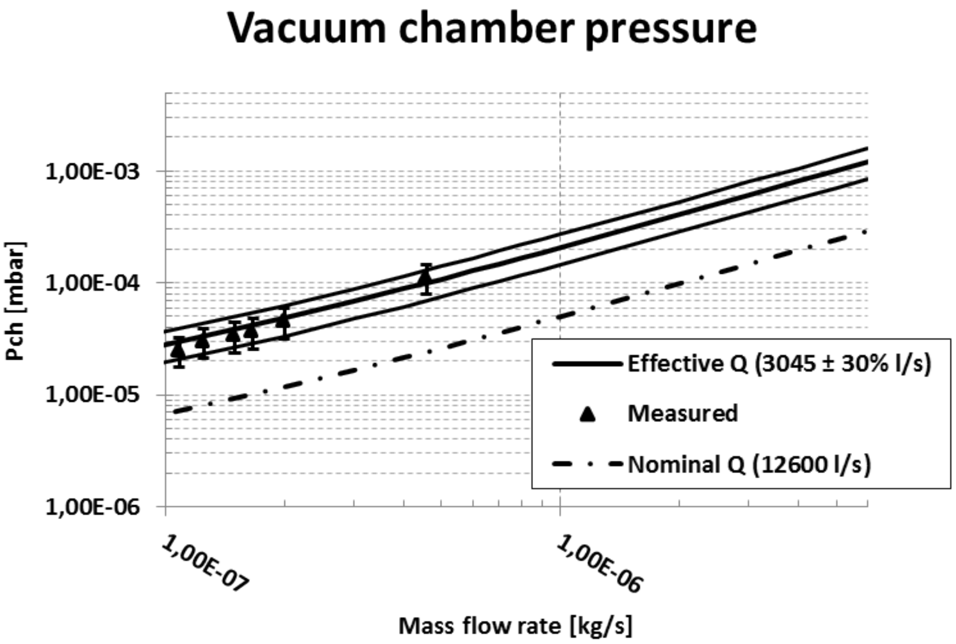

FIGURE 5.13: Estimation of the pressure inside CISAS vacuum chamber for different values of mass flow rate according to the estimated effective pumping capacity Q_{eff} (solid line). The estimated pressures match the experimentally measured ones within their uncertainty ranges. The system, due to connecting elements, operates at a considerably lower pumping capacity with respect to that theoretically allowed by the pumps, which would allow far lower pressures (dash-dotted line).

power HPT prototype for operation with CO_2, in order to identify in advance possible design solutions useful for the future developments of the STRONG - SAPERE project.

5.6.1 Discharge chamber

The discharge chamber was designed taking into account the geometrical requirements of both the Argon and CO_2 HPT configurations presented in 5.1; the two are in fact very similar in terms of diameter (38.8 mm and 49 mm respectively) and length (109 mm in both cases): this allows to employ the same chamber for both cases, adopting a compromise diameter, in order to reduce costs and complexity. Pyrex, due to its high softening temperature (≈ 820 °C), low cost and ease of manufacturing, was again chosen as the material for the chamber.

The design was carried out by performing a survey of the commercially available standard Pyrex tube diameters, resulting in the configuration reported in Table[5.6]: it was decided to employ a standard tube with an inner diameter of 40 mm, which was judged as the best solution in order to satisfy the geometrical requirements, and a wall thickness of 2 mm, which was test proven against the pressure differential between the inner vacuum and the external atmosphere. The length of 350 mm was chosen in order to allow the variation of the discharge chamber length in a wide range around the design value for characterization and optimization purposes.

Parameter	Value
Inner diameter	40 mm
Wall thickness	2 mm
Length	350 mm

Table 5.6: Key features of the discharge chamber.

Figure[5.15] shows the new discharge chamber tube, compared with the existing one developed for HPH.Com. The variation of the outlet section diameter was provided by means of a set of Macor ceramic rings, 5 mm thick and with various inner diameters (10,20 30 mm), designed to be housed between the discharge chamber and the outlet flange, resembling the solution adopted in the low power set-up (2.2.1).
Since the new discharge chamber was intended for operation with the existing external set-up, the design of new interfaces was required, namely:

- a new outlet flange, providing the interface between the discharge chamber and the expansion bell. The flange is in fact a copy of the existing one, made of aluminum, mantaining the same interface with the expansion bell but with an enlarged one for the discharge chamber and the outlet disks;
- a new vacuum interface between the chamber and the neutral gas injection tube, designed to allow its axial movement. Also in this case the new interface is an enlarged version of the low power one, based on steel sleeves and viton O-rings;
- new ceramic head for the injection tube, with an enlarged diameter (37 mm vs the 18.6 mm of the low power set-up) intended to limit eventual plasma backflows towards the rubber seals of the vacuum interface.

A CAD assembly of the new discharge chamber and its interfaces can be seen in Figure[5.14], which also reports the main geometrical dimensions.
As of now all the components of the new discharge chamber have been manufactured and vacuum-tested.

5.6.2 Antenna design

The design of the antenna took into account several factors, namely:

- the inner diameter of the antenna must obviously fit the outer diameter of the discharge chamber, around which it is wrapped;

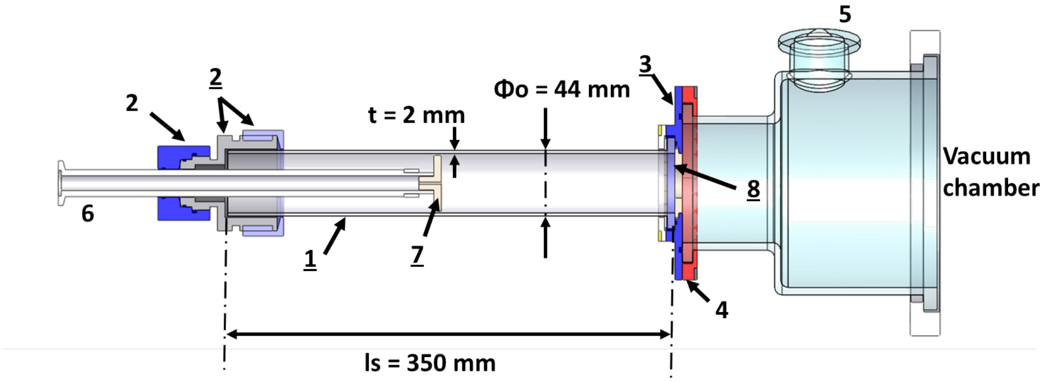

Figure 5.14: CAD model of the new discharge chamber set-up. Underlined numbers refer to the new components, while others denote existing ones developed for the low-power experiment. 1) discharge chamber (pyrex). 2) vacuum seals (stainless steel). 3) outlet flange (aluminum). 4) outlet flange interface (aluminum). 5) expansion bell (pyrex). 6) gas injection tube (stainless steel). 7) injector head (macor). 8) outlet disk (macor).

Figure 5.15: The existing discharge chamber (left), developed for HPH.Com and characterized by an inner diameter of 19 mm, and the new one (right).

- according to the results illustrated in 4, the axial electric field must be maximized near the outlet region in order to maximize the performance of the thruster;
- the parasitic resistances of the conductors must be kept as low as possible;

Several antenna configurations were considered, estimating for each of them the related electrical parameters (R, L, C), combining the lumped-parameters model with electrostatic and magnetic FEM simulations, according to the method illustrated in 3.3. Table[5.7] reports the selected solution, based on an inductive design, in which parasitic resistances were minimized by employing a 7-strands Litz wire (overall wire radius 2 mm), in order to reduce the skin effect losses. A relatively small parasitic capacitance is also present in parallel to antenna inductance. The length of the antenna was adjusted in order to maximize the inductance of the antenna, according to what observed in 5.4.1. In order to maximize the electric field across the outlet section an additional ring electrode (length 5 mm, thickness 0.5 mm), connected to ground, was placed around the discharge chamber according to the scheme illustrated in Figure[5.16].

Parameter	Value
Inner diameter	45 mm
Outer diameter	67 mm
Length	108 mm
L	56 μH
R @ 1 - 2 MHz	$\approx$ 1 - 1.5 Ω
C_{par}	25 pF
Ztot @ 1 - 2 MHz	335 - 577 Ω

TABLE 5.7: Key features of the high power antenna.

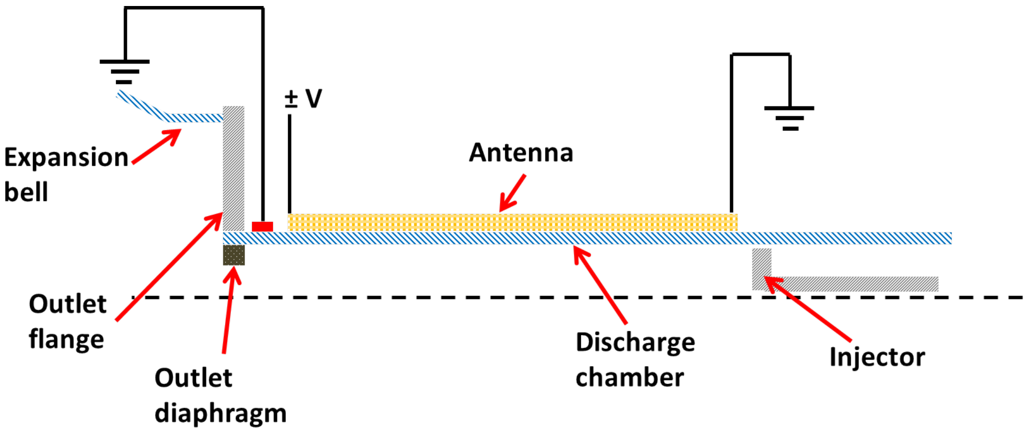

FIGURE 5.16: Scheme of the high power antenna configuration. A grounded metal ring is added between the antenna and the outlet section in order to maximize the axial electrical field in such region.

In the range of 1 - 2 MHz, corresponding to the estimated operating frequency span, the antenna has an almost purely reactive impedance, whose modulus ranges between 335 -577 Ω without plasma, whose presence is expected to produce an alteration of these values whose entity cannot be precisely estimated *a priori*. This variability is not a critical issue, since the dedicated RF amplifier and matching system devised for this application are capable of ensuring high efficiency operation even with an highly variable load impedance (see 6).

5.6.3 Magnetic system

For the sake of cost containment it was decided to investigate the possibility of meeting the magnetic field requirements of 5.1 with the existing electromagnets and permanent magnets (see 2.2.1).

The analysis in first place the existing electromagnets, whose optimal arrangement and current feeding were studied by means of simulations FEMM [22], taking into account the limits of the DC power generators currently available, an EUTRON BVR2000 60-30 and a Sorensen DCR60-30B, whose maximum voltage and current rating is of 60 V and 30 A respectively. It is also necessary to consider the constraint of the axial space required by the antenna, since its external diameter of 67 mm exceeds the 60 mm inner diameter of coil supports, which cannot be enlarged without dismantling the magnets themselves. This results in a minimum axial distance of 108 mm between the two pairs of coils.

The results of the simulations, shown in Figure[5.17], indicate that it is possible to achieve a mean axial field of 1349 G within the source, corresponding to ≈ 90% of the required value, by means of the two inward-facing coils (S2 and S3 in the figure) fed with a current I_c =30 A. Since the DC resistance of the coils corresponds to R_c= 2 Ω at room temperature, the required voltage becomes $V_c=R_c \cdot I_c=60$ V; this means that both DC generators will be operating at their limit performance and will not be capable of compensating an increase in the resistance of the coils due to heating, but operation at such high currents with the low power plasma source has shown that the heating process is very slow, thanks to the high thermal inertia of the coils (each one has a weight of 15 kg) and to the great surface of their housings, allowing several minutes of continued operation before cool-down is required. A flow of cold gas, achieved by expanding compressed air or Nitrogen, can be injected inside the coils housings, in order to ease their cooling.

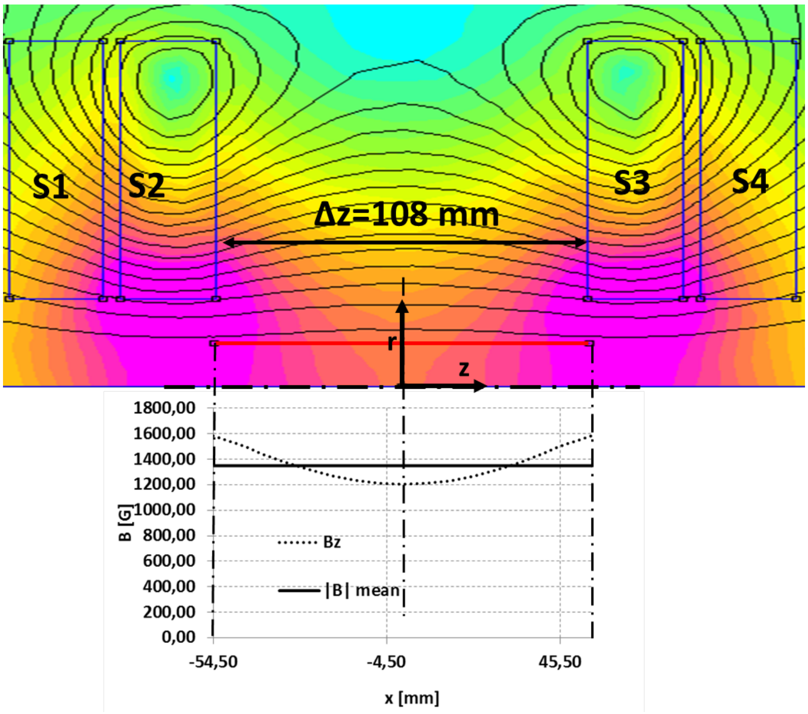

FIGURE 5.17: Electromagnets set-up for the high power experiment. The solenoids S2 and S3 are fed with a 30 A DC current. The axial spacing of 108 mm is required by the RF antenna.

The existing 20x20x20 mm SmCo permanent magnets were analyzed as well, but it was found to be impossible to achieve the desired field with the existing set-up. For this reason FEMM was employed to design a new permanent magnets system, taking inspiration from the one developed for the low power in-vacuum model (2.2.2), based on two radially magnetized SmCo permanent magnets rings. The result is shown in Figure[5.18]: the system employs two radially magnetized rings, axially spaced by 10 mm, a value which considers the thickness of the mangnets housings. Each ring has an inner diameter of 74 mm, in order to allow the antenna to be placed under it, an external diameter of 60 mm and a length of 43 mm. The figure shows the estimated axial magnetic field along the inner lateral face of the discharge chamber: FEMM simulations work in the hypothesis of a perfectly axisymmetric geometry, while in fact the rings were designed as composed of 6 wedge shaped elements, each magnetized along the radius of the ring and covering a 58° arc: this solution, mutuated from the low power in-vacuum model, was chosen since it has proven extremely difficult to manufacture monolithic radially magnetized rings, thus requiring them to be assembled from smaller elements approximating as closely as possible an ideal ring. A small gap, covering $\approx 2°$, was left between the wedges in order to ease mounting. The output axial magnetic field from FEMM, $B_{z,FEMM}$, was thus corrected by means of an angular coverage factor, taking into account the actual geometry of the magnets and defined as:

$$cf = \frac{\alpha_m \cdot M}{2 \cdot \pi} \tag{5.3}$$

where M is the number of magnets in each ring (8) and α_m is the angular coverage of each magnet (58°) and . With these values $cf \approx 97\%$ and the effective magnetic field results to be $B_{z,eff} = B_{z,FEMM} * cf$. The estimated intensity of $B_{z,eff}$ has a mean value of 1574 G along the inner lateral wall of the plasma source, slightly exceeding the 1500 G requirement.

The magnets are to be housed in a dedicated support made of PEEK, a plastic material characterized by good mechanical and thermal properties, already employed in the in-vacuum model. Each support has a length of 50 mm, an inner diameter of 68 mm and an outer diameter of 66 mm.

As of now the new permanent magnets have been designed but not yet manufactured.

5.7 High power thruster preliminary design

The final development of this part of the work has been the preliminary design of the high power HPT design featuring CO_2 as the propellant. This activity was carried out

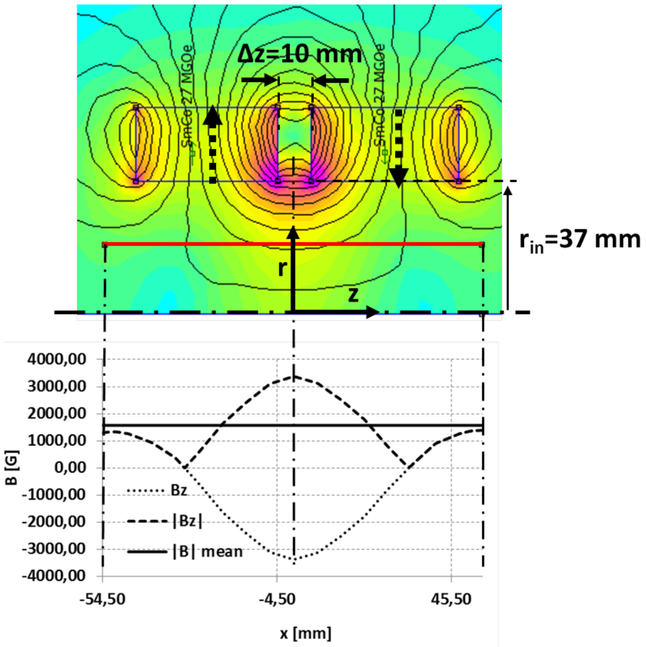

FIGURE 5.18: Permanent magnets set-up for the high power experiment. The system features the same SmCo magnets and plexiglas supports already developed for HPH.Com.

in order to identify in advance the possible solutions for an actual prototype, whose manufacturing is required by the ongoing research project SAPERE - STRONG. CO_2 was chosen since this propellant constitutes the likely final choice for the project.

The design features the same antenna and magnets designed for the reconfigurable set-up described in the previous sections, but the discharge chamber was re-designed for thermal control purposes. A structural frame was also designed, along with thermal and EM insulation elements.

The design was specifically optimized in order to (i) minimize the operating temperature of all sensible components, namely the antenna and the magnets, which were estimated by means of COMSOL simulations and (ii) minimize mass and size, estimated by means of a 3D CAD model of the HPT. The result can be seen in Figure[5.19]: the design has an overall diameter of 145 mm and a length of 162 mm, with an overall weight of 6.37 kg.

Structural integrity is ensured by a ”cage” structure, composed of an aluminum back flange and a cBN (cubic boron nitride) frontal flange, connected by four longitudinal aluminum bars. this structure houses the magnets, encased in a PEEK frame, the antenna and the discharge chamber, made of cBN. This material was chosen due to its relatively high thermal conduction coefficient (200 -740 W/(m K)), high hardness (10 Mohs), ensuring low erosion due to plasma, and high melting point (3246 K). Structural simulations revealed a resonant frequency of 1711 Hz, well above the 200 Hz limit judged safe for compatibility with most space launch systems.EM shielding is ensured by an

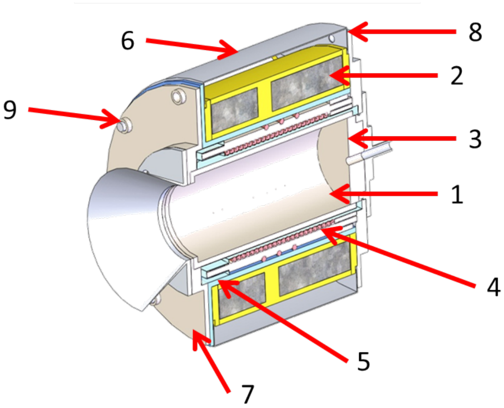

FIGURE 5.19: CAD model of the CO_2 high power HPT. 1) discharge chamber. 2) magnetic system. 3) injector. 4) antenna. 5) thermal insulation layer. 6) EM shield. 7) frontal flange. 8) back flange. 9) Al_2O_3 insulating washer.

aluminum skin closing the side of the structural frame.

Thermal control is ensured by a completely passive system: considering that, with an input power $P_{in} \approx 1496$ W, the estimated propulsive efficiency of the device is $\eta_p \approx 67\%$, while the antenna efficiency η_a is estimated around 90%, it becomes clear that the great part of the waste heat ($\mathrm{Q}_s = (1 - \eta_a) \cdot \eta_p \cdot P_{in} \approx 658$ W) will be generated from the plasma source itself, with minimal ohmic power dissipation from the antenna ($\mathrm{Q}_a = \eta_a \cdot P_{in} \approx 150$ W). For this reason it was decided to develop a thermal control system (TCS) which divides the thruster in two separated thermal circuits, an "high temperature" one, composed of the discharge chamber and the frontal flange, devoted to venting the waste heat of the plasma source, and a "low temperature" one, composed by the antenna, the back flange, the injector, the longitudinal bars and the EM shield, which eliminates the waste heat generated by the antenna. The circuits are separated by means of an insulating layer of Pyrogel, an high-temperature insulation blanket formed of silica Aerogel and reinforced with a non-woven, glass-fiber batting (thermal conductivity below 0.09 W/(m K) for $\mathrm{T} \leq 600$ °C), and by Al_2O_3 washers at the joints between the longitudinal bars and the frontal flange. The thermal control philosopy is evidenced in Figure[5.20]. Simulations show that, thanks to this solution, it appears to be possible to maintain the thruster at acceptable operating temperatures with virtually no impact on the TCS of the spacecraft carrying it. The estimated operating temperatures of the main thruster components are reported in Table[5.8], evidencing that it is possible to limit their values well below the maximum allowable temperatures of the components. These were calculated as 0.9 times the melting point of the relative materials for the discharge chamber, the aluminum structural elements and the EM shield, while for the magnets the maximum temperature indicated by the manufacturer was chosen. For antenna conductor the value was set in order to limit the increase in resistivity of conductors without imposing too heavy constraints on the TCS.

	Discharge chamber	Frontal flange	Antenna	Magnets	EM shield	Back flange
T_{mean} [K]	642 K	623	538	500	466	521
T_{lim} [K]	2921	2921	600	523	840	840

TABLE 5.8: Operating temperaure of thruster components, estimated by thermal simulations. The maximum allowed temperatures (T_{lim}) are never exceeded.

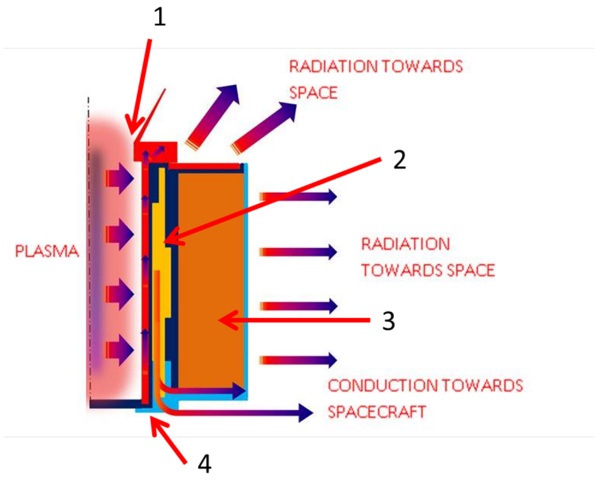

FIGURE 5.20: Thermal control philosophy of the HPT. Conduction heat exchanges with the supporting structure can be minimized, since the thruster is capable of self-cooling with minimal impact on the TCS of the spacecraft carrying it. 1) high temperature circuit (discharge chamber and forward flange). 2) antenna. 3) magnets. 4) back flange and lateral EM screen (low temperature circuit).

Chapter 6

High Power RF Generation System Design and Development

This chapter describes the design and development of the RF power generation system for the high power HPT test-bed, jointly carried out by CISAS personnel and dr. Antonio Selmo, by RESIA, an expert electronic engineer and CISAS external collaborator. The system was designed for high efficiency operation with variable load condition, which, in the case of the HPT, is determined by the complex impedance of the antenna. The latter can be subject to variation due to two main issues, covered in detail in 3 and here briefly recalled:

- ohmic heating of the electric conductors, with subsequent increase of parasitic losses and decrease of antenna impedance modulus;
- variation of the equivalent plasma impedance, both in terms of plasma resistance R_p and reactance X_p, which in turns generates a change on either the resistance or reactance of the antenna at a given frequency.

The latter, in particular, takes place if the operating regime of the thruster (power, mass flow rate, propellant type) or its configuration (geometry, magnetic field) are changed by purpose, as it happens in characterization tests. The two issues, anyway, are often coupled.

These considerations, under the design point of view, mean that the power generation system must be capable of high efficiency power transfer to the antenna in the widest possible range of antenna impedance value. This goal was met by developing (i) an innovative RF amplifier, capable of high efficiency operation up to 2 MHz and driven by (ii) an impedance matching system, designed to compensate in real-time the variations of the impedance of the antenna due to the plasma and based on a fixed capacitive network and an automatic frequency adjustment system.

An high efficiency has moreover the important consequence of enabling the space-based use of the developed technology, in the frame of the ongoing research activity

Within the frame of this activity the author has taken part to the preliminary design and to the testing of the RF amplifier, which was designed in detail and manufactured by RESIA, and to the preliminary design of the automatic frequency matching system. The device is intended for use in the high power testing set-up, but was developed keeping an eye to an eventual space-based application.

As of now an intermediate power prototype the amplifier, constituting the most innovative part of this activity, has been manufactured and is undergoing preliminary testing, while the impedance matching system has been preliminarily designed but not yet manufactured due to time issues.

6.1 RF power amplifier

6.1.1 General concepts

Ideally an amplifier is a device based on non-linear elements, mainly transistors (BJT, MOSFET, JFET) capable of increasing the magnitude of an input AC signal without altering its waveform [33]. Figure[6.1] shows the scheme of an elementary A-class amplifier (the meaning of this classification will be clearer later): here the non-linear element is a Base Junction Transistor (BJT), inserted in a polarization network which ensures that the element works in a condition where there is a linear dependence between the input, and the output: the variations of the input voltage V_i produce proportional variations of I_b, the current flowing in the base of the BJT, which in turns generates proportional variations of the current I_c flowing through the load in the collector, according to:

$$I_c \approx \beta \cdot I_b \tag{6.1}$$

where β is the current amplification factor of the transistor. The dash-dotted line r is the loading curve of the BJT, representing the allowed operating points, while dotted ones show the I_c, V_{ce} characteristic of the transistor as a function with parametric I_b.. The load can be either directly connected to the amplifier circuitry or decoupled by means of an output transformer.

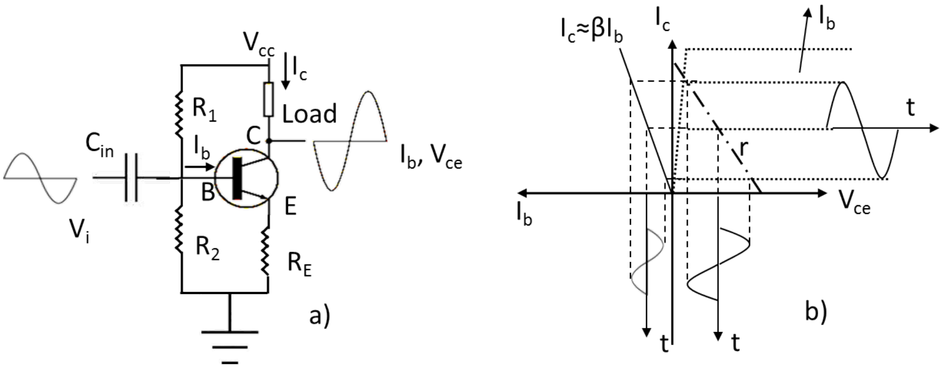

FIGURE 6.1: Example of an elementary A class amplifier based on an NPN BJT (Base Junction Transistor). a): electrical scheme. b): graphic representation of transistor functioning. The letters C, B, E are referred to the collector, base and emitter of the transistor respectively. V_{cc} is the DC feeding voltage, while the resistances R_1, R_2 and R_E provide the required polarization of the BJT. The capacitor C_{in} acts as an high-pass filter, on order to block useless DC components of the input. V_{ce} is the collector-emitter voltage of the BJT, which varies with I_c.

The broad definition of an amplifier can be further refined by focusing on the output physical quantity of interest, thus distinguishing between (i) *voltage amplifiers*, (ii) *current amplifiers* and (iii) *power amplifiers*. In general the first two types are employed as the first stages of an amplification system (pre-amplification or driver stages), which drive a final power amplification stage.

Power amplifiers must theoretically meet three key requirements, namely (i) high output power P_{out}, (ii) high efficiency, defined as the ratio $\eta_a = P_{out}/P_{in}$ between the output and input power, and (iii) low distortion of the signal waveform. These three aspects are in conflict between each other, leading to compromise solutions aimed at optimizing one of them at the expense of the others. These solutions are identified by various power amplifier classes [34], based on the *conduction angle* Θ of the non-linear element of the amplfier, defined on the basis of the time t during which, during a period T of the AC signal to be amplified, current flows through the element:

$$2\Theta = 360^\circ \cdot t/T \tag{6.2}$$

The value of Θ depends on the circuital solutions adopted in the amplifier and can be varied in order to meet one of the three requirements for power amplifier listed above. According to the definition of eq.6.2, four main classes of amplifiers can be identified:

- class A, where Θ=180°;
- class AB, where $90^\circ \leq \Theta \leq 180^\circ$;
- class B, where Θ=90°;

- class C, where Θ¡90°;

Classes from A to B are also defined as *linear amplifiers*, since they minimize the distortion of the signal at the expense of efficiency; in class A, in particular, current flows through the nonlinear elements for the entire length of the period, in order to mantain them in their linear operation region [35]. Figure[6.2] shows an example of this operation principle for a BJT amplifier: the polarization of the BJT is such that, with no input signal, the current I_b rests at a non-zero value, correspondent to approximately half of the load curve r. In these conditions the transistor is always in conduction and is capable of linearly amplifying both positive and negative variations of I_b, according to its β factor, with theoretically null distortion. This, however, also means that power is dissipated in the nonlinear element for the whole duration of T, resulting in a maximum theoretical efficiency η_a= 25% for the pure A class amplifier and of 50% with an output transformer [34]. It must be pointed out that the polarization circuit is designed for a specific load impedance, defined as the output impedance of the device. If the latter is connected to a load having a different impedance value, its nonlinear elements will receive an incorrect polarization and the overall efficiency will be lower than the theoretical maximum value.

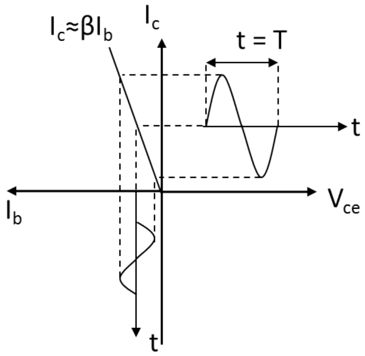

FIGURE 6.2: Graphical analysis of A class functioning for a BJT amplifier.

Class B amplifiers, on the other hand, represent an attempt at achieving a better efficiency while retaining a good linearity; this is achieved by means of the operating principle shown in Figure[6.3]: in this case the transistor is polarized in order to have I_b=0 in absence of an input signal, meaning that the transistor will allow the passage of I_c during just 1/2 of the period, while it will be in interdiction during the other half. The amplification is still linear, but with a pulsed output, requiring two amplification circuits, connected in a counter-phase (push-pull), to reconstruct the complete input waveform. The maximum theoretical efficiency, on the other hand, increases dramatically, since now current flows through the transistor, with consequent power dissipation, only for $T/2$, resulting in $\eta_{a,max} \approx 78\%$ [34]. The same limitations of class A with respect to load impedance apply for class B.

Class B transformers, in fact, are affected by a greater distortion than class A ones, since real transistors require a certain input voltage threshold to enter in conduction, resulting in the so called *crossover distortion.* Class AB amplifiers were created in order to overcome this issue, adopting a class B functioning with a small but non-zero I_b is maintained in zero input conditions. This current is small enough to keep the diode in conduction, while limiting the power dissipation with respect to a pure A class amplifier. The resulting efficiency is intermediate between classes A and B [34].

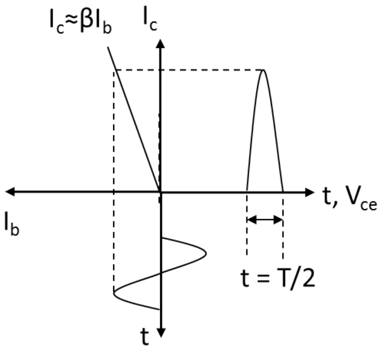

FIGURE 6.3: Graphical analysis of B class functioning for a BJT amplifier.

The last main class of amplifiers, class C, (Figure[6.4]), can achieve even higher efficiencies (theoretically up to 100%), since in this case the power absorption takes place for a time smaller than one half-period, but the output waveform, which is pulsed as in the case of B class amplifiers, is characterized by a relatively high distortion, which grows as the conduction angle becomes small. Efficiency, however, grows as well. Push-pull configuration is possible as in the case of class B. Again, the load impedance must match the design value.

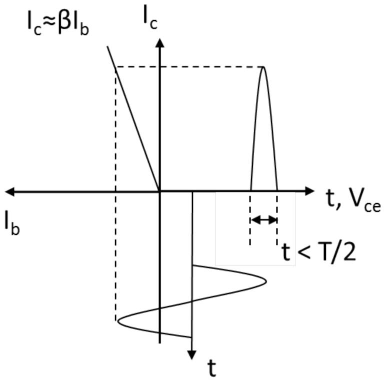

FIGURE 6.4: Graphical analysis of C class functioning for a BJT amplifier.

More recent developments of amplifier technology include switching devices, in which the nonlinear elements are polarized either completely on (i.e. in saturation regime) or completely off. The working regimes of these devices can be re-conduced to the three main classes identified above [36], but with a greater efficiency with respect to traditional amplifiers in the same operating conditions, since when in saturation the nonlinear elements have a negligible resistance, meaning that they dissipate a very small fraction of the power absorbed from the supply. The theoretical efficiency can be as high as 100% for some configurations, only limited by the small but non-zero resistance of nonlinear devices in conduction and by the non perfectly square waveforms which are practically achievable.

Switching amplifiers are grouped in additional operating classes (D,E,F,G,H) among which class E (Figure[6.5]) is of particular interest for our application; these amplifiers can be considered a sort of switching variant of class C, capable of high efficiency operation at frequencies nearing the duty cycle of the employed nonlinear elements: indeed in this case high efficiency is achieved by adopting the following strategy:

- the voltage across the nonlinear element is maximum during its OFF (interdiction) state, and ideally zero during its ON (conduction) state;
- the voltage across the nonlinear element must reach zero with zero slope (dV/dt = 0) so that the current flowing in the element is zero at the beginning of the ON state;
- the rise of the voltage at the end of the ON phase must be delayed (usually by means of a capacitor) until the OFF condition is reached.

All these conditions are conceived in order to avoid the contemporary presence of large voltages and currents across the nonlinear element, thus minimizing in each condition the $V \cdot I$ product and thus the dissipated power.

A sine-wave output is provided to the load by means of a series LC filter connected between the amplifier circuit and the load.

Class E amplifiers are potentially capable of MHz-range operation with high efficiency (≥ 90 %), making them the most promising candidates for the use in the HPT PPU.

6.1.2 Intermediate power prototype

The power amplifiers available in the existing set-up (see 2.1.2) are of commercial origin and originally intended for generic industrial or radio applications; for this reason they belong to class A or AB and are characterized by a standard design output impedance of

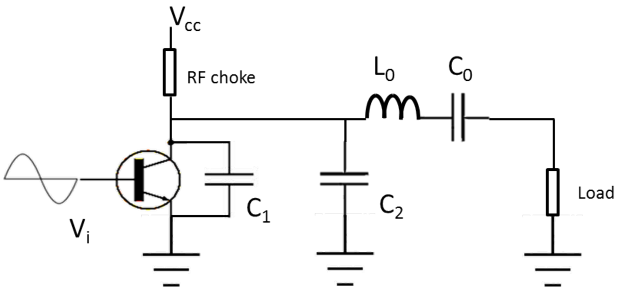

Figure 6.5: Basic scheme of a class E amplifier. The power supply providing the feeding voltage V_{cc} is protected from RF interference by an RF choke. C_1 is the parasitic capacitance of the transistor, C_2 is a shunt capacitance for high order harmonics, L_0 and C_0 are the components of a resonant circuit acting as a narrow-band pass filter, tuned at the operating frequency.

50 Ω, matching the characteristic impedance of standard cables and communication antennae constituting their intended load. These two limitations make them ill-suited for the execution of the intended high power multi-propellant characterization and optimization tests, since in this case (i) the load impedance will probably experience significant variations and (ii) their low efficiency limits the maximum power which can be applied to the thruster and, in perspective, makes them unsuitable for in-space operation.

The solution to these problems, developed in cooperation with RESIA, was found adopting a push-pull class E configuration, calibrated in order to achieve the lowest possible output impedance (a few ohms). The load, constituted by the antenna, is usually characterized by an impedance which varies within a relatively wide range (typically Z_A = 50-2000 Ω), but this value is transferred to the amplfier circuitry by means of an output transformer, thanks to which the impedance effectively seen by the amplifier becomes $Z_e = Z_a \cdot n_1/n_2$, with n_1/n_2 the winding ratio of the transformer ($n_1 \ll n_2$). This ensures that the impact of load variations on the polarization circuit becomes minimal, ensuring high efficiency operation in a broad range of operating conditions.

This solution was implemented by RESIA through the two-stage architecture shown in Figure[6.6]: a first stage, based on two branches of BJTs connected in push-pull [34], drives the power section, based on two push-pull branches of IRF540 MOSFETs, characterized by a maximum current rating of 10 A per transistor. The latter are connected to an output transformer, which can be easily replaced in order to achieve the desired output voltage level. The driver output voltage is asymmetrical (+12 V / -4 V) in order to shorten the commutation time of the MOSFETs. Output frequency adjustment is possible by changing clock frequency. The supply voltage can be comprised between 20-30 V DC, for a maximum output power of ≈ 480 W. kW-level output can be achieved by substituting the MOSFETs with other ones having an higher maximum current rating. The driver section includes logical circuitry for dead-band control, ensuring that the two branches of the push-pull are never in contemporaneous conduction, with potentially destructive effects. The operating frequency can reach a maximum of 2 MHz.

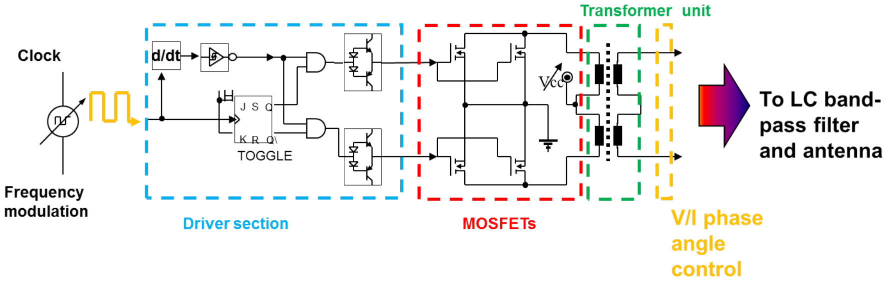

FIGURE 6.6: Basic scheme of the high efficiency RF amplifier developed with RESIA. The system is conceived in order to operate in frequency tuning mode.

It was decided to develop from the beginning constructive solutions aimed at enabling in-vacuum and space-based operation, in the perspective of realizing a full scale HPT prototype complete with its own PPU:

- thermal control is managed by means of completely passive solutions, allowing to collect the waste heat to the external surface of the PPU box, which then radiates it;
- all components have been chosen among models for which a space-qualified version is readily available.

The prototype RF amplifer can be seen in Figure[6.7], which evidences its two-stages architecture. The lateral aluminum bars, acting as radiators and structural elements, can also be noticed. Additional heat dissipators were attached to the driver section, which is responsible for the biggest part of the dissipated power.

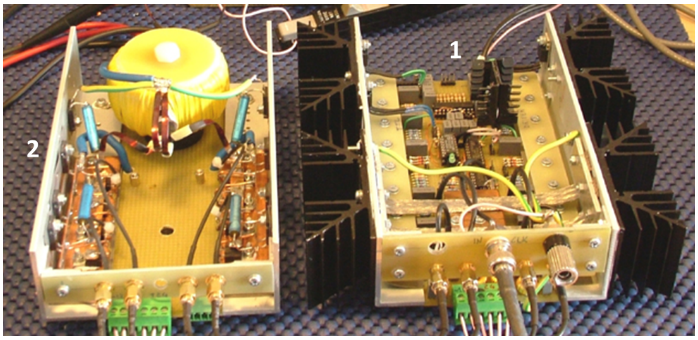

FIGURE 6.7: The prototype RF amplifier. 1) driver stage. 2) power stage.

As a final remark, it is interesting to point out that the amplifier was designed in order to be compatible also with DC thrusters, such as Hall effect ones: in this case the driver and power sections remain the same, but function with a fixed frequency, while the output power is regulated via PWM control. The thruster is fed through an AC/DC converter, in lieu of the LC filter employed for HPTs.

Such high flexibility, combined with an high efficiency, make this amplifier a truly innovative realization in the field of power generation systems for electric space thrusters.

6.1.3 Preliminary testing

The prototype was subject to preliminary testing at a power level below 200 W by RESIA and CISAS personnel, in order to check the correct functioning of all its components. The tests were performed in the 500 kHz - 2 MHz frequency range, employing an high power variable resistor ($R_{max} = 1$ kΩ) as a dummy load. Power was supplied by an HP6002A DC supply (P_{max} 200 W). The following tests were performed:

- measurement of the driver section output, with particular attention to dead-band control and voltage waveform;
- measurement of the power section output and current, in order to verify the effective output power and waveforms;
- monitoration of the input voltage and current provided by the DC power supply.

AC voltages and currents were probed by means of an oscilloscope, while the DC power feeding was monitored employing the output voltage and current indicators of the power supply. The waveform of the driver section can be seen in Figure[6.8]: the transistors are in conduction during Ton and in interdiction during Toff. It can be seen that Ton l Toff, ensuring that the simultaneous conduction of the two branches of the push-pull never occurs. The asymmetrical +12 V / -4 V output voltage was chosen to ensure high-speed MOSFET commutation. No significant waveform distortion was detected up to 2 MHz.

An example of power stage output is reported in Figure[6.9]: within the investigated frequency range the efficiency of the amplifier, measured as the ratio between the output and input power, resulted to be always above 80%.

Preliminary in-vacuum testing was also performed by placing the prototype amplifier inside CISAS vacuum chamber (2), where a pressure level of $\approx 1{\cdot}10^{-5}\ pm$ 30% mbar was mantained. The power section was connected to a dummy resistive load of 200 Ω and operated up to a power of 200 W. The amplifier temperature was monitored by means of an externally placed infrared camera through an IR-transparent observation port. The results, shown in Figure[6.10] although preliminary, showed that, in the explored conditions, the heating of the active components (MOSFETs, BJTs) and of integrated logics is effectively distributed to the external structure of the power section, resulting in a very uniform temperature profile and in a very limited heating (10-14 K in steady-state conditions). In all these tests confirmed the capability of the prototype to operate at MHz - level frequency with high efficiency.

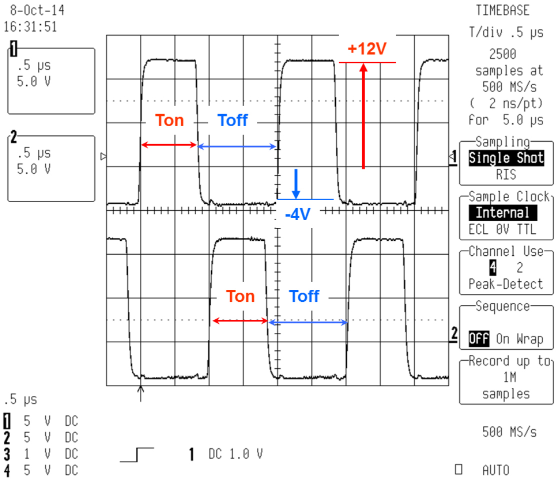

FIGURE 6.8: Driver section output voltage at 500 kHz. The transistors are in conduction during Ton and in interdiction during Toff. It can be seen that Ton l Toff, ensuring that the simultaneous conduction of the two branches of the push-pull never occurs. The asymmetrical +12 V / -4 V output voltage was chosen to ensure high-speed MOSFET commutation.

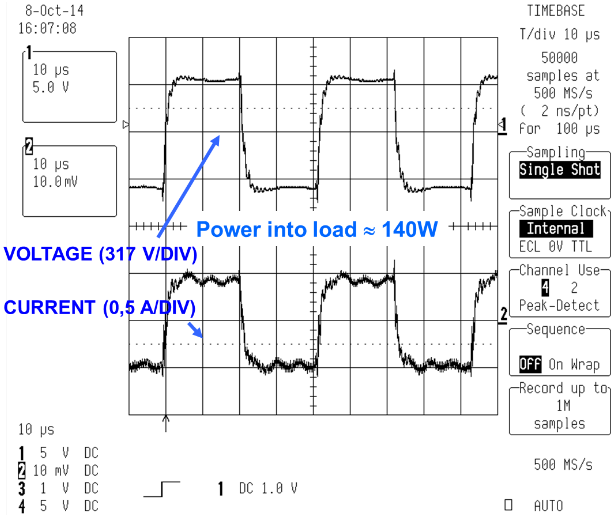

FIGURE 6.9: Power section output voltage (upper signal) and current (lower current) at 500 kHz, measured with a dummy load of 760 Ω. The scale is 317 V/div for voltage and 0.5 A/div for current. The corresponding output power is ≈ 140 W, against an input power from the DC supply of 170 W, for an efficiency of ≈ 80%.

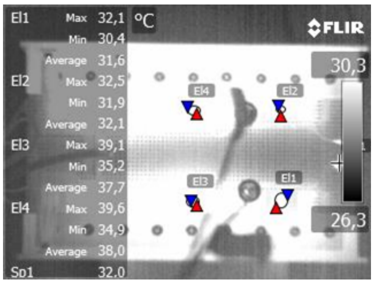

Figure 6.10: Thermal imaging of the power section during in-vacuum testing. Dark surfaces are at low temperature, while light ones are hotter. The high uniformity of temperature across the surface of the device evidences the effectiveness of the thermal dissipation system. The increase in temperature during operation at 100-200 W was estimated to be around 10-14 K in steady state operation (ambient temperature is around 26 ◦C.

6.2 Impedance matching system

6.2.1 Conceptual design

As stated in 3 the presence of the plasma can be seen, under the electrical point of view, as the introduction of additional resistive and reactive elements to the equivalent circuit of the antenna. This implies that, at a given operating frequency, the antenna will experience both a variation of its impedance modulus and of its phase angle, introducing the need of some sort of matching circuitry with variable reactive elements in order to actively (i) eliminate the reactive part of the load impedance, in order to avoid power reflections and (ii) match the output impedance value of the RF amplifier .
In the present case the matching requirements are less stringent, since the RF amplifier can handle loads with variable impedance without significant efficiency decrease in a broad range of values (see 6.1.2), but the elimination of reactive components remains critical. The solution devised in order to solve this issue is based on:

- a matching network, composed of fixed discrete capacitors;
- an automatic frequency adjsutment system.

The first element provides a coarse matching by making the load seen by the amplifier resonant at a given frequency, in correspondence of which its impedance is purely resistive; this first adjustment is performed without the plasma and provides the "reference" condition around which the antenna will work in the presence of the plasma. The second element must provide a fine matching by tuning the operating frequency: indeed the load, constituted by the matching capacitor, the antenna and the plasma, still resonates, although at a different frequency. The first derivative of the phase angle with respect to frequency has a monotonic trend around resonance, meaning that the imaginary part of impedance can be zeroed by frequency adjustment, resulting in a relatively simple system with respect to matching networks based on mechanically variable reactive elements. This feedback control philosophy is known as Phase-Locked Loop (PLL), and is exemplified in Figure[6.11]: the operating frequency of the RF amplifier is determined by a Voltage-Controlled Oscillator (VCO), basically an external clock whose output frequency is determined by an externally fed control voltage; the latter is produced by a phase detector, which measures the phase angle between the voltage and current flowing in the load, generating a proportional error signal. The authority and stability of the control loop are determined by the combination of an error amplifier and a low-pass filter, acting as a "damper" avoiding excessively violent corrections which may generate instabilities.

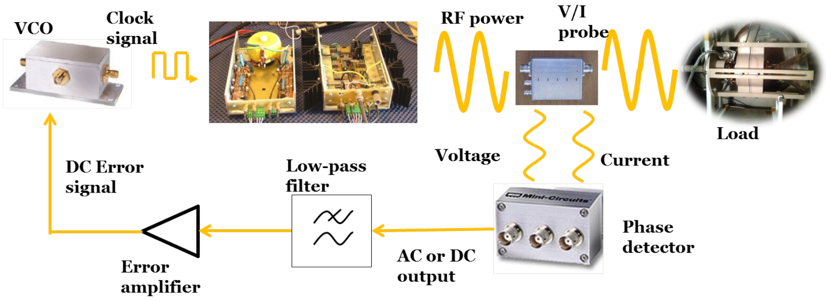

FIGURE 6.11: Basic scheme of the proposed Phase-Locked Loop.

6.2.2 Preliminary design

The preliminary design of the matching system was performed with the help of a Simulink lumped parameters model, which enabled the evaluation of the devised solutions by means of time-domain simulations. The overall model is portrayed in Figure[6.14]: the resonant system composed by the antenna, the plasma and the matching capacitors is represented by an equivalent dummy resonant load. The latter is fed by a power generation block (Figure[6.15]), consisting of a VCO connected to a simplified half-wave switching amplifier, producing a square-wave output which is representative of the output of the real amplifier in terms of harmonic content. The output frequency from the VCO ($f0$ in the figure) is decreased by means of a frequency divider, based on a cascade of n J-K flip-flops, so that the final frequency is $f1{=}f0/2^n$. This element is necessary since most commercially-available VCOs are characterized by operating frequency ranges well above the maximum value of 2 MHz allowed by the amplifier. In preliminary simulations the VCO was modeled on the base of the MiniCircuits ZOS-75, which is already available at RESIA, characterized by a frequency span between 37.5-75 MHz, corresponding to an input voltage span of 0-16 V (sensitivity ≈2,34 MHz/V), coupled with an 1:32 frequency divider (1.17 - 2.34 MHz output). The center frequency of the VCO is 56.25 MHz (8 V input), which become 1.76 MHz after frequency division: it was decided to adopt this frequency as the"rest" condition of the system (no plasma). The power generation block is connected to the dummy load through an LC band-pass filter; this element was inserted in the model in order to study its interaction with the load and the frequency adjustment system. The filter was centered on the "rest" frequency of 1.76 MHz, by choosing a capacitance of 8.2 pF and an inductance of 1000 μH. These values ensure the proper shaping of the sine-wave applied to the load, while allowing the variation of the operating frequency around the rest value within the variation range granted by the VCO.

Feedback control is provided by a phase detection system, which receives as an input the measured voltage and current flowing in the load and produces an output DC error signal which is fed to the VCO, in order to tune its frequency to the resonant frequency of the load. This system was preliminarily designed as illustrated in Figure[6.16]: the measured sine-wave voltage and current are turned into square pulses by means of J-K flip-flops and then fed to an XOR gate, which produces a pulsed output whose mean value within an RF period is proportional to the phase difference between the two signals (Figure[6.12]). A similar solution is employed in order to determine the sign of the phase angle, which is necessary in order to determine if the operating frequency has to be increased or decreased: an additional J-K flip-flop, triggered by voltage (the trigger is on for with a positive rising voltage), receives the output of the XOR gate on its J port and a null voltage on its K port. The default value of the outputs Q and $\overline{Q}$ are set at 0 and 1 respectively. The working principle of this solution can be seen in Figure[6.13]: if the pulsed signal produced by a non-zero phase angle is positive when the flip-flop is triggered (rising voltage) the current is anticipating the voltage and the output ports of the flip-flop assume the constant values of 1 and 0 respectively; if, on the other hand, the voltage is anticipating the current then the pulsed error signal is positive when the voltage is decreasing, meaning that the output ports of the flip-flop will retain the default values of 0 and 1 respectively. This means that the sign of the phase angle can be expressed by means of an 1-bit digital signal which, in the real system, will become a DC voltage, either null or positive.

The pulsed output of the XOR gate is fed to an integrator circuit based on an operational amplifier, which acts both as a low-pass filter and as an error amplifier for the feedback control loop. This was achieved by connecting the inverting input of the operational amplifier to its output by means of a relatively large (2.5 nF) capacitor in parallel with a 400 kΩ resistance, while all other resistances in the circuit have a value of 2.2 kΩ. This ensures both an high gain, required for effective phase angle nulling, and a strong damping effect, necessary to avoid excessively violent corrections which may

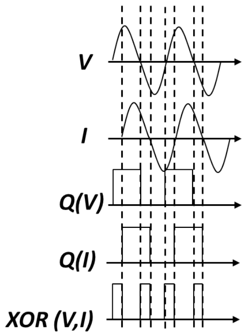

FIGURE 6.12: Signal processing for phase angle detection.

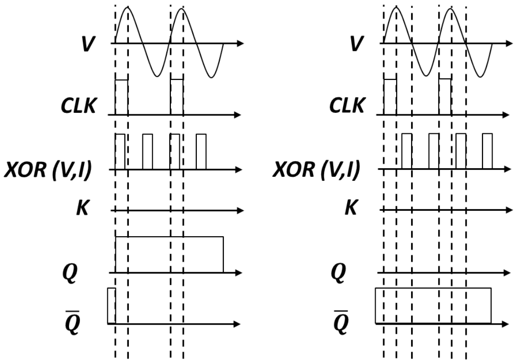

FIGURE 6.13: Phase angle sign determination. Left: current anticipating voltage. Right: voltage anticipating current.

bring the system in unstable conditions. The result is an amplified DC error signal, which is then summed to and subtracted from the "rest" voltage Vcc = 8 V by means of a chain of inverting amplifiers with unitary gain, based on operational amplifiers. A switch, controlled by the sign of the phase angle, selects one of the two resulting control voltages, which is then applied directly to the VCO. The validity of this solution was tested by means of time domain simulations, in which the electrical parameters of the dummy load were set in order to resonate at a slightly different frequency with respect to the "rest" one, thus simulating the variation of antenna reactance generated by the plasma: in particular the load inductance L_l was set at 12 μH and the load capacitance at 820 pF, resulting in a resonant frequency $f_{r,l} = 1/(2\pi\sqrt{L_l C_l}) \approx 1.6$ MHz. In a first test the feedback loop was not enabled, feeding the VCO with just the "rest" 8 V voltage, with the results reported in Figure[6.17], evidencing that at the "rest" frequency the load presents a non negligible reactance, resulting in a ≈27° phase angle. As expected the phase detector correctly produces a negative error voltage, which, when summed to the "rest" 8 V DC voltage, will reduce the output frequency of the VCO from the default value of 1.76 MHz. In a second test the full feedback loop was enabled, achieving the results shown in Figure[6.18]: the control system demonstrated its ability to effectively compensate the reactance of the load, by reducing the phase angle to approximately 5°, which, from a practical point of view, can be considered sufficiently small. The control has, with respect to the time scale of the simulation, a sensible inertia, given by the very large damping, which on the other hand ensures the required stability. Preliminary testing has thus far confirmed the validity of the adopted matching solution, which is scheduled for manufacturing during next year.

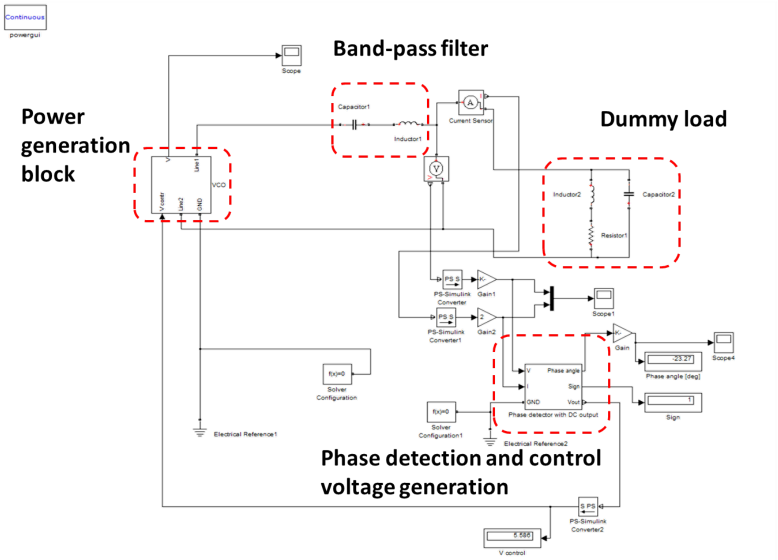

FIGURE 6.14: Overall layout of the impedance matching system. The system constituted by the antenna and the capacitive matching network is represented by an equivalent inductive - capacitive resonant network.

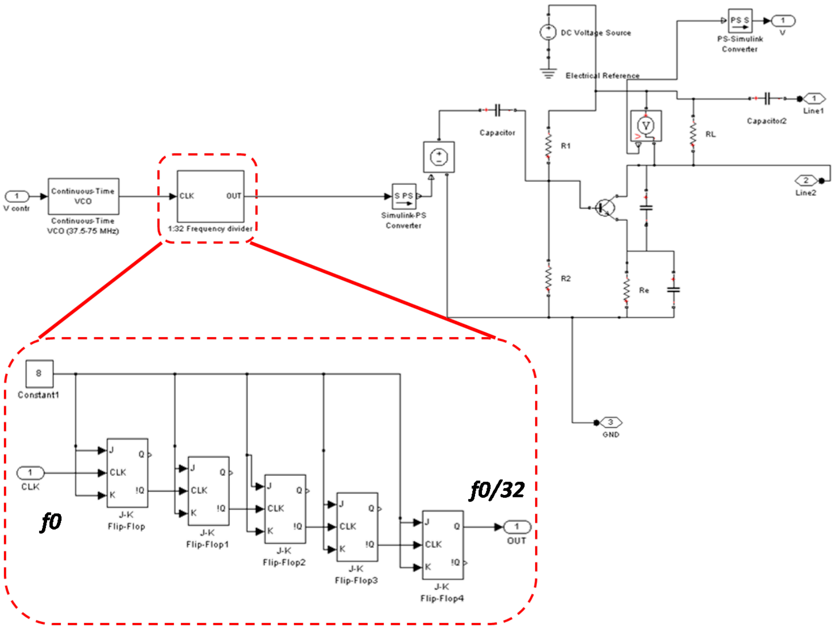

FIGURE 6.15: Scheme of the power generation block. A VCO drives a simplified, half-wave switching amplifier through a frequency division network.

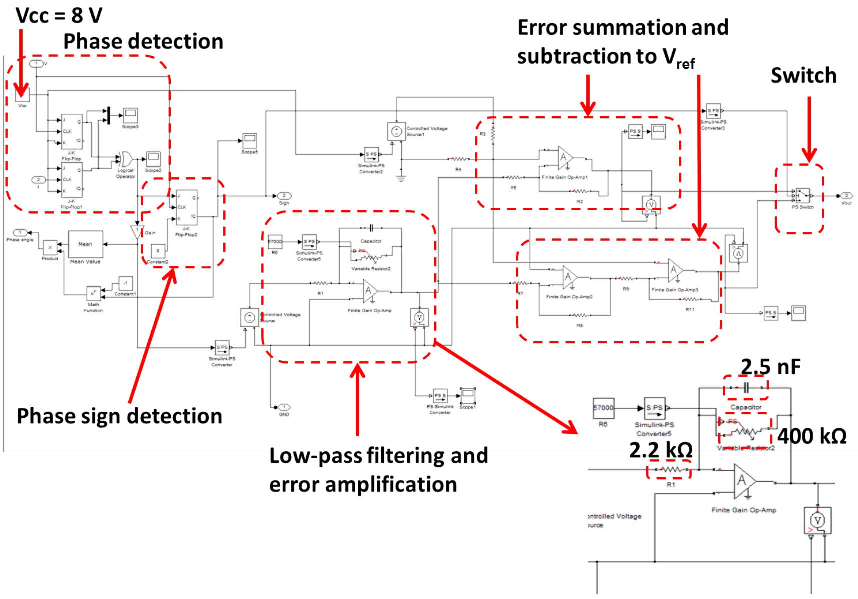

FIGURE 6.16: Phase detection and error signal generation circuit.

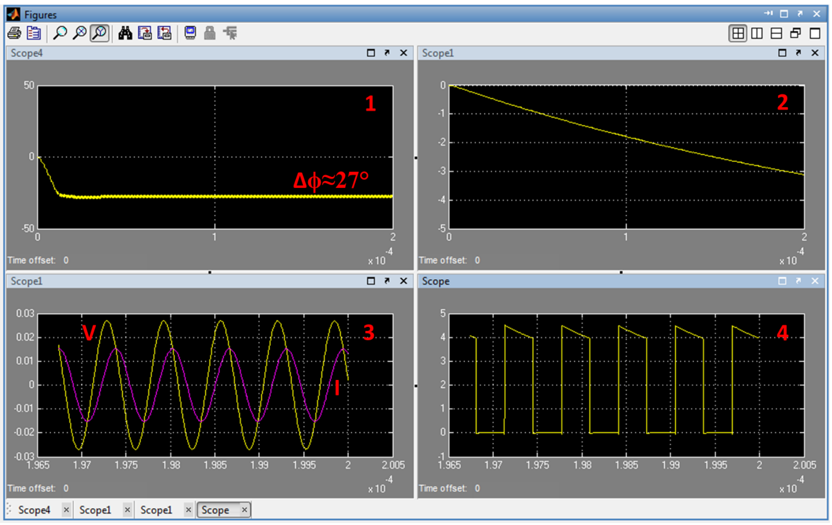

FIGURE 6.17: Simulation without frequency tuning. 1) phase angle [deg]. 2) error signal [V] . 3) load voltage and current [V · 100 , A /2]. 4) power generation block output [V].

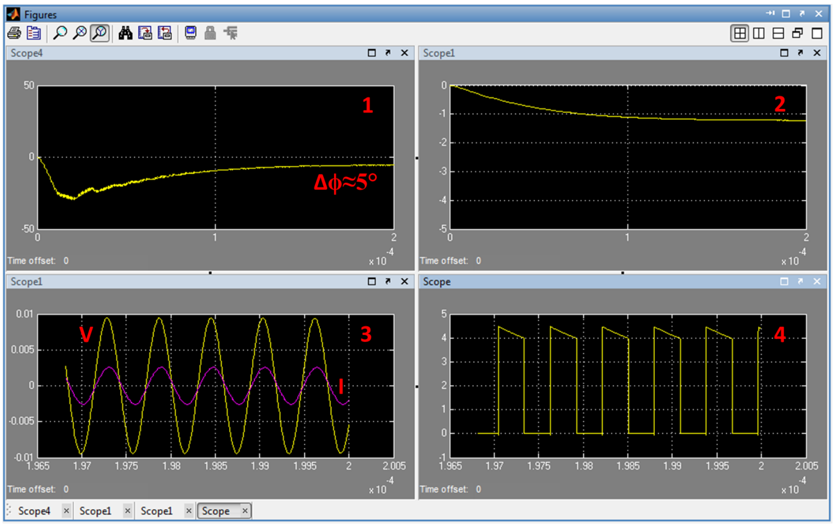

FIGURE 6.18: Simulation with frequency tuning. 1) phase angle [deg]. 2) error signal [V] . 3) load voltage and current [V · 100 , A /2]. 4) power generation block output [V].

Chapter 7

Conclusions

The completion of a fully operational high power, multi-propellant test-bed at CISAS propulsion laboratory is at an advanced stage of completion: the full system could not be assembled and tested within the end of this PhD, due to schedule issues, but all its components have already been designed and most have been manufactured. This was achieved through several key objectives, reached within this PhD activity: the analysis and design of the RF network, which constitutes the heart of the thruster itself, can now be carried out by means of the numerical tools and solutions illustrated in 3, while the combined experimental/numerical study reported in 4 led to the identification of electrical and geometrical optimization solutions, tested on the low power HPH.COM laboratory model, to be implemented in the high power design. High power, multi-propellant operation issues were explored with the test campaign reported in 5, whose results allowed to conclude that the power scaling of HPT technology and its adaption to different propellants does not present critical issues. All these results enabled the design and development of an high power plasma source, described in the same chapter, whose manufacturing is currently ongoing and is scheduled for completion within the beginning of 2015. The RF power generation system is at an high completion stage as well: the switching RF amplifier intended for high power operation was developed and tested as described in 6 and represents a substantial improvement over commonly available solutions based on linear amplifiers and can potentially be developed in a space-qualified system with relative ease. The same holds for the relatively simple matching system devised for operation with such amplifier, whose basic design was performed by means of numerical simulations. Such system was not yet manufactured due to the higher priority given to the RF amplifier, which represents the truly innovative part of the power generation system, but is scheduled for completion within 2015. The development of the high power, multi-propellant test bed will be completed by the author, which will continue its collaboration with CISAS after the end of his PhD.

Appendix A

Faraday probe focusing correction

In order to estimate the focusing effect of the Faraday probe a simplified approach was developed, in which the effect of probe potential on the trajectories of incoming ions is estimated in order to calculate the effective collection area of the probe. This was implemented in a dedicated Matlab® script, which is thus structured:

- the vector electrical field **E** induced by the probe in its surroundings is first determined by means of an electrostatic FEM solver. Since both the probe and the plasma plume it is immersed in exhibit an axisymmetric structure, the simulation is carried out in a 2D domain;
- the effect of Debye shielding [8] is neglected, assuming a sufficiently low plasma density in the measurement region and thus a large enough distance between the probe and the thruster;
- a set of ions is generated at a certain distance from the probe, spaced along the radius of the system. The ions are assumed to be all heading towards the probe with a purely axial trajectory and with the same speed, again an hypothesis holding when the probe is placed sufficiently far from the thruster;
- the equations of motion of the ions are integrated in a selected time span, considering the focrce experienced by the particles due to the electric field generated by the probe. Other forces, such as gravity or the electrostatic repulsion between ions, were considered negligible with respect to the electrostatic attraction/repulsion exerted by the probe;
- the integrated ion trajectories are followed in order to estimate which ones actually impact the collector plate. This leads to the estimation of the focusing effect

$fe = A_{p,eff}/A_{p,geom}$, where $A_{p,eff}$ is the effective probe collection area and $A_{p,geom}$ is the geometric area of the collector.

The hypothesis on the negligibility of Debye shielding is particularly critical: it means that the electrostatic shielding phenomenon due to charge re-configuration in the plasma must not interfere with the probe collection area, that is, with reference to Figure[A.1], it must act on a distance $\lambda_D \geq r_d$, where the latter is the distance from the probe at which a particle becomes sensibly deflected by the voltage bias of the collector plate. The value of R_D depends on the operating conditions and in the case of a 50 W HPT employing on Argon it was estimated around $0.5r_p$, with r_p the radius of the collector plate. This assumption may hold when the probe is relatively far from the thruster, in order to have a sufficiently low plasma density in the measurement region

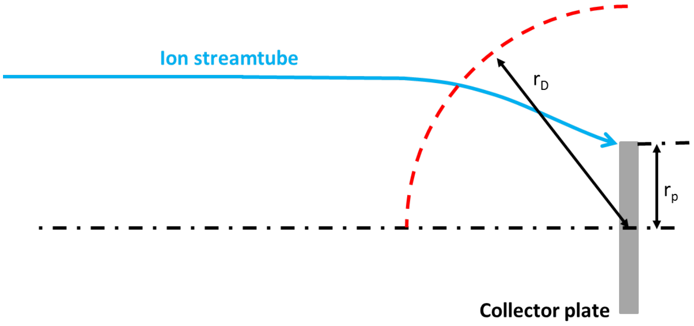

FIGURE A.1: Ion electrostatic focusing. The distance r$_D$ is the Debye length.

Electrical field calculation

This task is carried out by means of the free-ware software FEMM [22], a suite of programs dedicated to the solution of low-frequency electromagnetic problems on two-dimensional planar and axisymmetric domains. FEMM can interact with Matlab® or Octave by means of a dedicated Lua command set.

For the present application the probe was modeled as in a 2D axisymmetric problem as a thin plate encased in an hollow cylinder, representing the guard ring (see Figure[A.2]); the simulation domain is a sphere is centered on the center of the probe and its radius is chosen in order to be a least an order of magnitude larger than the probe radius, in order to allow the use of an explicit Dirichlet condition $V = 0$ on the sphere boundary. All the domains are modeled as air domains, since the relative permittivity of metals can be modeled as unitary, while the boundaries of the probe plate and guard ring were set as conductors with a prescribed voltage V_p and $V_g = 0V$ respectively. The size of the triangular mesh elements was chosen after a sensitivity analysis in which it was progressively reduced until no detectable variations on the solution were achieved. In order to reduce the computational time the mesh was divided into two sub-regions, a more refined inner one and a coarser external one.

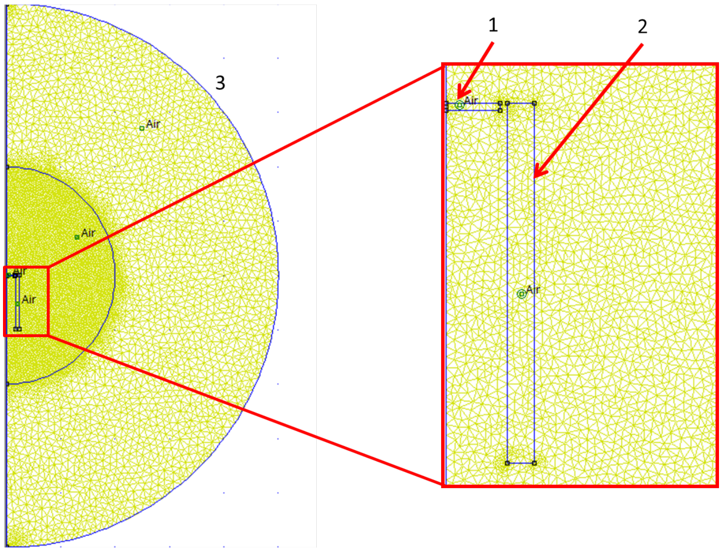

FIGURE A.2: FEMM model of CISAS Faraday probe, showing also the mesh (note the two sub-regions with different mesh refining). The diameter of the probe (1) is 3 mm, while the diameter of the spherical domain (3) is 400 mm. The guard ring (2) is also displayed.

The resulting electrical field is read by the Matlab® script in a specified region, discretized by a n_r byn_z matrix of points, and imported as two matrices, E_r and E_z, containing the radial and axial field components respectively.

Ion trajectory integration

Ions are generated at an arbitrary axial distance d=-15 mm from the plate, which is centered on the $[0;0]$ position of the simulation domain, and are aligned on the radial direction with a spacing δr chosen in order to ensure the desired resolution in the effective collection radius estimation, which is usually set at 0.05 mmx. Each particle is thus created with the following initial conditions vector, $X_{0,i}$:

$$X_{0,i} = \begin{bmatrix} d \\ r_i \\ v_{z,0} \\ 0 \end{bmatrix}$$

Here the subscripts z and r refer to the axial and radial directions respectively, while i indicates the i-th particle. The initial radial position of each particle, r_i, is calculated starting from a chosen radius, usually equal to $p_d/4$, where p_d is the diameter of the

collection plate, such that $r_i = p_d/4 + \delta r \cdot i$. This avoids to generate unnecessary particles that are useless for the collection radius determination. The number of particles is chosen in order to cover a radial extension sufficent to include the effective capture radius of the probe and must be determined by trial and error. The initial axial velocity of all particles is $v_{z,0} = \sqrt{2 \cdot q_i \cdot E_i / m_i}$, where E_i is the ion kinetic energy expressed in eV, q_i is the ion elementary charge and m_i is ion mass.
the equation of motion of the single particle are expressed as follows:

$$eq(X,t) = \begin{bmatrix} \dot{X}_1 \\ \dot{X}_2 \\ 1/m_i \cdot q_i \cdot E_z(X) \\ 1/m_i \cdot q_i \cdot E_r(X) \end{bmatrix}$$

where the axial and radial components of $\mathbf{E}$ are interpolated as a function of particle position. $X = [\dot{z}; \dot{r}; z; r]$ is the unknown vector. The equations of motion are integrated for each particle by means of the ode45 Matlab® function, in a time span chosen in order to avoid the exit of the particles from the simulation domain.

Focusing effect estimation

The trajectory of each particle is followed in order to determine if it impacts the collector plate, starting from the inner particle generation radius. If the i-th particle impacts the collector the effective collection radius of the probeis set equal to the initial radial position of the particle, $r_{p,eff} = r0_i$, corresponding to the radius of the particle stream tube coming from the unperturbed region whose external edge is marked by the i-th particle. As all the trajectories are scanned $r_{p,eff}$ progressively rises until no more impacts are detected; in this condition the maximum radius of the stream tube captured by the probe has been found and the effective collection area can be calculated as $A_{p,eff} = \pi \cdot r_{p,eff}^2$. The determination of the focusing factor is then straightforward: $fe = A_{p,eff}/A_{p,geom}$. The value of fe can then be employed to correct the experimentally detected current as follows:

$$I_{corr} = I_{exp}/fe \tag{A.1}$$

where I_{corr} is the estimated real current and I_{exp} si the experimentally measured one. An example of the output of the program is shown in Figure[A.3].

uncertainty estimation

	E_i=80 eV	E_i=100 eV	E_i=120 eV
fe	1.87	1.69	1.6

TABLE A.1: Variation of the focusing factor as a function of the mean ion energy for a probe voltage of -150 V. A ± 20 % variation of E_i produces a ± 8 % variation in f_e.

The uncertainty associated with the estimation of f_e, ϵ_{focus}, is affected by many factors:

- probe polarization uncertainty;
- mean ion energy uncertainty;
- Debye shielding uncertainty.

The polarization of the probe is known within ± 0.1 V and has a negligible impact on the overall uncertainty. The effective ion energy could not be directly measured within this work, due to the unavailability of the related diagnostic (the Retarding Potential Analyzer, see [3] for further details). Instead, since the Faraday probe was employed on the Argon-fed low power HPT model developed during program HPH.COM, it was assumed that the mean ion energy lies within the range detected during such program, spanning from 80 eV to 120 eV ([3, 13, 14]). For this reason it was decided to calculate f_e for E_i= 100 ± 20 eV, resulting in a variation of f_e due to this effect equal to $d_{f_e,Ei} \approx$ 8.5%, as it can be appreciated from Table[A.1].

Debye shielding effectiveness is more difficult to estimate with respect to other uncertainty factors: if the probe is placed sufficiently far from the thruster the plasma density will be sufficiently low to avoid shielding at all, but in the CISAS set-up, due to geometrical constraints, the probe must pe placed relatively close to the thruster exit plane, where Debye shielding effects may not be negligible. The accurate estimation of this effect would require a plasma density map of thruster plume, which represents an overcomplication under the experimental point of view. For this reason it was decided that, in cases where the probe is placed relatively near to the thruster, the uncertainty due to Debye shielding can only be broadly estimated according to the following process:

- the real focusing coefficient is considered to be between two extreme values, a maximum fe_{max} and a minimum fe_{min};
- fe_{max} is the value calculated without considering Debye shielding, meaning that the incoming particles are fully exposed to the focusing potential of the probe;
- fe_{min} is considered equal to 1, meaning that it refers to a situation in which Debye shielding is perfect and the probe voltage does not generate an appreciable focusing effect.

With such assumptions the overall uncertainty on fe becomes $\delta fe = \pm \left(fe_{max} - fe_{min}\right)/2$, referred to a mean value $fe_{mean} = \left(fe_{max} + fe_{min}\right)/2$. Of course the higher is the probe voltage, the higher will be δfe. For example a bias of -150 V, with a typical mean ion energy of 100 eV, results in $fe_{max} \approx 1.7$, $fe_{mean} \approx 1.35$ and $\delta fe \approx \pm 0.35$ ($d_{f_e,shield} \pm$ 26 % relative error). In general thanks to Debye shielding the real value of fe will be lower to the calculated one, meaning that the current is always underestimated. This provides a certain safety margin, since, if the ion current calculated in the worst case hypothesis ($fe = fe_{max}$) increases, the real value of the current will increase as well and will be equal to or higher in absolute terms with respect to the estimated one. The uncertainty related to the estimation of f_e can be performed as:

$$\epsilon_{focus} = \pm\sqrt{\left(d_{Ei}\right)^2 + \left(d_{shield}\right)^2} \approx \pm 30\% \tag{A.2}$$

Validation

The predictions of this program weri validated by means of a comparison between CISAS Faraday probe and analogous probe employed at Aerospazio Tecnologie S.r.l., an Italian society, based at Rapolano Serre (SI), specialized in electric thrusters testing. Aerospazio's probe (Figure[A.4]) is characterized by a bigger ϕ=10 mm collector, surrounded by a trunked metal cone acting as the guard ring, having the same polarization of the collector plate while being electrically decoupled from it. The two probes were both employed during a test campaign on an HPT model, where they were mounted on the same support and placed symmetrically with respect to the axis of the thruster, in order to be invested by the same plasma flow. The distance from the thruster exhaust was 0.5 m; the estimated plasma density at such distance was $n_e \approx 2.5^{12}$ m^{-3}, with an electron temperature $T_e \approx 5eV$ and a neglectible magnetic field. In these conditions the Debye shielding length [8] can be estimated as:

$$\lambda_D = \sqrt{\frac{\epsilon_0 \cdot k_B \cdot T_e}{n_e \cdot q_e^2}} \approx 3.35mm \tag{A.3}$$

where k_B is Boltzmann's constant, ϵ_0 is the vacuum dielectric permittivity, and q_e is the electron charge. A Debye length of 3.35 mm can be considered a sufficiently large distance with respect to the diameter of the two probes for the uncertainty due to shielding to be negligible.

Both probes were both polarized at -150 V, while the mean energy of the incoming ions was estimated around 80-100 eV. The currents read by the probes were plotted against each other, reconstructing a line trend which can be seen in Figure[A.5]. The same plot was then reconstructed theoretically, first estimating the focusing of the two probes in the operating conditions and then calculating Aerospazio's probe current as a function of CISAS' one: $I_{Aerospazio} = I_{CISAS}/(A_{p,CISAS} \cdot fe_{CISAS}) \cdot A_{p,Aerospazio} \cdot fe_{Aerospazio} + I_{offset}$, where $A_{p,Aerospazio}$ and $A_{p,CISAS}$ are the effective collection areas of the two probes and $fe_{Aerospazio}$ and fe_{CISAS} are the relative focusing factors, while I_{offset} is an offset bias. From the simulation $fe_{Aerospazio}$=1.25 and fe_{CISAS}=1.71, which, setting I_{offset}=0.1 μA (a realistic value, considering the experimental uncertainties on current measurements), led to a very good agreement with the experimental data.

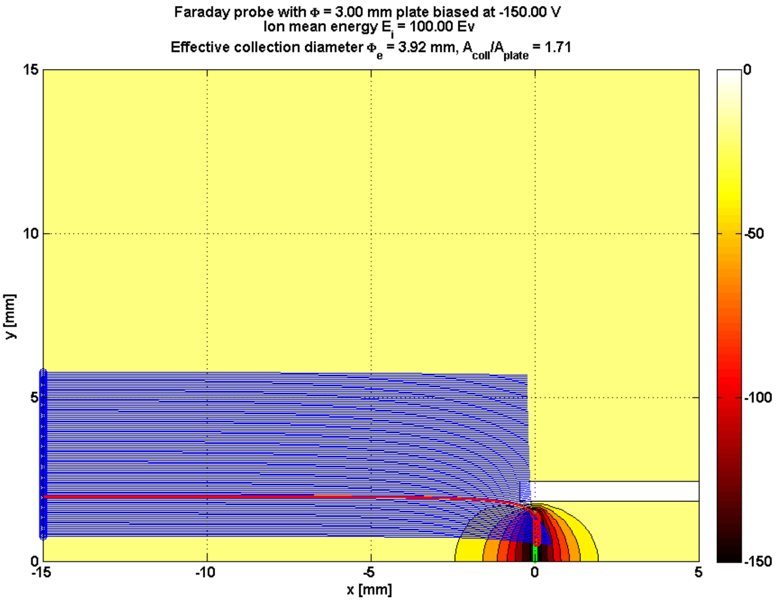

Figure A.3: Example of program output for an Argon plasma (mass = 40 proton masses) with $E_i \approx 100$ eV and a probe bias of -150 V.

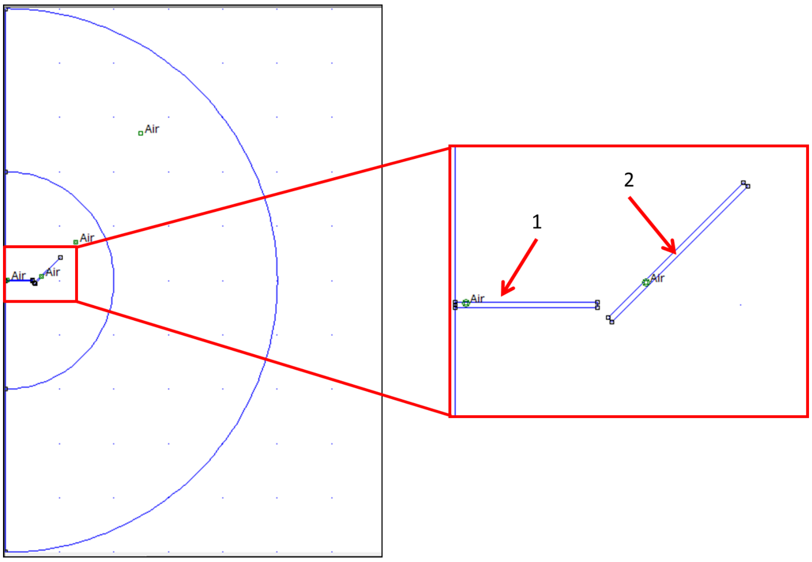

Figure A.4: FEMM model of Aerospazio's Faraday probe. The diameter of the collector (1) is 10 mm, while the diameter of the conical guard ring (2) is 20 mm. The two are electrically insulated but have the same polarization.

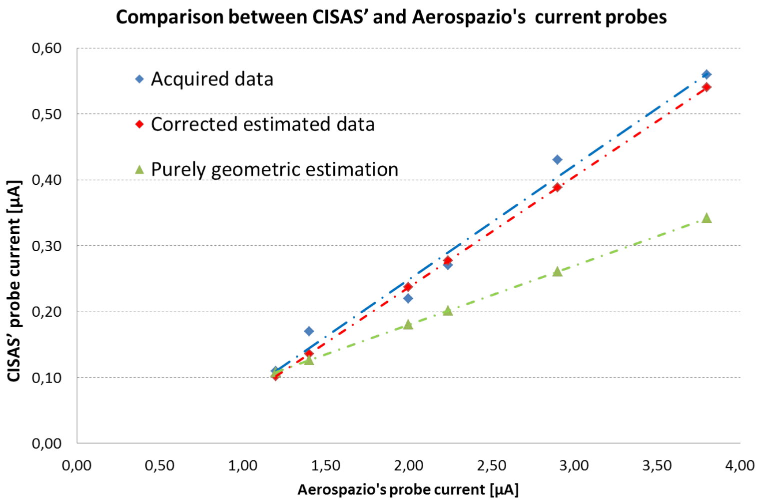

FIGURE A.5: Comparison of experimental and theoretical current readings. The effectiveness of the focusing correction is evidenced by the uncorrected theoretic prediction, elaborated without taking into account the focusing factors. The agreement between corrected current estimations and experimental measurements is easily appreciated.

Bibliography

[1] Cluster tecnologico nazionale. http://http://www.ctna.it/.

[2] Daniele Pavarin, Fernando Ferri, M Manente, D Curreli, Y Guclu, D Melazzi, D Rondini, S Suman, J Carlsson, Cristina Bramanti, et al. Design of 50 w helicon plasma thruster. In *31st Int. Electric Propulsion Conf., Ann Arbor, MI*, pages 2009–205, 2009.

[3] D Pavarin, F Ferri, M Manente, A Lucca Fabris, F Trezzolani, M Faenza, L Tasinato, O Tudisco, R Deangelis, A Loyan, et al. Thruster development set-up for the helicon plasma hydrazine combined micro research project. In *Proceedings of the 32nd International Electric Propulsion Conference (IEPC'11)*, 2011.

[4] D.M. Goebel and I. Katz. *Fundamentals of Electric Propulsion: Ion and Hall Thrusters*. JPL Space Science and Technology Series. Wiley, 2008. ISBN 9780470436264. URL `http://books.google.it/books?id=P50GFXcBKcwC`.

[5] Salvo Marcuccio, Angelo Genovese, and Mariano Andrenucci. Experimental performance of field emission microthrusters. *Journal of Propulsion and Power*, 14(5): 774–781, 1998.

[6] Franklin R Chang Diaz. The vasimr rocket. *Scientific American*, 283(5):90–97, 2000.

[7] Cristina Bramanti and D Fearn. The design and operation of beam diagnostics for the dual stage 4-grid ion thruster. In *30th International Electric Propulsion Conference, Florence, Italy September*, pages 17–20, 2007.

[8] F.F. Chen. *Introduction to Plasma Physics and Controlled Fusion*. Number v. 1 in Introduction to Plasma Physics and Controlled Fusion. Springer, 1984. ISBN 9780306413322. URL `http://books.google.it/books?id=ToAtqnznr80C`.

[9] Timothy Ziemba, John Carscadden, John Slough, James Prager, and Robert Winglee. High power helicon thruster. In *41th Joint Propulsion Conference, Tucson, AR*, 2005.

[10] Oleg Batishchev, Justin Pucci, Nareg Sinenian, Zachary LaBry, Murat Celik, and Manuel Martinez-Sanchez. Mini-helicon thruster experiment at mit. In *APS Meeting Abstracts*, volume 1, 2006.

[11] Michael D West, Christine Charles, and Rod W Boswell. Testing a helicon double layer thruster immersed in a space-simulation chamber. *Journal of Propulsion and Power*, 24(1), 2008.

[12] K Takahashi, T Lafleur, C Charles, P Alexander, RW Boswell, M Perren, R Laine, S Pottinger, V Lappas, T Harle, et al. Direct thrust measurement of a permanent magnet helicon double layer thruster. *Applied Physics Letters*, 98(14):141503, 2011.

[13] F Trezzolani, A Lucca Fabris, D Pavarin, A Selmo, A I Tsaglov, A V Loyan, O P Rubalov, and M Manente. Low power radio-frequency plasma thruster development and testing. 2013.

[14] Daniele Pavarin, Andrea Lucca Fabris, Fabio Trezzolani, Marco Manente, Martina Faenza, Francesca Ferri, Antonio Selmo, Konstantinos Katsonis, and Chloe Berenguer. Low power rf plasma thruster experimental characterization. In *48th AIAA/ASME/SAE/ASEE Joint Propulsion Conference & Exhibit*, 2012.

[15] W.L. Stutzman and G.A. Thiele. *Antenna Theory and Design*. Antenna Theory and Design. Wiley, 2012. ISBN 9780470576649. URL `http://books.google.co.uk/books?id=xhZRA1K57wIC`.

[16] O.A. Popov. *High Density Plasma Sources: Design, Physics and Performance*. Elsevier Science, 1996. ISBN 9780815517894. URL `http://books.google.it/books?id=8lVF_839zYkC`.

[17] O Tudisco, A Lucca Fabris, C Falcetta, L Accatino, R De Angelis, M Manente, F Ferri, M Florean, C Neri, C Mazzotta, et al. A microwave interferometer for small and tenuous plasma density measurements. *Review of Scientific Instruments*, 84(3):033505, 2013.

[18] Andrea Lucca Fabris. *Experimental Characterization of Plasma Sources for Space Propulsion*. PhD thesis, Università degli Studi di Padova, april 2014.

[19] K Katsonis, Ch Berenguer, D Pavarin, A Lucca Fabris, F Trezzolani, M Faenza, P Tsekeris, S Cohen, and M Cornille. Optical diagnostics of a low temperature argon thruster. In *Proceedings of the 32nd International Electric Propulsion Conference (IEPC'11)*, 2011.

[20] Robert L Petry. Critical potentials in secondary electron emission from iron, nickel, and molybdenum. *Physical Review*, 26(3):346, 1925.

[21] B.S. Guru and H.R. Hiziroglu. *Electromagnetic Field Theory Fundamentals*. Cambridge University Press, 2004. ISBN 9781139451925. URL `http://books.google.it/books?id=qzNdDtZUPXMC`.

[22] David Meeker. Finite element method magnetics version 4.2 user's manual. `http://http://www.femm.info/Archives/doc/manual42.pdf`. Last Updated: October 2010.

[23] Robyn L Carrasquillo, James L Reuter, and Cynthia L Philistine. Summary of resources for the international space station environmental control and life support system. Technical report, SAE Technical Paper, 1997.

[24] F Bosi, A Lucca Fabris, F Trezzolani, M Manente, D Melazzi, and D Pavarin. Modelling and optimization of electrode-less helicon plasma thruster with different propellants. In *50th AIAA/ASME/SAE/ASEE Joint Propulsion Conference*, pages 28–30, 2014.

[25] Seiji Tsurubuchi and Tsuruji Iwai. Simultaneous ionization and excitation of co_2 by electron-impact. *Journal of the Physical Society of Japan*, 37(4):1077–1081, 1974.

[26] Smco magnets datasheet. http://www.algamagneti.it/prodotti/magneti-in-samario-cobalto.htm.

[27] M. Fauri, F. Gnesotto, and G. Marchesi. *Lezioni di elettrotecnica*. Number v. 3 in Lezioni di elettrotecnica. Progetto Leonardo, 2003. ISBN 9788874880362. URL `http://books.google.it/books?id=m44uAAAACAAJ`.

[28] Rg-213 cable datasheet. http://www.odeskabel.com/radio-eng/images/stories/pdfs/5.pdf.

[29] N-type connector datasheet. http://rfconnector.com/n-connectors.php.

[30] Mks 1179a mass-flo mass flow controllers. http://www.mksinst.com/product/.

[31] B. Ferrario and A. Calcatelli. *Introduzione alla tecnologia del vuoto*. Pàtron, 1999. ISBN 9788855525107. URL `https://books.google.it/books?id=iErIPAAACAAJ`.

[32] Kazunori Takahashi, Christine Charles, Rod Boswell, and Akira Ando. Effect of magnetic and physical nozzles on plasma thruster performance. *Plasma Sources Science and Technology*, 23(4):044004, 2014.

[33] R Giometti and F. Frascari. *Elettrotecnica - Elettronica - Radiotecnica*, volume 1. Calderini, 1976.

[34] R Giometti and F. Frascari. *Elettrotecnica - Elettronica - Radiotecnica*, volume 2. Calderini, 1976.

[35] R Giometti and F. Frascari. *Elettrotecnica - Elettronica - Radiotecnica*, volume 1. Calderini, 1976.

[36] M. Albulet. *RF Power Amplifiers*. Institution of Engineering and Technology, 2001. ISBN 9781884932120. URL `http://books.google.it/books?id=HrDXZctHzUQC`.